Nanoscale

Accepted Manuscript

This article can be cited before page numbers have been issued, to do this please use: M. Dong, Y. Sun, D. J. Dunstan, R. J. Young and D. G. Papageorgiou, *Nanoscale*, 2024, DOI: 10.1039/D4NR01356E.

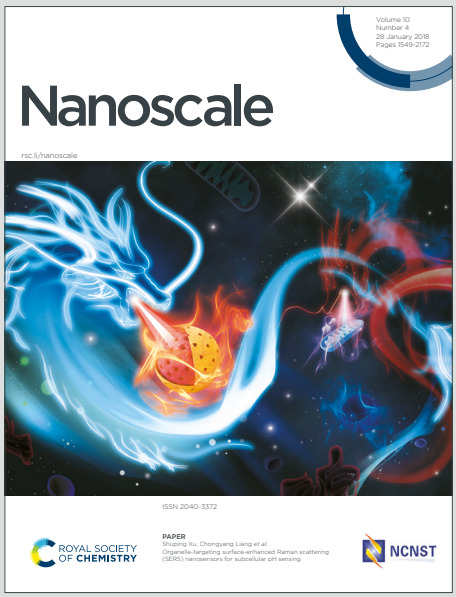

ROYAL SOCIETY OF CHEMISTRY

rsc.li/nanoscale

No primary research results, software or code have been included and no new data were generated or analysed as part of this review.

View Article Online
DOI: 10.1039/D4NR01356E

View Article Online
DOI: 10.1039/D4NR01356E

Mechanical reinforcement from two-dimensional nanofillers: model, bulk and hybrid polymer nanocomposites

Ming Dong[1], Yiwei Sun[1], David J. Dunstan[2], Robert J. Young[3*], Dimitrios G. Papageorgiou[1*]

[1] School of Engineering and Materials Science, Queen Mary University of London, London E1 4NS, United Kingdom

[2] School of Physics and Chemical Sciences, Queen Mary University of London, London E1 4NS, United Kingdom

[3] National Graphene Institute, Department of Materials, School of Natural Sciences, The University of Manchester, Manchester M13 9PL, United Kingdom

Corresponding authors' emails: d.papageorgiou@qmul.ac.uk (Dimitrios Papageorgiou),

robert.young@manchester.ac.uk (Robert J. Young)

Abstract

Thanks to their intrinsic properties, multifunctionality and unique geometrical features, two-dimensional nanomaterials have been used widely as reinforcements in polymer nanocomposites. The effective mechanical reinforcement of polymers is, however, a multifaceted problem as it depends not only on the intrinsic properties of the fillers and the matrix, but also upon a number of other important parameters. These parameters include the processing method, the interfacial properties, the aspect ratio, defects, orientation, agglomeration and volume fraction of the fillers. In this review, we summarize recent advances in the mechanical reinforcement of polymer nanocomposites from two-dimensional nanofillers

View Article Online
DOI: 10.1039/D4NR01356E

with an emphasis on the mechanisms of reinforcement. Model, bulk and hybrid polymer nanocomposites are reviewed comprehensively. The use of Raman and photoluminescence spectroscopies is examined in light of the distinctive information they can yield upon stress transfer at interfaces. It is shown that the very diverse family of 2D nanofillers includes a number of materials that can attribute distrinctive features to a polymeric matrix, and we focus on the mechanical properties of both graphene and some of the most important 2D materials beyond graphene, including boron nitride, molybdenum disulphide, other transition metal dichalcogenides, MXenes and black phosphorous. In the first part of the review we evaluate the mechanical properties of 2D nanoplatelets in "model" nanocomposites. Next we examine how the performance of these materials can be optimised in bulk nanocomposites. Finally, combinations of these 2D nanofillers with other 2D nanomaterials or with nanofillers of other dimensions are assessed thoroughly, as such combinations can lead to additive or even synergistic mechanical effects. Existing unsolved problems and future perspectives are discussed.

Keywords: *mechanical properties, two-dimensional materials, nanocomposites, graphene, boron nitride, molybdenum disulphide*

View Article Online
DOI: 10.1039/D4NR01356E

Contents

Mechanical reinforcement from two-dimensional nanofillers: model, bulk and hybrid polymer nanocomposites....1
1. Introduction....4
2. Two-dimensional materials: preparation and mechanical properties....7
2.1. Preparation....7
2.1.1 Top-down methods....7
2.1.2 Bottom-up methods....10
2.2. Mechanical Properties....10
2.2.1. Stiffness and strength....11
2.2.2. Toughness....18
3. "Model" nanocomposites....20
3.1. Theories of reinforcement in polymer matrix: the shear-lag theory....21
3.2. Model monolayer nanocomposites....23
3.3. Model few- and many-layer nanocomposites....32
3.4. Stacking, scrolling and folding in model nanocomposites....37
4. Bulk nanocomposites....39
4.1. Preparation....39
4.1.1 Solution casting....40
4.1.2 Melt mixing....41
4.1.3 In situ polymerization....43
4.1.4 Layer-by-layer assembly....44
4.1.5 Other methods....45
4.2. Mechanisms of Reinforcement....46
4.2.1 Analytical model....46
4.2.2 Semi-empirical model....51
4.3. Mechanical Properties....52
4.3.1 Graphene nanocomposites....52
4.3.2 Boron nitride nanocomposites....59
4.3.3 TMDC-based nanocomposites....64
4.3.4 MXene-based nanocomposites....68
4.3.5 Black phosphorus nanocomposites....71
4.3.6 Other nanocomposites....74
5. Hybrid nanocomposites....75
5.1. 2D-2D nanocomposites....75
5.2. 2D-1D nanocomposites....80
5.3. 2D-0D nanocomposites....85
6. Conclusions and Outlook....89
References....91

View Article Online
DOI: 10.1039/D4NR01356E

1. Introduction

Since its isolation in 2004 in Manchester [1], graphene, the first two-dimensional (2D) material, has been studied extensively and utilised in different fields, including electronics, photonics and composites, as a result of its impressive intrinsic properties [2]. The very interesting research on graphene-related materials has motivated researchers to explore further the large family of 2D materials, such as hexagonal boron nitride (h-BN) [3], transition metal dichalcogenides (TMDCs) of the type MX_2 [4], transition metal carbides, nitrides, or carbonitrides (MXenes, where M = transition metal and X = C or N [5]) and black phosphorus (BP) [6], as shown in Figure 1. The majority of these 2D materials display impressive and sometimes unusual mechanical, electrical and optical properties in comparison to their three-dimensional (3D) counterparts as a result of their atomic thinness, high specific surface area and electron confinement in 2D sheets [7]. For example, graphene with hexagonal sp^2 hybridized carbon atoms in its structure, alongside its zero band gap, shows excellent electron mobility of 250,000 cm^2/V s along with a very high thermal conductivity of around 5000 W/mK [8, 9]. On the other hand, monolayer MoS_2 and BP are semiconductors while h-BN is an electrical insulator.

Amongst the long list of exceptional properties and numerous applications of 2D materials, their mechanical properties and the corresponding reinforcement in the field of polymer nanocomposites are very appealing to both academia and industry, as in many cases they can be readily incorporated into polymers using established manufacturing processes [10-12]. The majority of 2D materials possess high in-plane stiffness and strength resulting from their strong covalent bonds [13, 14]. For example, graphene has in-plane stiffness of the order of 1 TPa resulting from its sp^2 hybrid bonds [15, 16]. Similarly, h-BN displays good mechanical properties with a stiffness up to 90% of graphene [17], while the stiffness of MoS_2 is about 300 GPa [18]. The direct transfer of these properties into nanocomposites, however, presents challenges. The first is the importance of the lateral size and aspect ratio of 2D nanofillers. To achieve high levels of mechanical reinforcement in polymer nanocomposites by 2D materials, flakes with large lateral sizes (>30 μm) are favoured, given that in order to obtain good reinforcement,

View Article Online
DOI: 10.1039/D4NR01256E

the flake length should be ~10× the critical length, according to the shear lag theory developed initially for fibres [19, 20]. Large flakes, however, have a high probability of containing a large number of defects and these defects will unavoidably degrade the mechanical properties of the 2D nanosheets. It is also very challenging to prepare nanosheets of consistently large lateral dimensions via bulk-scale production methods. A number of top-down exfoliation and bottom-up synthesis methods have been proposed to produce high quality 2D materials while also achieving a high production yield [21]. Additional challenges include obtaining a homogeneous distribution of the flakes, the unavoidable damage of the flakes during melt processing and the increase of melt viscosity at higher filler content. Nevertheless, the incorporation of 2D nanosheets can not only lead to considerable improvements in the mechanical properties, but also attribute good thermal, electrical and optical properties. It is highly desirable, therefore, to make a comparison between different fabrication strategies, different nanofiller combinations and their reinforcement mechanisms in polymer nanocomposites in order to understand how to the maximise the level of reinforcement and hence target a wide number of applications.

Due to the increasing interest in graphene and graphene-based nanocomposites, a large number of reviews have been published on the mechanical properties of graphene-based nanocomposites [16, 22, 23]. There are other reviews upon the mechanical properties of 2D materials [13, 14, 24], and perspective articles about the emerging trends and challenges of polymer nanocomposites with 2D materials [10, 11]. Here, we go beyond the scope of these earlier reviews and examine the mechanisms of mechanical reinforcement of polymers by 2D nanomaterials with a particular focus upon the range of 2D materials beyond graphene. We focus on the study of model composites in order to understand the mechanical characteristics of 2D monolayers and evaluate their combination with nanomaterials of different dimensions in hybrid nanocomposites, as illustrated in Figure 1. In Section 1, a brief introduction is given of 2D nanomaterials and polymer nanocomposites. In Section 2, the various preparation methods (including top-down and bottom-up) of a number of 2D materials are discussed along with their intrinsic mechanical properties. In Section 3, a series of model nanocomposites based on 2D materials

View Article Online
DOI: 10.1039/D4NR01556E

are reviewed. The use of Raman spectroscopy and photoluminescence (PL) spectroscopy is examined in detail as both techniques can offer invaluable information in the characterization of the mechanical properties and of the nanoscale reinforcement. The mechanical properties of bulk nanocomposites based on different 2D nanosheets are reviewed in detail in Section 4, with an emphasis on graphene, h-BN, TMDCs and MXenes nanocomposites. Hybrid nanocomposites based on 2D nanosheets (including 2D-2D, 2D-1D and 2D-0D composites) are thoroughly discussed in Section 5. Finally, future perspectives for the field of mechanical reinforcement of polymer nanocomposites reinforced with 2D materials are discussed in Section 6.

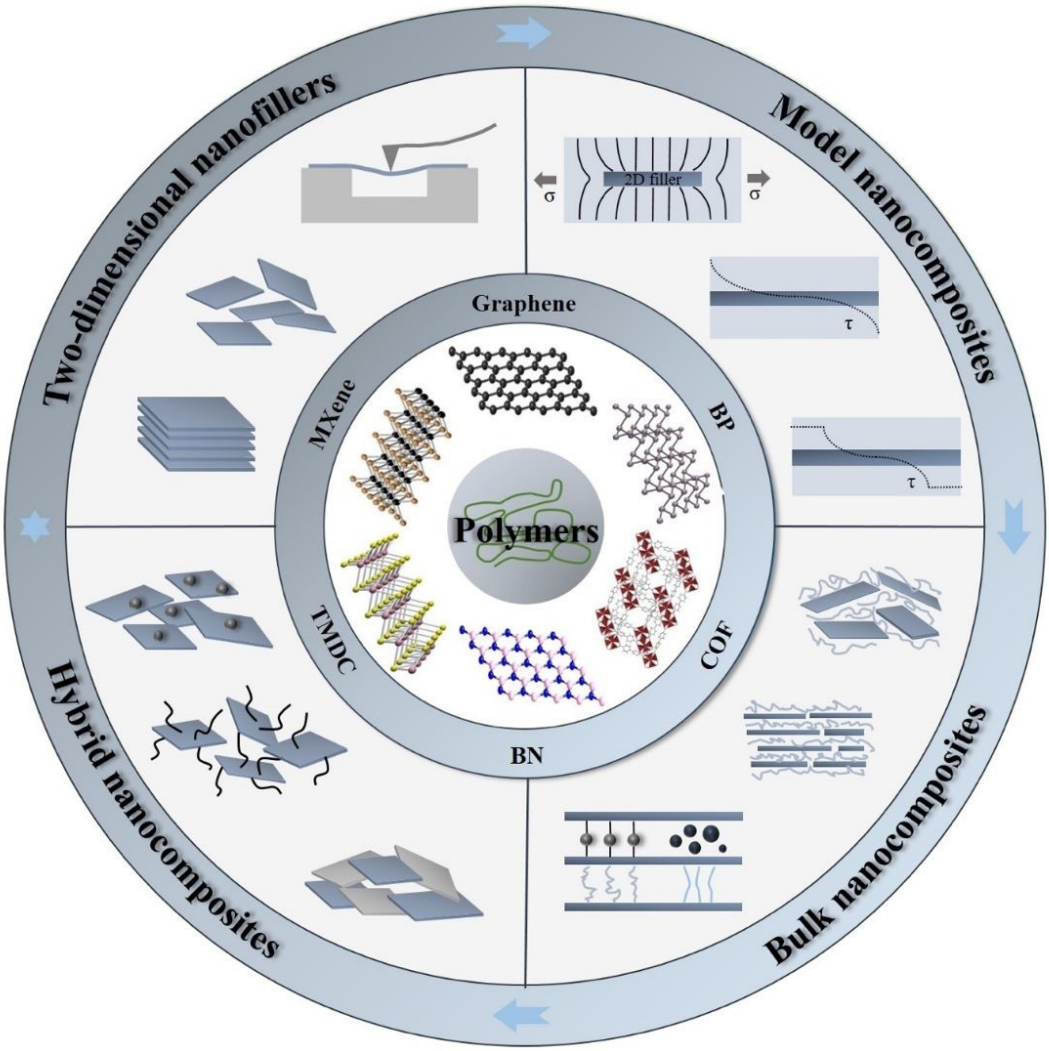

Figure 1. Illustration of mechanical reinforcement in a polymer matrix from two-dimensional nanofillers, including graphene, BN, TMD, MXene, BP and COF (covalent organic frameworks).

View Article Online
DOI: 10.1039/D4NR01356E

2. Two-dimensional materials: preparation and mechanical properties

2.1. Preparation

During the past decades, various methods have been used to prepare 2D materials in order to explore their fundamental mechanical, electrical and optical properties, and to promote their use in numerous applications. These approaches can be divided into two categories: top-down and bottom-up. Here we summarize recent advances in the preparation of 2D materials with a highlight on their applications in polymer nanocomposites.

2.1.1 Top-down methods

Top-down methods include the preparation of 2D materials through the exfoliation of their bulk crystals. During the exfoliation process, the interlayer attraction is overcome by external mechanical or electrochemical forces. The two major methods are mechanical exfoliation and liquid exfoliation. Mechanical cleavage is the simplest way to produce multilayer and monolayer 2D materials [1, 25]. In 2004, using highly-ordered pyrolytic graphite (HOPG), the Manchester group were the first to mechanically exfoliate graphite to monolayer graphene [1]. High-quality monolayer nanosheets can be obtained by repeating this exfoliation process several times. This method has been used widely to exfoliate a number of 2D materials beyond graphene, given its simplicity, applicability and the resulting large-area and high-quality samples [26]. It does, however, come with certain disadvantages. For example, it is very difficult to control the size and shape of the flakes. Most importantly, it is impossible to achieve high-yields to meet practical requirements for the development of applications such that material produced by this process is only suitable for research studies.

View Article Online
DOI: 10.1039/D4NR01356E

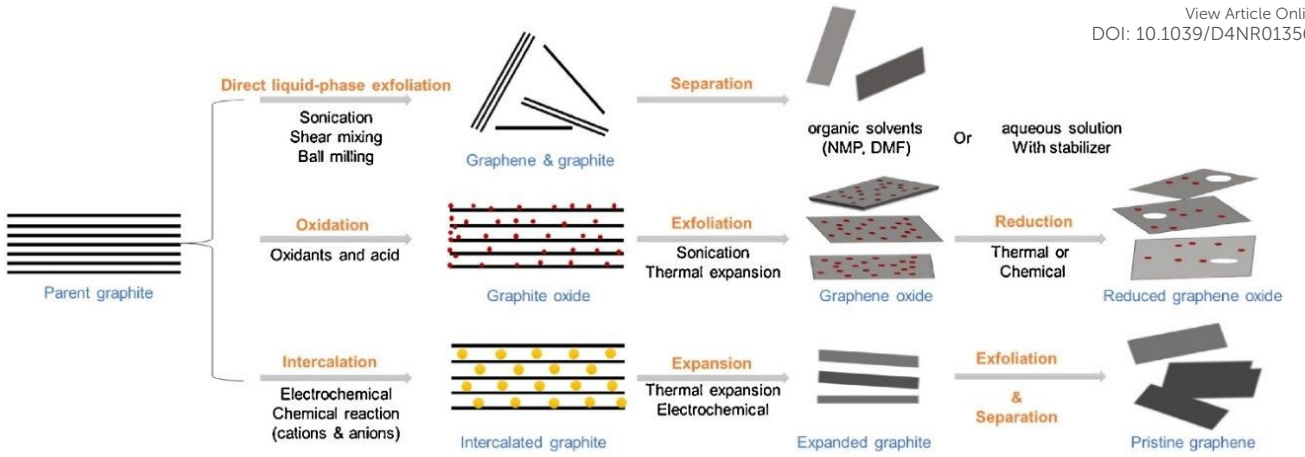

Figure 2. Liquid exfoliation methods for the preparation of graphene and related 2D nanosheets, including mechanical force-assisted, oxidation-assisted and intercalation-assisted exfoliation. Reproduced with permission from [11]. Copyright 2018 Elsevier.

Liquid-phase exfoliation is one of the most promising methods for the high-yield production of 2D materials [21, 27, 28]. 2D materials with layered bulk crystals can be exfoliated in an appropriate liquid phase. Mass production can be achieved by the liquid exfoliation method in an inexpensive and relatively simple way. Exfoliated 2D materials can be processed directly by solution blending for applications in polymer nanocomposites. The method follows three successive steps: dispersion, exfoliation and purification. Liquid exfoliation processes can be classified into three distinct types: mechanical-, intercalation-, and oxidation-assisted methods. Mechanically-assisted methods include sonication, shear mixing, and ball milling. Sonication was first employed in the exfoliation of graphite flakes [29] and leads to the rupture of large flakes and the formation of kink band striations on the surfaces of the flakes. Cracks form along these striations and together with intercalation of solvent, lead to the unzipping and peeling off of thin graphite strips that are exfoliated into graphene [28]. The key point for efficient exfoliation is matching the surface energy between the layered materials and the solvents. Low boiling-point or volatile solvents are preferred to facilitate post-processing. Solvents also play an important role in the stabilization of exfoliated 2D sheets to prevent their agglomeration. This method has been applied widely to various layered materials beyond graphene such as h-BN and TMDCs [30].

View Article Online
DOI: 10.1039/D4NR01356E

Liquid-phase exfoliation also presents some drawbacks such as the low yield of monolayer flakes and their small lateral sizes (nanometres or no more than a few microns).

Shear-force-assisted liquid exfoliation was developed to improve the productivity of the method [31]. Typically, shear is generated by a rotor-stator mixer or even a kitchen blender [32]. This method is highly promising for the production of 2D materials on an industrial scale. Alternatively, mechanical forces can be generated by ball milling [33]. This method suffers seriously, however, from the production of flakes with very small lateral size (in the order of nanometres) and a key restriction on the applicability of these methods is the achievable flake size.

For the production of large flakes, ion intercalation-assisted liquid exfoliation has been proposed [34]. This method relies on the intercalation of cations into the interlayer space of layered structures to enlarge the interlayer distance and weaken the interlayer forces. Reactions between the cations and the solvents can produce hydrogen gas to further facilitate the exfoliation. This method has been successfully applied to exfoliate graphene and TMDCs with large lateral sizes of tens of micrometres [34, 35]. One disadvantage of this method is the poor control of the ion intercalation process. This results in the insufficient or excessive intercalation of ions, and more post-processing is then required. Furthermore, it is more time-consuming compared to mechanical force-assisted liquid exfoliation as ion intercalation takes place over longer periods [7].

In oxidation-assisted liquid exfoliation for graphene oxide (GO) [36] and selective etching-assisted liquid exfoliation for MXenes [7], the oxidation or etching stages are a pre-treatment of the bulk crystals. Oxidation generates functional groups on the surfaces of graphene. These functional groups can enlarge the interlayer spacing of the graphite and weaken the van der Waals (vdW) interactions. Exfoliation is then obtained by sonication so that monolayer or multilayer GO can be produced. This method is effective for the preparation of GO, but it is not applicable to other materials. Selective etching-assisted liquid exfoliation has been used for the exfoliation of MXenes. In contrast to most layered structures connected by weak vdW bonds, the $M_{n+1}X_n$ (n = 1, 2, or 3) layers in MAX phases

View Article Online
DOI: 10.1039/D4NR01356E

are connected by the A layers (elements of group ⅢA or ⅣA). The covalent bonds mean that stronger forces are required to exfoliate MXenes from their bulk crystals. Gogotsi *et al.* [37] were the first to exfoliate MXenes from their MAX phases successfully. They fabricated 2D nanosheets composed of Ti_3C_2 layers by exfoliating $TiAlC_2$ in a hydrofluoric acid (HF) solution without causing damage to the remaining structure. The lateral size of nanosheets from this method is a few hundred nanometres, small enough to limit the reinforcement efficiency of individual nanosheets in polymer nanocomposites, especially at low filler contents.

2.1.2 Bottom-up methods

Bottom-up methods such as chemical vapour deposition (CVD) can be employed to grow large area, high quality 2D materials from the deposition of gaseous reactants onto a suitable substrate [38, 39]. A substrate such as Cu or Ni [38] is put into a chamber and the gas molecules come into contact with the substrate. Reactions between gaseous reagents then take place, to create the target material as a thin film on the substrate. Factors such as the temperature, pressure, substrate, growth time and the catalyst have to be optimized to synthesize high-quality thin films [40]. Li *et al.* [41] produced centimetre-scale monolayer and bilayer graphene on copper foil using methane. The CVD method has been applied to produce numerous other 2D materials [42]. To upscale the CVD method, roll-to-roll (R2R) processes have been used for graphene [43]. 2D materials are grown on moving copper foils and then are transferred from the growth substrate to polymer substrates. Overall, the CVD process is advantageous in terms of the capability of preparing large-size high-quality 2D materials. It displays some problems, however, compared to the top-down methods. It is more expensive due to the specific experimental conditions such as high temperature and inert atmospheres. Additionally, 2D materials produced by CVD need to be transferred to different substrates for further applications.

2.2. Mechanical Properties

View Article Online
DOI: 10.1039/D4NR01356E

The mechanical properties of 2D materials constitute one of the main reasons for their immense interest from academia and industry. The mechanical properties of 2D materials have already been reviewed in terms of elastic properties, interfacial behaviour, failure mechanisms, characterization methods and coupling properties (including electromechanical, optomechanical, and thermomechanical properties) [13, 14, 24]. In this section, we will summarize the intrinsic stiffness, strength and toughness of a range of 2D materials.

2.2.1. Stiffness and strength

Experimentally, atomic force microscopy (AFM) nanoindentation has been used extensively to characterize the elastic properties of 2D materials due to its ability to probe the mechanical properties of individual nanosheets [15]. As shown in Figures 3a to 3d, monolayer or multilayer 2D membranes are suspended over circular holes on substrates and are indented by AFM tips at their centre [15]. Load-indentation depth curves are then obtained and the Young's modulus of 2D membranes E^{2D} can be extracted by fitting the experimental data with an analytical model such as,

$$F = \sigma_0^{2D}(\pi a)\left(\frac{\delta}{a}\right) + E^{2D}(q^3 a)\left(\frac{\delta}{a}\right)^3 \quad (1)$$

where F is the applied load, σ_0^{2D} is the pre-stress already in the membrane before any displacement, δ is the displacement at the centre of the membrane, q is a dimensionless parameter depending on the Poisson's ratio, and a is the radius of the membrane. Under the elastic deformation assumption, the strength of 2D membranes, σ^{2D} at failure can be estimated using [15]

$$\sigma^{2D} = \left(\frac{FE^{2D}}{4\pi R}\right)^{\frac{1}{2}} \quad (2)$$

where R is the radius of the tip. The 3D Young's modulus E and breaking strength σ can be obtained after taking into consideration the thickness of the membranes. It should be noted that many authors have used simplified equations based on the Schwerin-type point-load solutions [44], such as Eq. (1). However, more thorough analyses, such as the one from Jin *et al.* [45], suggest that these equations are

View Article Online
DOI: 10.1039/D4NR01356E

over-simplified and using them to extract the mechanical properties from indentation testing of free-standing membranes can result in significant errors. Additionally, the easy slippage between layers in multilayer samples brings further complications. An important detail that needs to be considered is that the AFM nanoindentation technique focuses on very small areas of the nanosheets, so that there is a low probability of encountering defects [46].

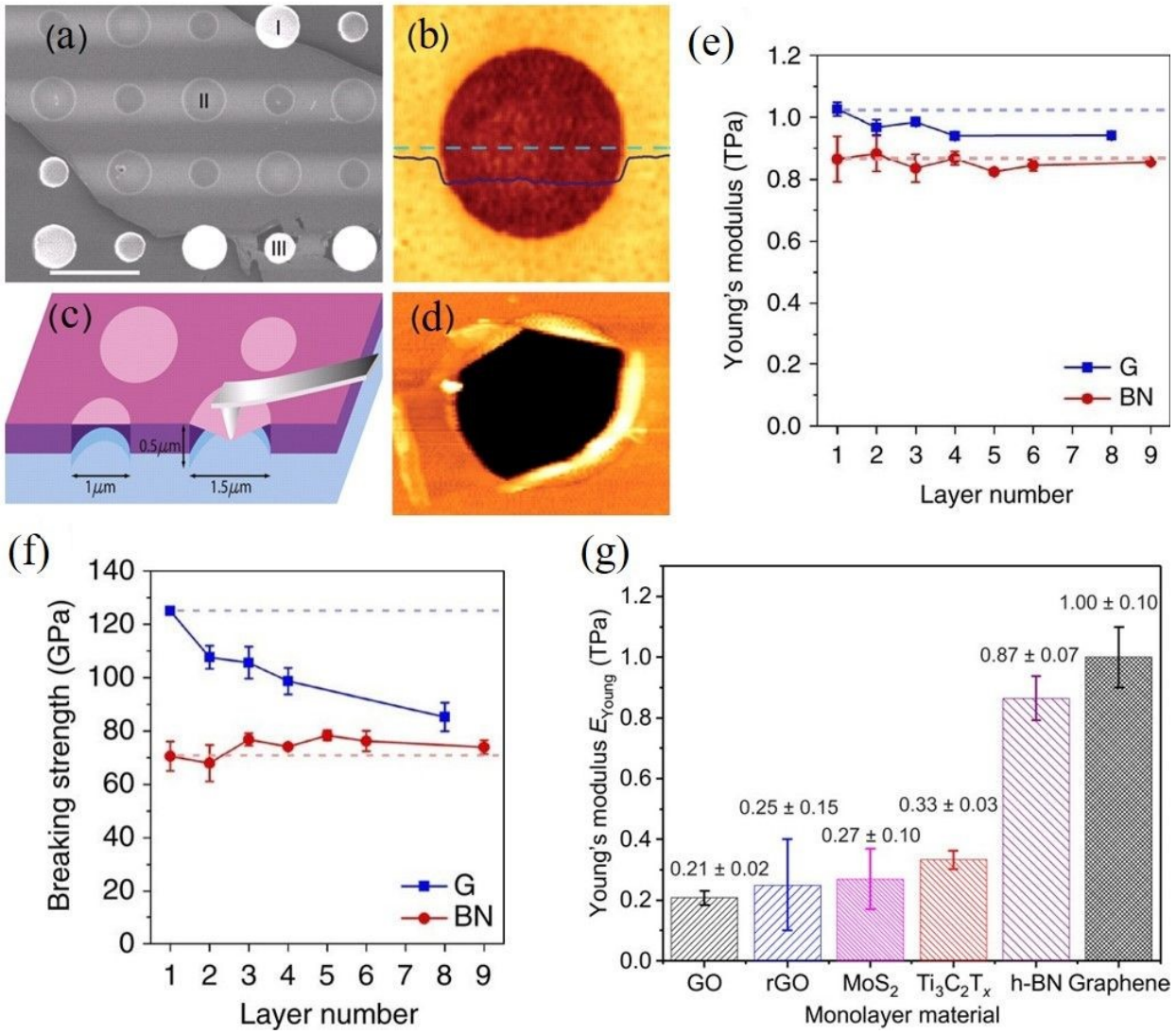

Figure 3. (a-d) AFM indentation method for the measurement of stiffness and strength of graphene. Reproduced with permission from [15]. Copyright 2008 AAAS. (e, f) Variations of Young's modulus and breaking strength with layer number of graphene (G) and BN. Reproduced with permission from [17]. Copyright 2017 Nature Publishing Group. (g) Young's modulus of various 2D materials. Reproduced with permission from [47]. Copyright 2018 AAAS.

View Article Online
DOI: 10.1039/D4NR01356E

More recently, *in situ* tensile tests have been applied to measure the elastic properties of 2D materials [48-50]. To conduct an *in situ* tensile test, monolayer 2D materials are prepared and transferred onto a push-to-pull micromechanical device. The displacement-controlled tensile test is carried out in a scanning electron microscope (SEM) and the mechanical properties can be assessed from the load-displacement curves. Quite importantly, this method can apply a uniform loading to the 2D material plane and the corresponding elastic properties can be directly determined. The Young's modulus, tensile strength and elastic strain of monolayer graphene [48] and $Ti_3C_2T_x$ [49] have been determined using this method.

The buckling method is another highly useful and interesting method that can be used to measure the stiffness of 2D films or nanosheets [51]. This technique is based upon the buckling instabilities that form when a stiff material is deposited (or coated) as a thin film under compressive strain onto a soft, thick substrate. Using the well-established mechanics of buckling [52, 53] and by observing the periodicity and spacing of the wrinkles that are formed, the elastic modulus of a nanosheet (or film) (E_{film}) can then be calculated based on the relationship between the ripple period (λ) and the flake thickness (h):

$$E_{\text{film}} = \frac{3(1-\nu_{\text{f}}^2)E_{\text{s}}}{8\pi^3(1-\nu_{\text{s}}^2)}\left(\frac{\lambda}{h}\right)^3 \quad (3)$$

where E_{s} is the modulus of the substrate (assuming there is no slippage between the substrate and the nanosheet) and ν_{f} and ν_{s} are the Poisson's ratio of the flake and the substrate, respectively. Recently, the buckling method has been applied to TMDCs for the measurement of Young's modulus of thin films and the elastic moduli determined show good agreement with the values extracted from AFM indentation [54]. It should be noted that the buckling test is not able to determine the strength of 2D materials, given that delamination invariably takes place before fracture. Additionally, the buckling method can sometimes be unreliable, as plate mechanics might not apply to certain 2D materials with relatively weak vdW interlayer interactions [55, 56].

The Young's modulus (~ 1 TPa) and breaking strength (~ 130 GPa) of monolayer graphene (assuming a thickness of 0.335 nm) were first reported by Lee *et al.* [15]. High-quality monolayer

View Article Online
DOI: 10.1039/D4NR01356E

graphene synthesised by CVD was also investigated by AFM indentation and found to have modulus and strength values similar to mechanically-exfoliated material [57]. It is generally accepted that the strength of graphene decreases with an increase in number of layers [17, 58]. The hypothesis for the degradation of the strength of graphene is based on the fact that the interactions between layers influence the load distribution and lead to weakening. The onset of interlayer slippage coincides with the formation of kinks in the graphene. Each slippage step corresponds to a certain part of the interface overcoming energy barriers to go from the initial energy minimum state to the adjacent energy minimum state [58]. Once interlayer slippage occurs, the stress distribution between individual layers becomes unequal. The layer under the highest stress fails first, causing premature failure of the multilayer material and lowering the material strength. It should be noted that the stacking between graphene layers plays a major role in controlling the effective strength of the material. As expected, noncommensurate stacked systems show a lower interlayer shear strength which leads to earlier slippage and a greater drop in the effective strength, compared with commensurate stacked systems. From another aspect, if the external load can be applied evenly to each layer, there is no reason that the breaking strength of a multilayer would differ from a monolayer.

Among various graphene-related materials (GRMs), graphene oxide is one of the most popular materials for reinforcement in polymer nanocomposites. GO consists of a hexagonal carbon network having both sp^2- and sp^3- hybridized carbon atoms. The basal plane is decorated with hydroxyl and epoxide groups, while the edges contain carbonyl and carboxyl groups. The Young's modulus of monolayer graphene oxide (GO) was measured experimentally to be 210 ± 25 GPa [59]. The significantly lower stiffness of GO, compared to monolayer graphene, can be attributed to the transformation of the original sp^2-bonded carbon atoms of graphene into sp^3-bonded atoms *via* covalent bonding with oxygen.

Similar to graphene, h-BN displays a honeycomb structure consisting of sp^2-bonded boron and nitrogen atoms that leads to excellent mechanical properties. Falin *et al.* [17] reported a Young's modulus

View Article Online
DOI: 10.1039/D4NR01356E

of 865 ± 73 GPa and a breaking strength of 70.5 ± 5.5 GPa for h-BN, properties that make it an appealing alternative to graphene in polymer nanocomposites. Most importantly, the Young's modulus and tensile strength of h-BN do not deteriorate with an increase of the number of layers due to strong interlayer interactions (Figure 3e and f). This can be attributed to the difference in the electronic characteristics of graphene and h-BN (semi-metallic and insulating, respectively).

The Young's modulus and breaking strength of mechanically-exfoliated monolayer MoS_2 have been measured to be 270 ± 100 GPa and 22 ± 4 GPa, respectively [18] and the Young's modulus of mechanically-exfoliated multilayer MoS_2 was measured to be 330 ± 70 GPa [60]. High-quality, CVD-grown MoS_2 was found to have a similar modulus value (264 ± 18 GPa) [61]. The mechanical properties of other TMDCs including WS_2 [61], $MoSe_2$ [62], WSe_2 [63] and $MoTe_2$ [64] have also been measured experimentally (Table 1). The Young's modulus and tensile strength of the TMDC sulfides tend to be similar but both decrease when the S is replaced by Se or Te (Table 1) [65].

Lipatov *et al.* [47] measured the Young's modulus and intrinsic strength of monolayer $Ti_3C_2T_x$ MXene to be 330 ± 30 GPa and 17.3 ± 1.6 GPa via AFM indentation (Figure 3g). The modulus value is lower than that derived from theoretical calculations (500 to 600 GPa) [66], most likely due to the monolayer containing defects as a result of solution processing. Interlayer sliding is suppressed as a result of the hydrogen bonding between $Ti_3C_2T_x$ layers, leading to any increase in layer number not degrading mechanical properties [47]. The mechanical properties of $Nb_4C_3T_x$ were measured recently with values of Young's modulus of 386 ± 13 GPa and strength of 26 ± 1.6 GPa being reported [67]. It should be noted that these values are amongst the highest for solution-processed 2D materials other than graphene, which makes MXenes promising candidates for applications in structural composites.

The mechanical properties of black phosphorus (BP) have been investigated using both nanoindentation and buckling. The Young's modulus and breaking strength of monolayer BP were found by nanoindentation to be 58.6 ± 11.7 and 27.2 ± 4.1 GPa in the zigzag direction, 4.79 ± 1.43 and 2.31 ± 0.71 GPa in the armchair direction [68]. Similar results were obtained from the AFM indentation

View Article Online
DOI: 10.1039/D4NR01356E

of BP nanoribbons by Chen *et al.* [69]. The Young's modulus of few-layer BP was determined using the buckling method to be 93.3 ± 21.8/35.1 ± 6.3 GPa (zigzag/armchair) [70].

Reduced values of stiffness and strength have been observed resulting from the presence of defects and wrinkles. Structural defects, such as vacancies, grain boundaries and dislocations are ubiquitous in 2D materials and have significant effects on their mechanical properties [71]. Zhao *et al.* [72] reported, through the use of *in situ* Raman mapping, that the intrinsic strength for large, mechanically-exfoliated monolayer graphene flakes can drop to around 10 GPa as a result of the presence of defects. In the AFM indentation tests of h-BN grown by CVD, poorer elastic properties were determined compared to the values for mechanically-exfoliated samples and theoretical calculations. This was attributed to the presence of vacancy defects [73]. Out-of-plane deformations of 2D materials, such as ripples, wrinkles and crumples may be produced naturally during the preparation of 2D materials [74] and they can modify the mechanical properties of the materials [75]. For example, Ruiz-Vargas *et al.* [75] indented wrinkled graphene using AFM and found that the in-plane stiffness was softened significantly by out-of-plane wrinkles.

It should be noted that there are contradictory findings in the literature where the presence of defects and the variation of grain boundary angles has been reported to lead to an increase in the modulus and tensile strength. The work of Lopez-Polin *et al.* [76] showed a higher stiffness for graphene samples that were bombarded with Ar^+ ions when the mean distance of such vacancy defects was up to ~5 nm (a defect density of 0.2%). For higher defect densities, the elastic modulus decreased once again, while according to continuum mechanics the strength of the graphene sheets also decreased with the presence of defects (regardless of the density). The authors explained the increase of stiffness with an increase in defect density on the basis of the thermodynamic theory of crystalline membranes; the defects suppress the flexural modes with longer wavelengths that do not contribute to a decrease of E^{2D}, leading to an effective increase. Grantab *et al.* [77] used molecular dynamics (MD) and density functional theory (DFT) modelling to understand the effect of grain boundaries on the mechanical

properties of graphene. According to the authors, and quite counterintuitively, as the grain boundary angle and hence the defect density increases, the stress and strain at failure of monolayer graphene increases. This comes as a result of the decrease of the initial length of the critical bonds toward the sp^2 carbon-carbon bond length and the level of pre-existing strain within the critical bonds of the seven-membered rings. As expected, fracture mechanics (Griffith's theory) was unable to account for these observations since continuum theories ignore the presence of atomic bonds. There is no clear consensus on the effect of defects on the strength and stiffness of graphene membranes, even if the majority of experimental studies have reported a decrease in their values as a result of the presence of different types of defects. All these findings are summarized in Table 1.

Table 1. Young's modulus and tensile strength of 2D materials measured from different experiment methods. (F: few-layer; /: armchair/zigzag directions.)

Material	Layers	Young's modulus (GPa)	Strength (GPa)	Method	Ref.
Graphene	1	1000 ± 100	130 ± 10	Nanoindentation	15
Graphene (CVD)	1	1000 ± 50	103-118	Nanoindentation	57
Graphene (CVD)	1	920	50-60	*In situ* tension	48
Graphene (Wrinkled)	1	160	35	Nanoindentation	75
	1	60-299	–	Interferometry	78
GO	1-3	207.6 ± 23.4	–	Nanoindentation	59
	1	150 ± 30	4.4 ± 0.6	Nanoindentation	79
h-BN	1-9	865 ± 73	70.5 ± 5.5	Nanoindentation	17
h-BN (CVD)	2	223 ± 16	–	Nanoindentation	73
MoS_2	1	270 ± 100	22 ± 4	Nanoindentation	18
	1	210 ± 50	26.8 ± 5.4	Nanoindentation	80
	5-10	330 ± 70	–	Nanoindentation	60
	3-11	246 ± 35	–	Buckling method	54
MoS_2 (CVD)	1	264 ± 18	–	Nanoindentation	61
WS_2	3-8	330 ± 70	–	Buckling method	54
WS_2 (CVD)	1	272 ± 18	–	Nanoindentation	61
$MoSe_2$	1-2	177.2 ± 9.3	4.8 ± 2.9	Tension test	62
	5-10	224 ± 41	–	Buckling method	54
WSe_2	5-12	167.3 ± 6.7	12.4	Nanoindentation	63

	4-9	163 ± 39	–	Buckling method	54
$MoTe_2$	F	110 ± 16	5.6 ± 1.3	Nanoindentation	64
BP	F	27.2 ± 4.1/ 58.6 ± 11.7	2.31 ± 0.71/ 4.79 ± 1.43	Nanoindentation	68
	F	27.38 ± 2.35/ 65.16 ± 4.45	–	Nanoindentation	69
	F	35.1 ± 6.3/ 93.3 ± 21.8	–	Buckling method	70
$Ti_3C_2T_x$	1-2	330 ± 30	17.3 ± 1.6	Nanoindentation	47
$Ti_3C_2T_x$	1	484 ± 13	15.4 ± 1.92	*In situ* tension	49
$Nb_4C_3T_x$	1	386 ± 13	26 ± 1.6	Nanoindentation	71

2.2.2. Toughness

Toughness is another key parameter for the application of 2D materials in nanocomposites. Unlike strength that characterizes the fracture of defect-free materials, toughness describes the failure of materials with pre-existing cracks. The fracture toughness is, therefore, more frequently used for engineering materials such as composites and the failure mechanisms of 2D materials can be divided into brittle failure, ductile failure and phonon instability.

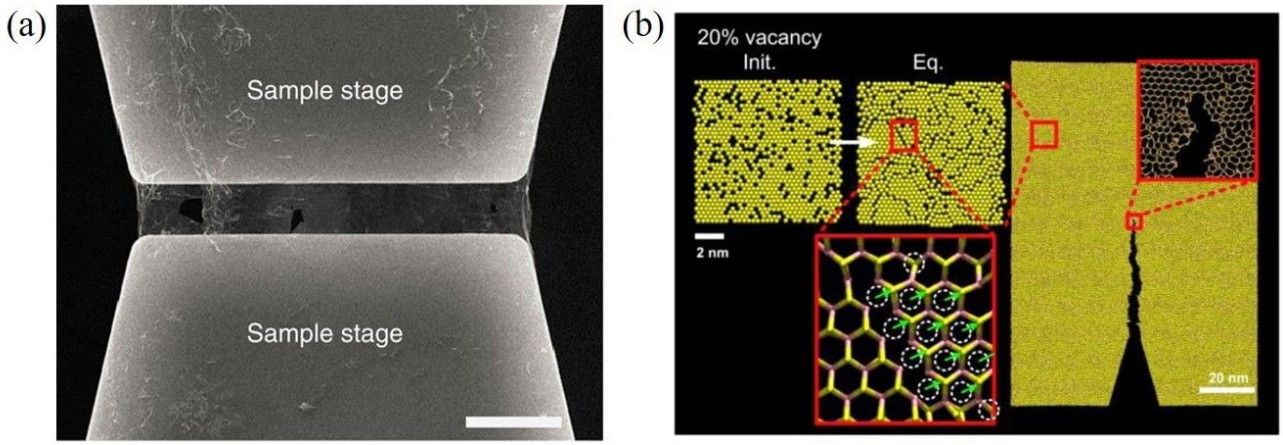

Figure 4. (a) Suspended monolayer graphene over a tension stage for fracture toughness measurement. Scale bar, 5 μm. Reproduced with permission from [81]. Copyright 2014 Nature Publishing Group. (b) Crack propagation in monolayer MoS_2 with line defects. Reproduced with permission from [82]. Copyright 2016 American Chemical Society.

View Article Online
DOI: 10.1039/D4NR01356E

In situ tensile tests within an SEM chamber were first used to characterize the fracture behaviour of graphene [81]. As shown in Figure 4a, a pre-cracked graphene monolayer was stretched in a tension stage and the stress-strain curve was used to evaluate the fracture behaviour. According to Griffith's theory of brittle fracture [83], the critical stress for the initiation of fracture σ_c is given as $\sigma_c = \sqrt{2\gamma E/\pi a_0}$, where a_0 is the initial crack length, γ is the surface energy and E is the stiffness of the material. The critical stress intensity factor K_{IC} ($= \sigma_c\sqrt{\pi a_0}$), and the strain energy release rate G_C ($= \sigma_c^2 \pi a_0/E$) are generally used to characterize the fracture toughness [84]. The average values for graphene are $K_{IC} \approx 4$ MPa m$^{1/2}$and $G_C \approx 15.9$ J m^{-2}, which implies that graphene is a brittle material since the product $\sigma_c\sqrt{a_0}$ remains constant around an average value of 2.25 MPa m$^{1/2}$. Recently, it has been shown that the propagation of cracks in graphene can be monitored by the use of *in situ* Raman mapping [85]. Multilayer graphene exhibits a larger fracture toughness (12.0 ± 3.9 MPa m$^{1/2}$) than monolayer resulting from different fracture mechanisms [86]. The cracks propagate along different directions and form rough edges in multilayer graphene. A higher energy is therefore required for crack propagation. In addition, recoverable interlayer slippage leads to a driving force relaxation and elastic strain energy dissipation. Polycrystalline graphene also shows higher fracture toughness compared with the single-crystal graphene [87, 88]. The grain boundaries in polycrystalline graphene lead to complex crack propagation paths and higher energy dissipation while the stress is less concentrated at the crack tip due to the larger deformation area.

For monolayer h-BN, the value of K_{IC} (8.7 MPa$\sqrt{\text{m}}$) is similar to that of graphene, while the value of G_C (86.35 ± 45.22 J m^{-2}) is one order of magnitude higher than both its energy release rate for brittle Griffith fracture and that for graphene [89]. This is the result of its asymmetric edge elastic properties, crack deflection and branching occuring repeatedly at the crack tip and edge swapping during crack propagation, that toughens the material and enables stable crack propagation. Wang *et al.* [82] observed the transition from brittle to ductile fracture in MoS_2 with an increase in defect density. The tensile strength of moderately-defective MoS_2 is larger than that of graphene. This is because line defects in

View Article Online
DOI: 10.1039/D4NR01356E

MoS_2 influence crack propagation as shown in Figure 4b, while holes in graphene have no effect on the crack propagation.

Different strategies have been used to improve the fracture behaviour of 2D materials. The fracture toughness of multilayer graphene was increased from 16 to 39 J m^{-2} through chemical functionalization [90]. Apart from the distinct crack propagation in multilayer samples, oxygen groups induce local strain fields, thus a higher energy is required for crack growth. Secondly, defect engineering, such as inducing high-density defects, can lead to the transition from brittle to ductile fracture in graphene and MoS_2 [82]. Finally, kirigami-type structures have been found to undergo large strains without fracture, as ripples in a kirigami structure can stiffen the nanosheets significantly [91].

3. "Model" nanocomposites

To achieve mechanical reinforcement in bulk polymer nanocomposites, 2D nanosheets need to be dispersed into the matrix and the stress transferred from the matrix to the 2D nanosheets via an interfacial shear force when the composites are subjected to external loading. Since the elastic modulus of 2D nanosheets is much higher than that of the polymer matrices, it means that in a uniform strain situation, a much larger stress can be sustained [92]. It is difficult, however, from the study of bulk polymer nanocomposites to extract conclusions regarding the reinforcing mechanisms originating from individual monolayer or few-layer 2D materials due to a number of complexities. These include agglomeration and orientation of the fillers, the formation of filler folds or loops during processing and the size distribution of the fillers. In order to fully understand and model the stress transfer mechanisms originating from the geometric characteristics and the intrinsic mechanical properties of 2D materials, researchers have devised the study of "model" polymer nanocomposites where individual flakes are sandwiched between two polymer layers. Studies on model nanocomposites can provide guidance on how to balance different factors, such as the lateral dimensions of the flakes, the layer number, any chemical functionalization and the effects of defects or wrinkles, to achieve optimal

View Article Online
DOI: 10.1039/D4NR01356E

mechanical reinforcement of polymers using 2D nanosheets. There are some reports in which flakes are deposited on top of a flexible polymer substrate and strain is subsequently applied to the polymer beam. These studies are also very helpful to achieve a detailed understanding of the stress transfer mechanisms.

3.1. Theories of reinforcement in polymer matrix: the shear-lag theory

The ultimate mechanical performance of polymer nanocomposites depends not only upon the mechanical properties of the incorporated 2D nanosheets, but is also subject to the interfacial interaction between the nanosheets and the matrix. A strong interfacial interaction means that the stress in a matrix can be transferred efficiently to the nanosheets via shear and reinforcement can thus be achieved. The stress transfer mechanism from a matrix to 2D nanosheets can be described using shear-lag analysis [93] based upon elastic deformation with no interfacial sliding. When a strain is applied to the matrix with shear modulus G_{m}, the strain in the 2D nanosheet ε_f can be calculated from

$$\varepsilon_{\mathrm{f}}(x) = \varepsilon_{\mathrm{m}}\left[1 - \frac{\cosh\left(ns\frac{x}{l}\right)}{\cosh\left(ns/2\right)}\right] \tag{4}$$

where ε_{m} is the strain in the matrix, l is the length of the nanosheet at the x direction, s ($= l/t$) is the aspect ratio of the flake, $n = \sqrt{\frac{2G_{\mathrm{m}}}{E_{\mathrm{f}}}\frac{t}{T}}$ is the shear-lag parameter describing the interfacial shear stress transfer efficiency, E_{f} is the Young's modulus of the filler and t and T are the thicknesses of the nanosheet and the surrounding matrix.

View Article Online
DOI: 10.1039/D4NR01356E

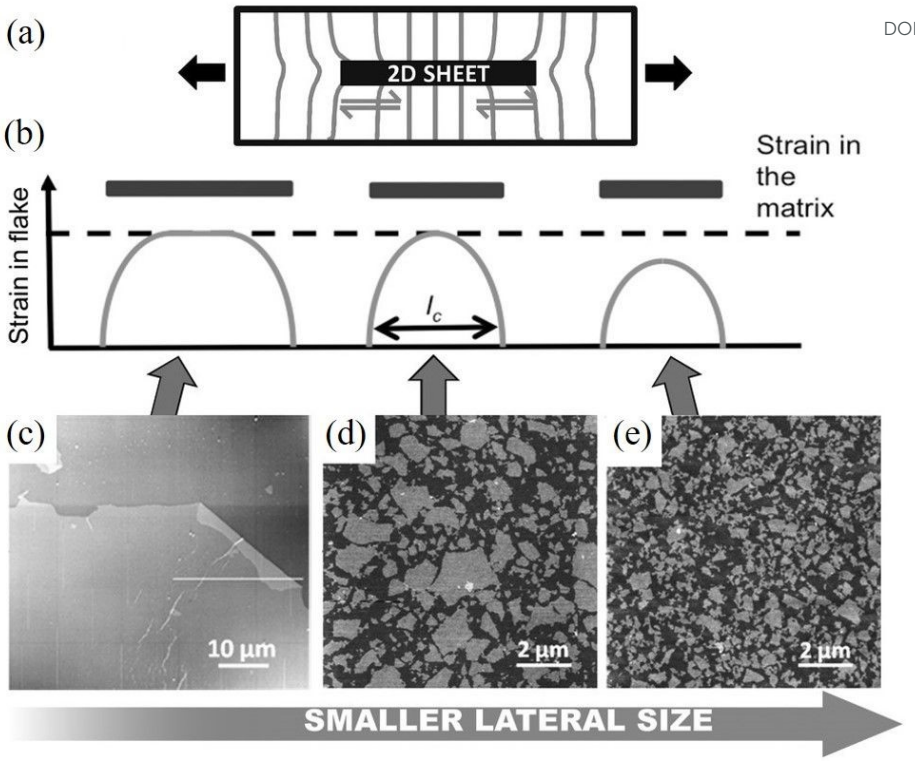

Figure 5. (a) Illustration of stress transfer from a matrix to 2D nanosheets through shear at the fibre-matrix interface. The distortion of the stress lines comes as a result of the differences in the Young's modulus between the matrix and the fibre. (b-e) Variations of strain transfer efficiency with lateral size of 2D nanofiller. When the lateral size is large, strain transfer efficiency from the matrix to 2D nanosheet is high; when the lateral size reduces to the critical length l_c, only strain at the centre position of the nanosheet equals to strain in the matrix; as the lateral size continues to decrease, the strain transfer efficiency is poor. Reproduced with permission from [10]. Copyright 2016 Wiley-VCH Verlag GmbH & Co. KGaA.

When strain is applied to a nanosheet, the strain begins at the edges and extends to match the strain level of the matrix at a certain distance away from the filler edge; 90% of this distance is defined as the critical length l_c, as seen from Figure 5b. Only the central part of the flakes delivers effective reinforcement, while the critical length region reinforces the composite relatively poorly. The maximum strain in the graphene occurs at the centre of the flake where x=0 and the maximum interfacial shear stress occurs at the edges. The lateral size of the nanosheet is therefore an important

View Article Online
DOI: 10.1039/D4NR01356E

parameter. When the lateral size is large, efficient stress transfer and mechanical reinforcement can be achieved; as the lateral size decreases, insufficient stress transfer takes place, as seen from Figure 5c to 5e. To achieve good mechanical reinforcement, the size of the nanosheets needs to be about $10\times l_c$. Moreover, mechanical reinforcement also depends on the strength of the interface, the interfacial shear strength. The interfacial shear stress τ is given by

$$\tau(x) = nE_{\mathrm{f}}\varepsilon_{\mathrm{m}}\frac{\sinh\left(ns\frac{x}{l}\right)}{\cosh\left(ns/2\right)} \tag{5}$$

which shows that the interfacial shear stress increases with an increase of the applied strain. When the interfacial shear stress surpasses the interfacial shear strength, sliding occurs as a result of the failure of the interface and stress will only be transferred by friction. This will result in poor stress transfer and insufficient mechanical reinforcement. The onset of interfacial sliding can be obtained by setting the maximum shear stress equal to the interfacial shear strength τ_c which corresponds to a critical strain applied to the substrate [20]:

$$\varepsilon_{\mathrm{c}} = \frac{\tau_{\mathrm{c}} l}{\beta E_{\mathrm{f}}}\coth\left(\frac{\beta l}{2}\right) \tag{6}$$

where $\beta = \sqrt{k_{\mathrm{m}}/E_{\mathrm{f}}}$, k_{m} is the effective stiffness of the substrate. This strain cannot be directly measured and the interfacial shear strength can be determined from the measurements of the plateau strain at the centre of the flake ε_{p}, given that the sliding zones develop from the edges and approach the centre:

$$\varepsilon_{\mathrm{p}} = \frac{\tau_{\mathrm{c}} l}{2E_{\mathrm{f}}} \tag{7}$$

It can be realised from Eq. (7) that the level of stress transferred from the matrix to the nanofiller can be improved by increasing the lateral size of the nanosheets and by having a high interfacial shear strength (e.g. by chemical functionalization).

3.2. Model monolayer nanocomposites

View Article Online
DOI: 10.1039/D4NR01356E

In order to understand the mechanics of reinforcement it is desirable to know the distribution of strain in the 2D nanofillers. The strain in the nanosheets, the stress transfer mechanisms and the mechanical reinforcement can be evaluated using Raman spectroscopy and photoluminescence (PL) spectroscopy as strain induces changes in phonon frequencies and band gaps. This can offer invaluable information with regards to both the mechanical properties of the 2D nanosheets and their polymer-based nanocomposites.

Raman spectroscopy has been widely used to study model nanocomposites under strain. The strain induces shifts in the characteristic Raman bands of 2D materials, such as the *G* [94-96] and *2D* [97-99] bands of graphene, the *G* mode of h-BN [100], the E^1_{2g} and A_{1g} modes of MoS_2 [101-104] and WS_2 [105-107], and the A_{1g} mode of $Ti_3C_2T_x$ [108]. The shifts of phonon modes are generally proportional to the applied strain and this allows the determination of strain in 2D nanosheets. The mode-specific Grüneisen parameter is calculated based on the following expression for either uniaxial or biaxial strain for a specific phonon mode [95]

$$\gamma_{\mathrm{m}} = -\frac{1}{\omega_{\mathrm{m}}^0}\frac{\partial \omega_{\mathrm{m}}}{\partial \varepsilon} \tag{8}$$

where the strain $\varepsilon = \varepsilon_x + \varepsilon_y$; for uniaxial strain, $\varepsilon_x = \varepsilon$ and $\varepsilon_y = -\nu\varepsilon$ where ν is the Poisson's ratio; ω_{m}^0 is the m mode frequency at zero strain.

The strain in graphene can be monitored by observing the 2D band shifts of a monolayer deposited onto a flexible polymer substrate. Reported values of the rate of band shift are found to vary as a result of slippage [109] or wrinkling [110] and a value of around −60 cm^{-1}/% for uniaxial strain has been regarded as a reference for good stress transfer [95]. Gong *et al.* [19] studied stress transfer in a graphene/SU-8/polymethyl methacrylate (PMMA) model composite under uniaxial tension using the Raman 2D band shift. Monolayer graphene (tens of micrometres in lateral dimensions) was exfoliated from graphite and the Raman spectra at the centre of the nanosheets were obtained. For strains under 0.4%, the 2D band shift is −50 cm^{-1}/% and the shear-lag theory works well. The interfacial shear stress was

View Article Online
DOI: 10.1039/D4NR01356E

calculated to be around 2.3 MPa. For strains above 0.4%, interfacial sliding occurs as shown in Figure 6a and the interfacial behaviour can no longer be predicted by the shear-lag theory. The interfacial shear stress drops to about 0.3−0.8 MPa. These values are relatively low compared to the values of carbon fibre composites (~ 20−40 MPa) [111], as adhesion between graphene and the matrix is relatively poor. Subsequently, Young *et al.* [112] used Raman mapping to capture the strain distribution in monolayer graphene embedded between SU8 and SU8/PMMA. For strains under 0.6%, the 2D band shift is −61 ± 2 cm^{-1}/% and the strain distribution is homogeneous. For strain above 0.6%, the strain distribution becomes inhomogeneous due to the formation of cracks that are also responsible for the poor interfacial shear strength (~0.25 MPa). Jiang *et al.* [20] later studied the interfacial shear behaviour in a graphene/PET system. For strains from 0 to 1.2%, the 2D band shift was found to be of the order of −52.5 cm^{-1}/%. In this case, at low strain levels, above 0.3% interfacial sliding occured and a nonlinear shear-lag theory was proposed to describe the stress transfer mechanism (Figure 6b). According to this theory, the onset of interfacial sliding can be predicted by setting the maximum shear stress equal to the interfacial shear strength. In their experiments, the interfacial shear strength was found to range from 0.7 MPa for a specimen with a length of 12.4 μm to 0.5 MPa for a specimens with a length of 17.2 μm, assuming E^{2D} = 350 N/m. The maximum strain that could be transferred from the substrate to graphene was in the range of 1.2−1.6%. Anagnostopoulos *et al.* [113] investigated how doping and edge effects (bond length and angle and edge chirality) affect stress transfer in a graphene/SU-8/PMMA system. The lateral size of graphene was of the order of tens of micrometres. It was found that the stress transfer may deviate from the shear-lag theory near the edges (~2 μm), induced by residual stress and doping. According to the authors, the overall length for efficient load transfer was estimated to be ~4 μm, meaning that for flakes that are simply supported on a substrate, a length of ~8 μm is needed for efficient loading. The interfacial shear strength was about 0.4 MPa. The morphology of the flake under study in the specific investigation makes the interpretation of results challenging as the short width of the flake leads to the maximisation of the interfacial shear stress

View Article Online
DOI: 10.1039/C4NR01356E

under strain at a very short length, within the spatial resolution of the Raman measurements (of the order of 1-2 μm). Additionally, the mechanical exfoliation process and the subsequent deposition on substrates (with varying degrees of roughness) can lead to high levels of residual stresses. There is a caveat that the lateral strain of graphene is often not $\varepsilon_y = -\nu\varepsilon$ in a specimen under uniaxal strain. Where the strain of a substrate is fully transferred to graphene, its lateral strain is either determined by the Poisson's ratio of the substrate, or zero (e.g. during flexure of a thin beam). This results in complexity in obtaining strain from the shift of the 2D mode, whereas the G mode with clearer mechanical meaning may be a better alternative. A number of key factors such as the interfacial shear stress have been quantitatively determined through these studies, along with the intrinsic mechanical properties of the nanosheets, which are helpful for the optimization of the mechanical reinforcement in bulk polymer nanocomposites.

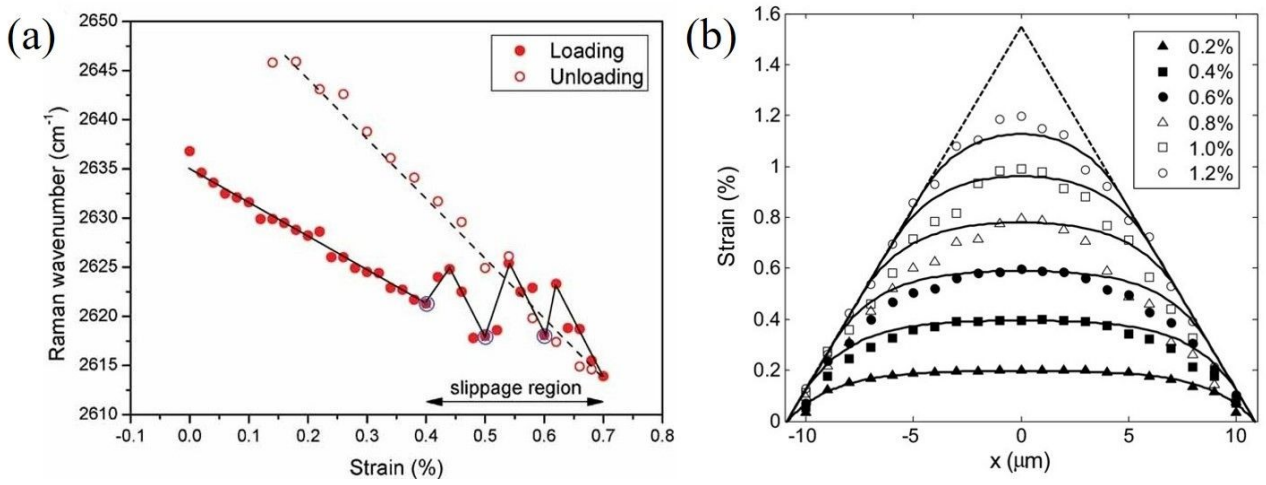

Figure 6. (a) Raman 2D peak shifts of graphene with applied uniaxial strain under loading and unloading. For strains higher than 0.4%, interfacial slippage occurs. Reproduced with permission from [19]. Copyright 2010 Wiley-VCH Verlag GmbH & Co. KGaA. (b) Experimental (dots) and nonlinear shear-lag theory prediction (lines) values of strain distribution from edge to centre of graphene under different loading conditions. Reproduced with permission from [20]. Copyright 2013 Wiley-VCH Verlag GmbH & Co. KGaA.

View Article Online
DOI: 10.1039/D4NR01356E

Stress transfer from the polymer substrate to 2D nanosheets has also been studied for other materials [107, 108]. Wang *et al*. [107] followed the stress transfer of a WS_2/SU8/PMMA model composite under uniaxial tension through monitoring the downshift of the Raman E^1_{2g} mode. The strain distributions in an uncoated WS_2 nanosheet at 0% and 0.55% are shown in Figure 7. At 0% applied strain, the centre of the flake is under 0% strain while the edge of the flake is under compression, as a result of the specimen preparation procedure. At 0.55% applied strain, the strain builds up from the edges and reaches about 0.55% strain towards the centre of the flake. This means that stress can be transferred from the substrate to the nanosheet effectively. The shear stress at the edges of the nanosheets was calculated to be about 1.1 MPa, which is similar to the values for graphene but significantly lower than that of the carbon fibres in composites (~20-40 MPa). For monolayer WS_2 coated with an SU8 layer, a crack was observed at the middle of the flake upon the application of 0.55% strain. This result, using the modulus of WS_2 (~ 272 GPa), suggests that the fracture strength of this monolayer WS_2 flake was of the order of ~1.5 GPa. Liu *et al*. [108] studied interfacial stress transfer in $Ti_3C_2T_x$ MXene-polymer composites. The strain distributions and interfacial shear stresses of a monolayer flake are illustrated in Figure 7d and 7e. At 0.2% and 0.4% strain, the strain distributions still follow shear-lag behaviour and the shear stress at the edge is estimated to be 2.0 and 4.0 MPa, respectively. It was concluded that $Ti_3C_2T_x$ MXene flake with a length of >10 μm and a thickness of 10s of nanometers would be a good candidate for mechanical reinforcement in polymer matrices.

View Article Online
DOI: 10.1039/D4NR01356E

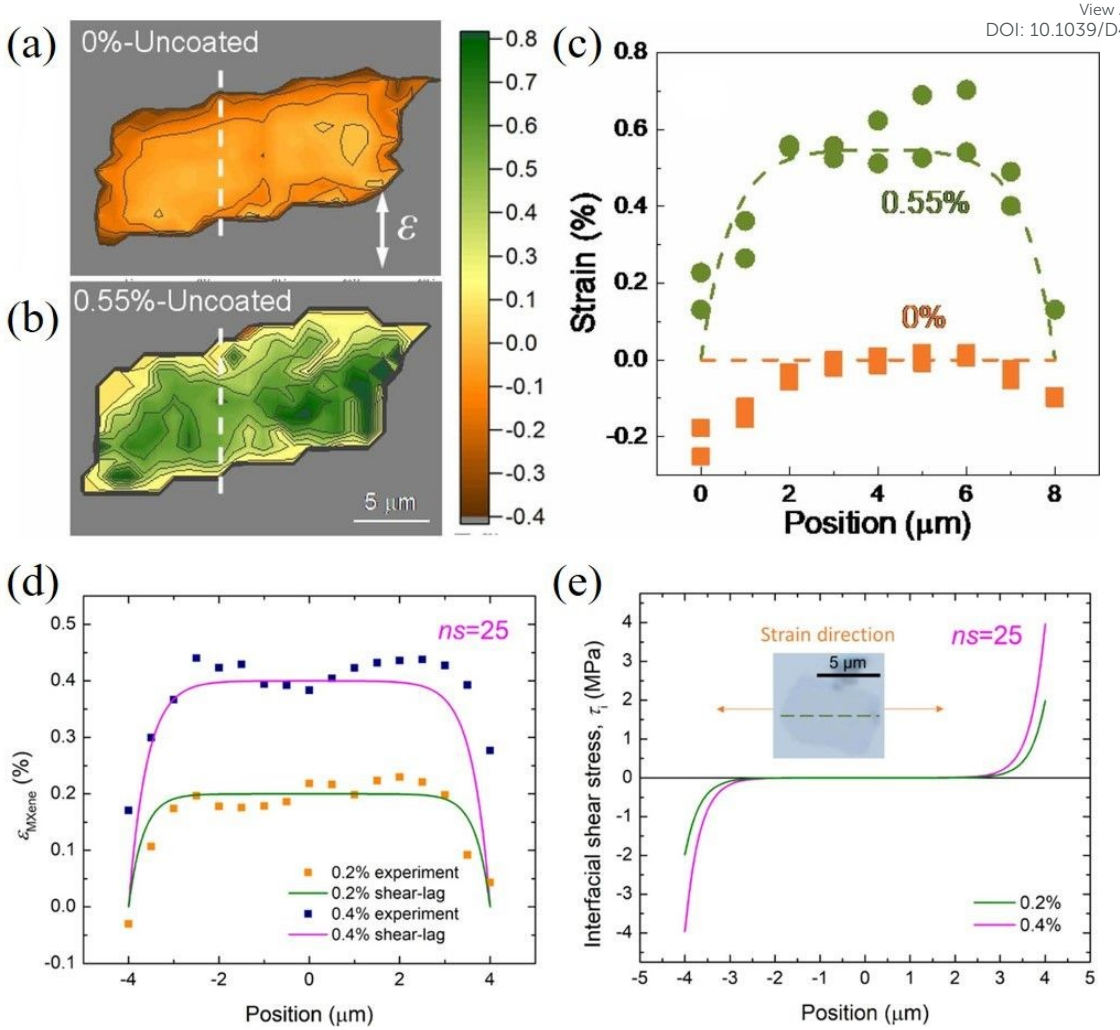

Figure 7. (a, b) Strain distributions in uncoated WS_2 nanosheets at 0% and 0.55% applied strain. (c) Strain distributions along the white dashed lines in (a) and (b), where the points represent experimental values and the dashed lines represent values calculated from shear-lag theory. Reproduced with permission from [107]. Copyright 2020 IOP Publishing Ltd. (d) Strain distributions and (e) interfacial shear stresses of a monolayer $Ti_3C_2T_x$ flake under 0.2% 0.4% strain. Reproduced with permission from [108]. Copyright 2022 American Chemical Society.

The stress transfer from a matrix to 2D nanosheets with a direct band gap can also be studied by photoluminescence (PL) spectroscopy [114-116]. Liu *el al* [114] followed the strain transferred from PDMS to MoS_2 by PL mapping as shown in Figure 8a and 8b. It was found through the observation of PL peak shifts that about 10% of the applied strain can be transferred from PDMS to MoS_2. Finite element

View Article Online
DOI: 10.1039/D4NR01356E

modelling further showed that an increase in substrate modulus will improve the stress transfer under the same interfacial conditions. This is in good agreement with observations from a number of experimental investigations on graphene-polymer nanocomposites reported in the literature, where it was concluded that an increase of the modulus of the matrix leads to an increase in the effective graphene modulus within the composite [16]. In a recent study, the stress transfer mechanism from a polymer matrix to monolayer MoS_2 was studied in detail through strain-dependent PL spectroscopy [115]. With increasing strain, the strain distribution in monolayer MoS_2 can be described by shear-lag, partial-debonding and total-debonding models. It was concluded that the shear-lag model overestimates the strain in the flake when slippage takes place, as shown in Figure 8c and 8d. Additionally, any errors originating from the incorrect use of the shear-lag model will increase with loading, as a result of the slippage length increasing further with loading.

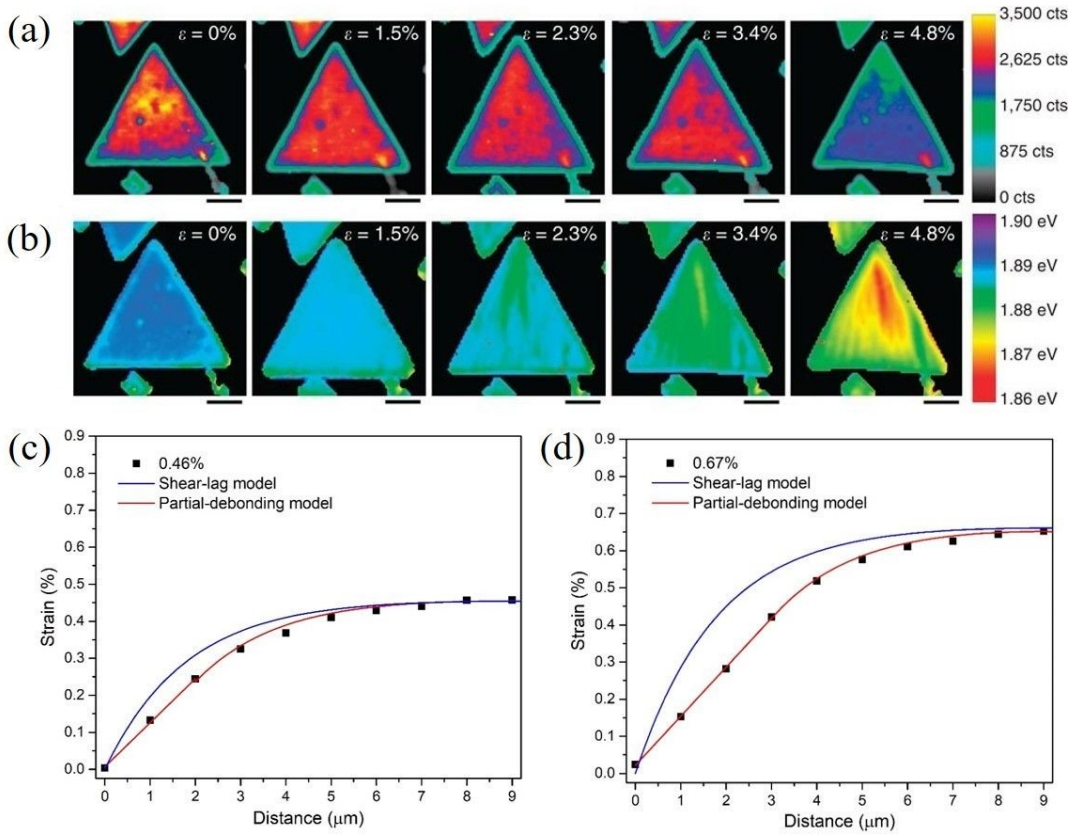

Figure 8. PL A exciton (a) intensity and (b) peak mapping of MoS_2 with applied strain increasing from 0 to 4.8%. (Scale bar, 4 μm). Reproduced with permission from [114]. Copyright 2014 Nature Publishing Group. Strain distribution in monolayer MoS_2 at (a) 0.46% and (b) 0.67% strain. Both shear-lag model

View Article Online
DOI: 10.1039/D4NR01356E

and partial-debonding model were used to fit the experimental results. Reproduced with permission from [115]. Copyright 2023 Elsevier.

The geometry of 2D materials and their orientation with the loading direction can affect the stress transfer from matrix to the inclusion [117-119]. Manikas *et a*l. [117] studied the transfer of stress from a PMMA substrate to graphene ribbons aligned to the loading direction. In this way, truly axial deformation was achieved, and the effect of off-axial shear was avoided. The authors derived an inverse length parameter that governs the stress transfer process. The transfer lengths were in the range of 500 to 1000 nm, which are lower than cases of randomly oriented 2D materials with irregular shapes. Out-of-plane deformations such as wrinkling and crumping often occur during the preparation of 2D materials. These out-of-plane deformations can affect stress transfer and the level of mechanical reinforcement. Li *et al.* [120] studied the stress transfer mechanisms from a PET matrix to wrinkled monolayer CVD graphene using Raman spectroscopy. The microsctructure of CVD graphene consists of islands where the inside of the island is flat while the material separating the flat graphene is wrinkled graphene. Strain increases towards the centre of each separated area as shown in Figure 9a. The observed 2D band shift of the wrinkled part is −12.8 cm^{-1}/% is therefore about 75% lower than that of the flat part (−60 cm^{-1}/%). In subsequent studies [121, 122], it was found that wrinkling will not affect the stress transfer in a composite significantly if the flake is not delaminated from the matrix [121]. Moreover, small amplitude wrinkling can improve the stress transfer efficiency of few-layer flakes due to a higher interfacial shear stress [122]. In a recent study, the difference between strain relaxation in graphene and MoS_2 was investigated by Yu *et al.* [123]. Monolayer graphene and MoS_2 were deposited on a PDMS substrate and AFM was used to extract the spacing between wrinkles. According to the authors, at lower strain, the 2D nanosheets prefer to delaminate to generate new wrinkles; at higher strain, the 2D nanosheets prefer to slip to enlarge the existing wrinkles as shown in Figure 9b. Furthermore, MoS_2 is able to sustain a larger strain before relaxing and the maximum interfacial

View Article Online
DOI: 10.1039/D4NR01356E

friction of MoS_2 on PDMS (7.7 ± 2.5 MPa) is higher than that of graphene (3.8 ± 0.8 MPa). This is because the interfacial adhesion energy between MoS_2 and PDMS is stronger compared to the graphene counterpart. It should be noted that the PDMS substrate was described by the manufacturer as a gel with adhesive properties, which most likely resulted in higher values of interfacial adhesion and friction. In another study, Zhang *et al.* [124] studied the strain relaxation of WS_2 on a PDMS substrate using PL spectroscopy. It was found that the formation of wrinkles depends on the orientation between the flake edge and the tensile axis; when an edge of the flake is parallel to the tensile axis, the wrinkles are distributed uniformly.

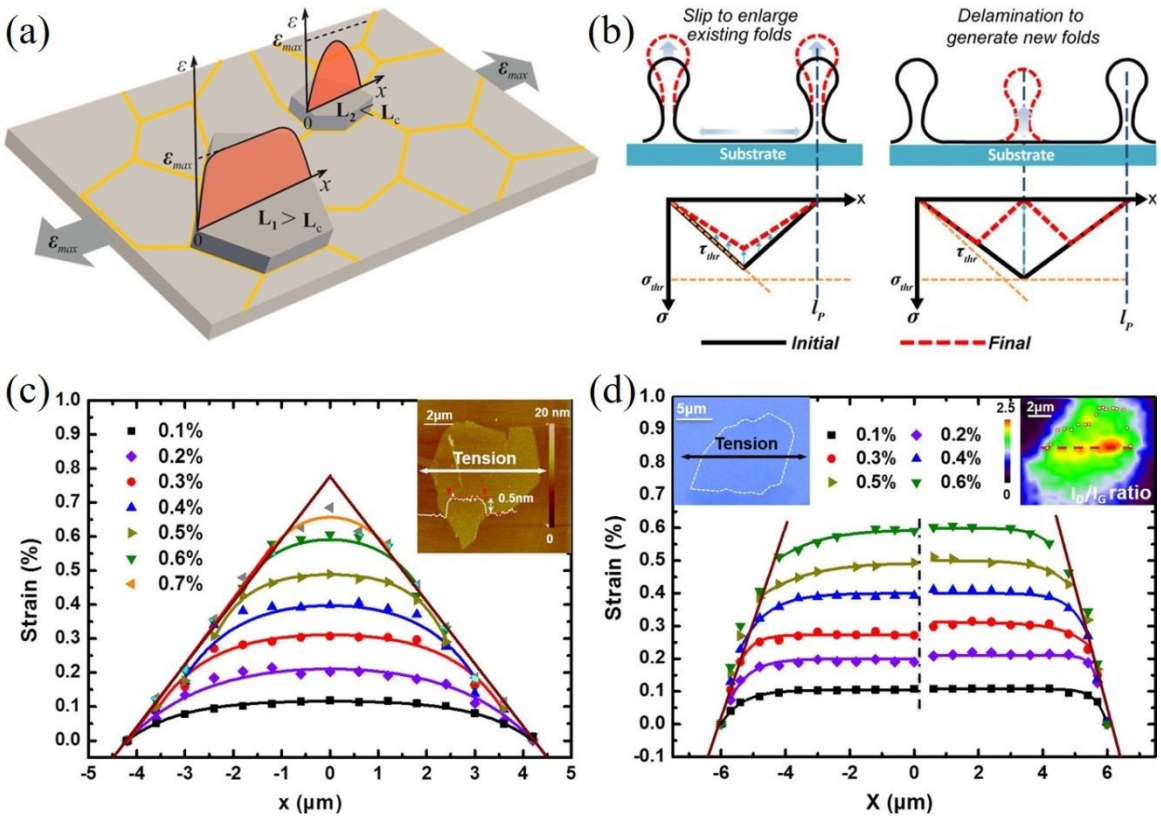

Figure 9. (a) Strain transfer from a substrate to a wrinkled graphene nanosheet. Reproduced with permission from [120]. Copyright 2015 American Chemical Society. (b) Mechanism for the formation of wrinkles in 2D nanosheets: slip to enlarge existing folds and delamination to generate new folds. Reproduced with permission from [123]. Copyright 2020 American Chemical Society. Strain distributions in (c) pristine graphene and (d) oxidized graphene at different applied strain. Reproduced with permission from [125]. Copyright 2016 American Chemical Society.

View Article Online
DOI: 10.1039/D4NR01356E

As a result of the weak vdW forces between the 2D nanosheets and the matrix, interfacial slippage occurs at a relatively low strain, especially when the length of the flakes is lower than the critical length and the 2D nanosheets are not able to reinforce efficiently. Non-covalent or covalent bonds between the nanosheets and substrate can be used to improve the interfacial shear strength [125-127]. Wang *et al.* [125] studied the effects of functionalization on the stress transfer and mechanical properties of a graphene/PMMA model nanocomposite as shown in Figure 9c and 9d. On one hand, it was found that the interfacial shear strength quadrupled to 1.7 MPa compared to pristine graphene. On the other hand, the functional groups induced defects in the graphene and in turn, the defects degraded the mechanical properties of graphene. Therefore, a balance needs to be kept between the degree of functionalization and the increased interfacial shear strength. The effect of chemical functionalization on the interfacial stress transfer and mechanical properties of model composites based on 2D nanosheets is a field which can provide important information regarding the reinforcement mechanisms of different nanosheets and there is plenty of scope for future investigations.

3.3. Model few- and many-layer nanocomposites

In contrast to monolayer 2D nanosheets, few-layer and multi-layer nanosheets are most commonly used as fillers in polymer nanocomposites. In this case the strain is transferred from the matrix to the outer layer of the nanosheets, and then transferred to the inner layer via shear forces. Therefore, in addition to the interfacial shear strength, the interlayer interactions also play an important role in controlling effective reinforcement from 2D nanosheets. This section focuses upon the studies of few-layer 2D nanosheets, where it is easy to identify contributions from interlayer stress transfer and interactions.

Gong *et al* [128] studied the behaviour of monolayer and few-layer graphene/polymer model composites under axial tension with an emphasis on the effect of layer number on mechanical

View Article Online
DOI: 10.1039/D4NR01256E

reinforcement. Firstly, it was found that the 2D band shift of uncoated bilayer graphene (−31 cm^{-1}/%) is much lower compared with the coated bilayer graphene (−53 cm^{-1}/%) and coated or uncoated monolayer graphene (−59 cm^{-1}/%). This implies that interlayer stress transfer is relatively poor in graphene. Reduced interlayer stress transfer can further be realised from the behaviour of the coated monolayer, bilayer, trilayer and multi-layer graphene composites where the 2D band shifts are −52 cm^{-1}/%, −53 cm^{-1}/%, −43 cm^{-1}/%, −8 cm^{-1}/%, respectively, as seen from Figure 10a.

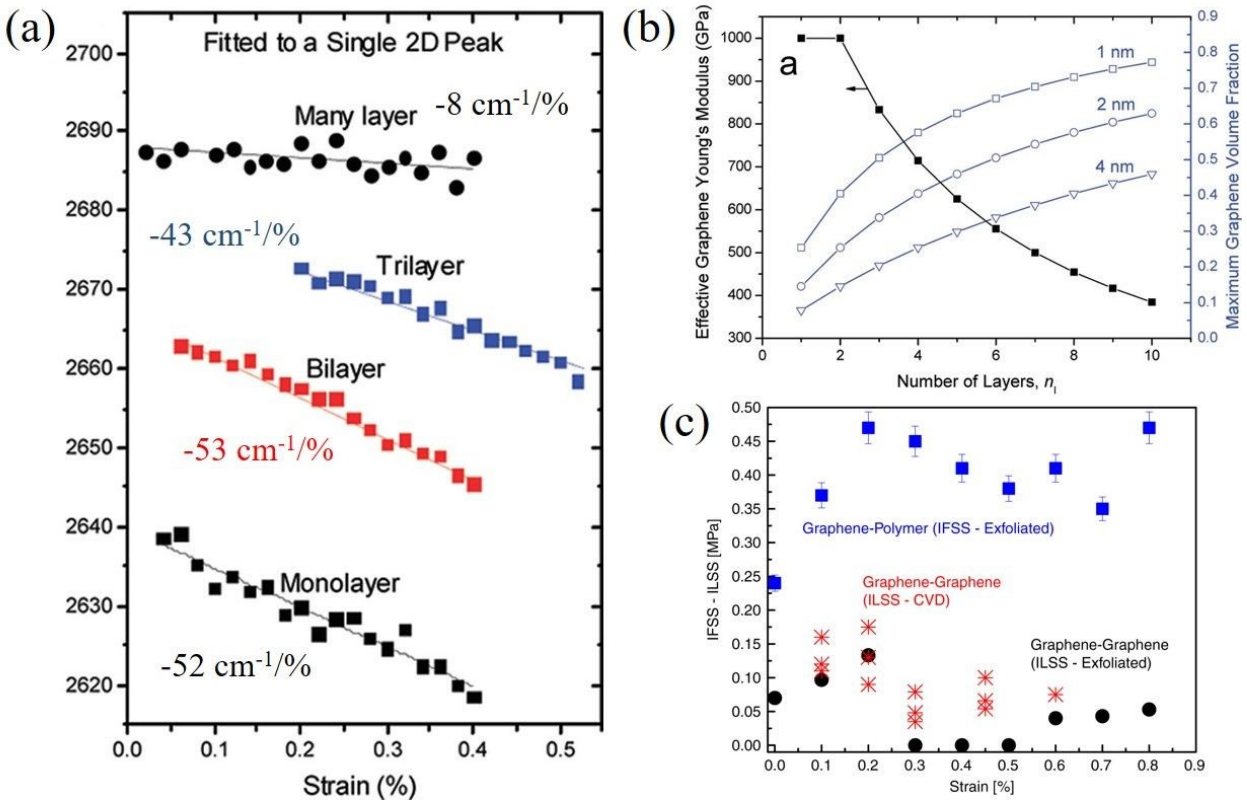

Figure 10. (a) Raman 2D shifts of monolayer, bilayer, trilayer and multilayer graphene in a polymer/graphene/polymer model composite. (b) Variations of effective elastic modulus of graphene with layer number. Reproduced with permission from [128]. Copyright 2012 American Chemical Society. (c) Interfacial shear stress of graphene-polymer and graphene-graphene. Reproduced with permission from [129]. Copyright 2020 Nature Publishing Group.

The *2D* band shift is related to the effective Young's modulus of *2D* nanosheets as

View Article Online
DOI: 10.1039/D4NR01356E

$$E_{\mathrm{R}} = E_{\mathrm{g}}\left[\frac{\partial\omega_{2\mathrm{D}}/\partial\varepsilon}{\left(\partial\omega_{2\mathrm{D}}/\partial\varepsilon\right)_{\mathrm{ref}}}\right] \quad (9)$$

where E_{R} is the Young's modulus derived from Raman spectroscopy, E_{g} is 1.05 TPa, and $\left(\partial\omega_{2\mathrm{D}}/\partial\varepsilon\right)_{\mathrm{ref}}$ is −60 cm^{-1}/% [23]. This means that monolayer and bilayer graphene have similar values of effective Young's modulus, and a further increase of layer numbers will degrade the effective elastic modulus (as a result of insufficient interlayer stress transfer efficiency, 0.6–0.8) of graphene as shown in Figure 10b.

Interfacial stress transfer for both mechanically-exfoliated and CVD-grown bilayer graphene deposited on a PMMA/SU8 substrate have been studied using Raman spectroscopy as shown in Figure 10c [129]. The interfacial shear stress between the graphene and polymer was found to be about 0.45 MPa, whereas the maximum interfacial shear stress between the graphene layers was only about 0.13 MPa and this value dropped to zero (adhesion being lost, leaving only friction) with an increase in strain. This means that the interfacial interactions within graphene are relatively weak and interlayer stress transfer is poor. Interestingly, in this study, the interlayer strain that was transferred from the bottom to top graphene layers is only about half of the interfacial strain that was transferred from the polymer substrate to the bottom graphene layer. In a recent study, it was found that stress can be transferred within few-layer graphene with a ladder-like morphology effectively as all the layers adhere to the surrounding polymer and interlayer slippage is suppressed [130].

In contrast to graphene, the effective Young's modulus of h-BN does not decrease with increasing layer number and this suggests a major advantage in using h-BN in polymer nanocomposites [100, 131]. Androulidakis *et al.* [100] studied the stress transfer in a few-layer h-BN /SU-8/PMMA system. The $E_{2\mathrm{g}}^{+}$ and $E_{2\mathrm{g}}^{-}$ ($E_{2\mathrm{g}}^{+}$ mode is perpendicular to the applied strain and $E_{2\mathrm{g}}^{-}$ is parallel to the applied strain) band shifts are −8.3, −7.7, −9.8 cm^{-1}/% and −24.2, −23.7, −27.1 cm^{-1}/% for the number of layers ranging from 2 to 4 (Figure 11a and 11b), respectively. This shows that the layers are strongly bonded

and few-layer h-BN is strained as a whole unit, contrary to what is observed in graphene, as a result of the high sliding energy of h-BN, a finding identical to that concluded from AFM indentation experiments [17]. Moreover, the interlayer stress transfer efficiency of h-BN was determined to be 0.99 as shown in Figure 11c, which is much higher than graphene (0.6-0.8) [131]. These findings indicate that multilayer h-BN can be considered to be more effective than multilayer graphene for the reinforcement of polymers. In another study, the interlayer stress transfer efficiency of few-layer MoS_2 was derived through layer-dependent PL spectroscopy as shown in Figure 11d [115]. The value of interlayer stress transfer efficiency was in the range of 0.76–0.86, higher than the value of graphene but lower than that of h-BN. The Raman peak shifts of few-layer BP were observed by Li *et al.* [132] for BP nanosheets sandwiched between PMMA and SU8 and subjected to uniaxial strain. The Raman shift rate of the B_{2g} mode was −11 cm^{-1}/% strain whereas the strain transfer coefficient was not confirmed.

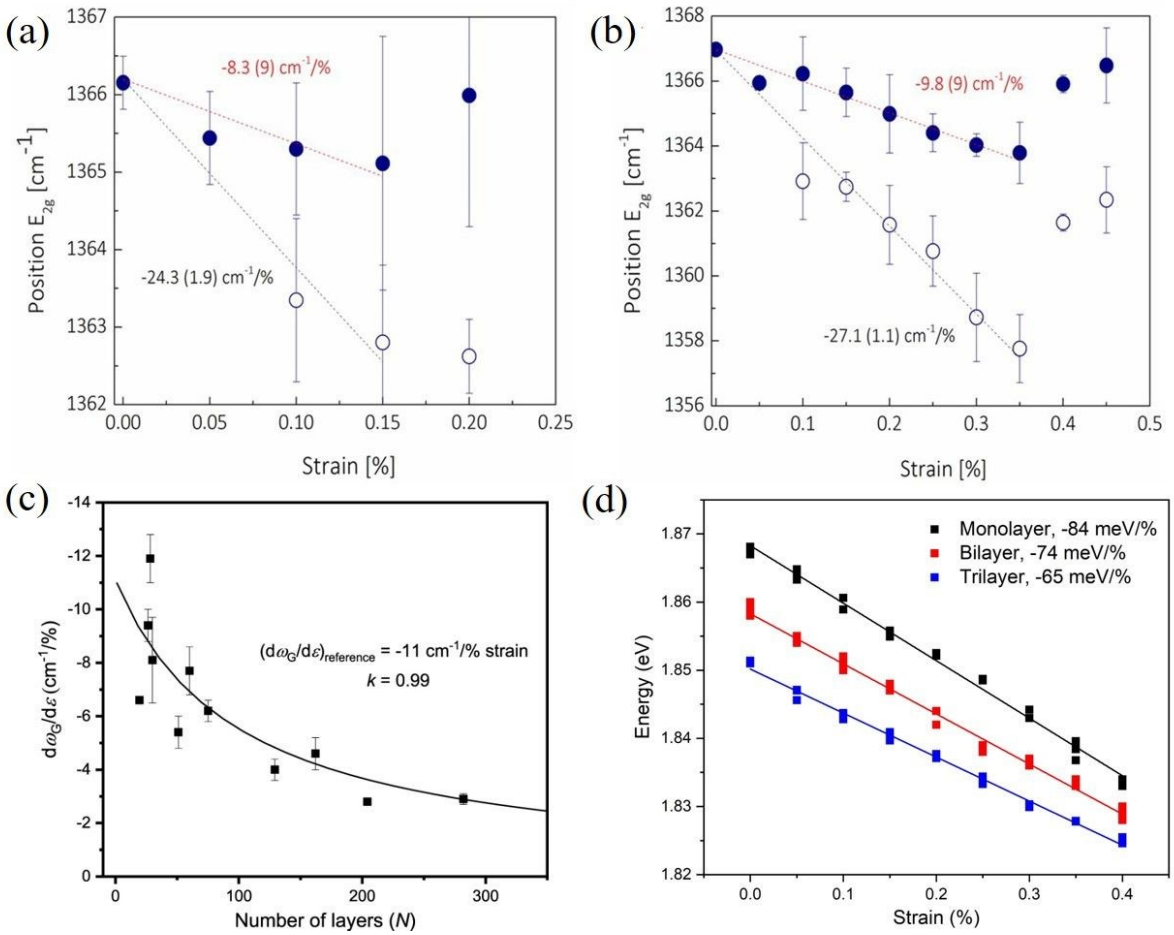

Figure 11. Raman G peak shifts of (a) bilayer and (b) four-layer h-BN under uniaxial tension.

View Article Online
DOI: 10.1039/D4NR01356E

Reproduced with permission from [100]. Copyright 2018 American Physical Society. (c) Raman G band shift rate of h-BN as a function of layer number. Reproduced with permission from [131]. Copyright 2021 IOP Publishing Ltd. (d) Evolution of the PL A peak of monolayer, bilayer and trilayer MoS_2 with strain. Reproduced with permission from [115]. Copyright 2023 Elsevier.

The parameters governing interfacial and interlayer stress transfer mechanisms of 2D materials within a polymer matrix are summarized in Table 2. Firstly, the interfacial shear strength values for different 2D materials in combination with different polymers (SU8, PMMA and PET) generally fall within the same order of magnitude. This is not surprising since interfacial stress transfer takes place primarily through van der Waals interactions and the effect of polymer or nanosheet chemical structure appears to be minimal. Secondly, chemical functionalization and wrinkled structures are effective ways to improve the interfacial shear strength at the expense of degrading the intrinsic mechanical properties of 2D materials. A balance should therefore be achieved between an increased shear strength and the degraded mechanical properties. Thirdly, the interlayer stress transfer efficiency plays a vital role in reinforcing polymer nanocomposites with 2D nanofillers in view of the fact that monolayer materials are not likely to be used commercially to reinforce bulk nanocomposites.

Table 2. Parameters related to interfacial stress transfer from polymers to 2D materials. (f-graphene: functionalized graphene; w-graphene, wrinkled graphene.)

2D materials	Layers	Polymer	Applied strain (%)	Interfacial shear strength (MPa)	Critical length (μm)	Interlayer transfer efficiency	Ref.
Graphene	1	SU8/PMMA	0.4–0.6	0.3–2.3	3	–	[19]
Graphene	1	PET	1.2–7.0	0.46–0.69	–	–	[20]
Graphene	2	SU8/PMMA	0.4	0.15	–	0.6–0.8	[128]
Graphene	1	SU8/PMMA	1.6	0.2–0.5	10	–	[133]
	2	SU8/PMMA	1.5	0.2–0.5	15–22	–	
	3	SU8/PMMA	1.6	0.2–0.5	22–30	–	
Graphene ribbon	1	PMMA	1.0	0.3	0.5–1	–	[117]

View Article Online
DOI: 10.1039/D4NR01356E

w-Graphene	3	SU8/PMMA	0.8	0.75	≥20	–	122
f-Graphene	1	PMMA	0.6	1.7	5.4	–	125
WS_2	1	SU8/PMMA	0.35–0.55	1.1–1.5	4	–	107
$Ti_3C_2T_x$	1	PMMA	0.4	3–4	–	–	108
h-BN	50	PMMA	0.1–0.3	3.8–9.4	6	0.99	131
MoS_2	1	PMMA	0.7	0.26–0.28	9	–	115
	2	PMMA	0.9	0.24–0.29	14	0.86	

3.4. Stacking, scrolling and folding in model nanocomposites

Compared to the top-down methods for the preparation of 2D nanosheets, one major advantage of the bottom-up CVD synthesis method is that the process is highly controllable. The continuous stacking of CVD grown nanosheets onto highly-ordered layered structures provides opportunities to model and study experimentally the mechanical properties of nanocomposites containing numerous nanosheets. Further processing of the stacked nanocomposites, such as cutting, scrolling and folding, can modify their mechanical performance [134-137]. Stacked CVD graphene-based laminates and scrolled fibres were firstly studied by Vlassiouk *et al.* [134] and then by Liu *et al.* [135]. Vlassiouk *et al.* [134] fabricated $(graphene/PMMA)_{16}$ (subscript represents layer number) laminates and subsequently scrolled the laminates into fibres. The addition of 0.13 vol% of graphene increased the PMMA modulus by a factor of three, but the strength increased by only a quarter. This corresponds to an effective modulus and strength of 1.2 ± 0.5 TPa and 11 ± 6.7 GPa according to the rule of mixtures, indicating effective stiffness reinforcement but poorer strength reinforcement. The enhancement is due to polymer orientation at the interface instead of efficienct load transfer between graphene and PMMA. The effective strength of graphene in the fibres was calculated to be 19 ± 9 GPa, (a reduced value due to defects in the fibres from and fracture of the nanosheets during scolling). This indicates that the theoretical and experimental values of the strength of graphene of about 130 GPa cannot be easily realised in practical applications such as nanocomposites. Liu *et al.* [135] fabricated very similar

View Article Online
DOI: 10.1039/D4NR01356E

(graphene/polycarbonate (PC))$_8$ up to (graphene/PC)$_{320}$ laminates and fibre structures as shown in Figure 12, with the graphene volume fractions ranging from 0.003 to 0.185%. The effective modulus of graphene was estimated to be in the order of 360 GPa and 500 GPa for the laminates and fibres, respectively. The atomic thinness of monolayer CVD graphene and its extremely large aspect ratio maximize the reinforcement. These highly interesting studies demonstrate sophisticated methods to prepare nanocomposites with uniformly-distributed nanosheets to take advantage of the unique properties of monolayer 2D nanosheets and approach the theoretical modulus values. It is possible that such nanocomposite assemblies might in the future be used for structural and functional applications but it should be noted that at present, the stacking process is time-consuming which makes it difficult to produce and use such assemblies used in bulk, practical applications. The development of the R2R process mentioned in Section 2.1.2 or an automated CVD transfer process may be promising routes to upscale this family of model nanocomposites. In a recent study, a scalable manufacturing approach, the float-stacking strategy, was proposed to fabricate graphene/PMMA laminates [138]. The graphene/PMMA membrane was initially floated on a water-air interface after etching the copper foil. Then, the membrane was stacked layer-by-layer by a roller, followed by a hot-rolling mill process to fabricate the laminate. Using this method, monolayer graphene was well-aligned in the polymer matrix and the effective Young's modulus of graphene was calculated to be 1.09 TPa. According to the authors, the heat-treatment eliminated wrinkles and voids on the surface and interlayer and increased the conformal contact of graphene and PMMA; this maximized the reinforcing efficiency of graphene. It should be noted though that the specific work has received considerable criticism from Ruoff and coworkers [139] who argued that the reported enhancement in the Young's modulus and strength of the graphene-reinforced laminated was mainly result of the heat treatment rather than the actual presence of graphene. In the same work, it was mentioned that the hot rolling process introduces a considerable amount of cracks and defects in graphene, which should reduce its reinforcing efficiency.

View Article Online
DOI: 10.1039/D4NR01356E

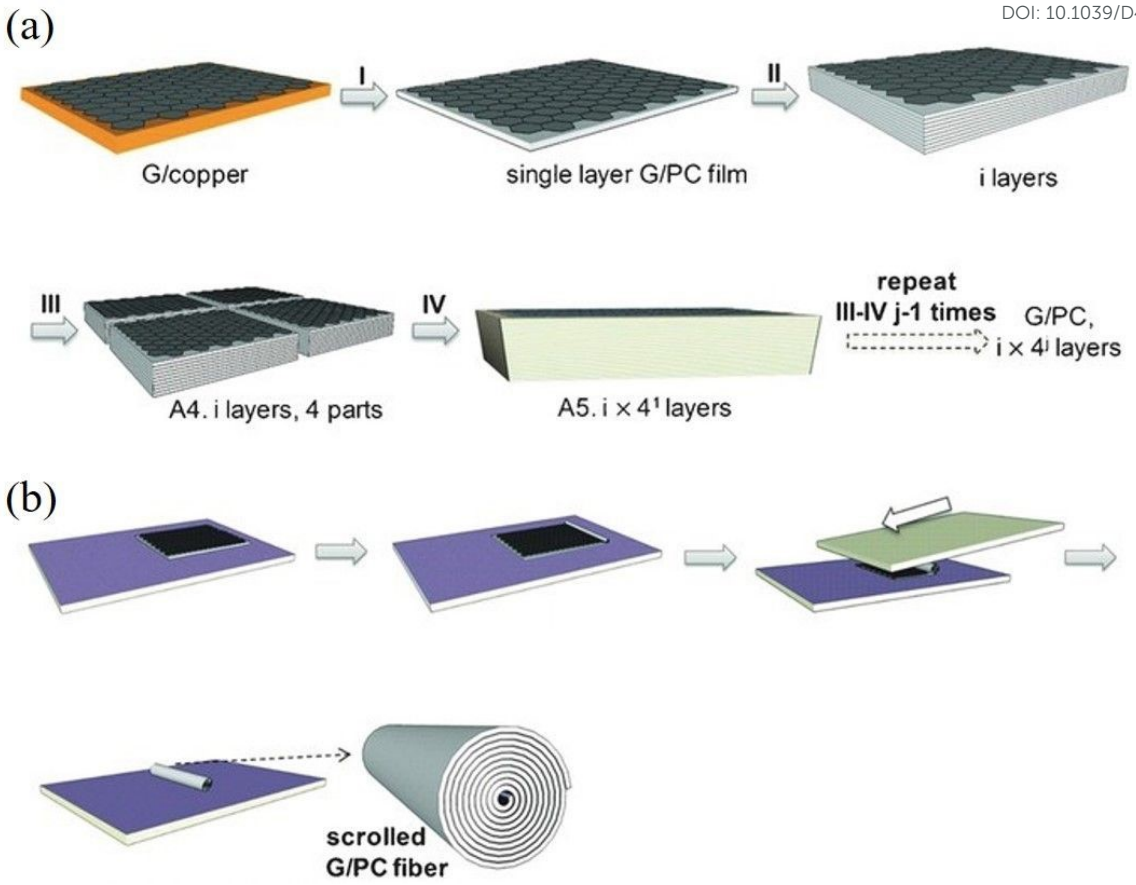

Figure 12. (a) Stacking and cutting of layered graphene/PC composites. (b) Scrolling of layered graphene/PC composites. Reproduced with permission from [135]. Copyright 2016 AAAS.

4. Bulk nanocomposites

4.1. Preparation

Even though the intrinsic mechanical properties of 2D materials are excellent both in their monolayer and few-layer forms, it is challenging to achieve their full potential in the mechanical reinforcement of polymer nanocomposites. The mechanical performance of the final nanocomposites depends strongly on the dispersion and orientation of the 2D materials in the matrix, and a homogeneous distribution of the fillers can improve the mechanical behaviour significantly. A number of approaches have been proposed to prepare high-performance nanocomposites, including physical mixing, *in situ* polymerization, layer-by-layer (LBL) assembly, evaporation, filtration and freeze casting.

View Article Online
DOI: 10.1039/D4NR01356E

4.1.1 Solution casting

The solution casting of 2D materials with polymers is a simple and versatile process and is used widely for the preparation of 2D polymer composites. Solution casting starts with the dispersion of 2D nanosheets and the polymer in separate solutions and the two are then blended. The solvent is finally removed by evaporation but the complete removal of solvents is required as the presence of solvents can lead to degradation of the ultimate properties of the nanocomposites. Solution casting has been reported for graphene [140], $TMDC_S$ [141] and MXenes [142]. A typical example is the work of Eksik *et al.* [143] who prepared MoS_2/epoxy nanocomposites containing 0.2 wt% MoS_2 using solution casting as shown in Figure 13. The bulk MoS_2 was exfoliated to monolayer and few-layer flakes via sonication in 1-vinyl-2 pyrrolidone. The epoxy was then added to the solvent and after a series of mixing steps the epoxy-MoS_2 nanocomposite was produced. It was found that low nanofiller loading fractions can improve the mechanical properties of the epoxy composites significantly. The fracture energy increased from 230 J m^{-2} for the epoxy matrix to 600 J m^{-2} and the fracture toughness increased from ~1 MPa $m^{1/2}$ to ~ 1.6 MPa $m^{1/2}$. Despite its simplicity, solution casting has a number of drawbacks. The use of toxic solvents can pose environmental hazards. Achieving a homogeneous dispersion of high-content fillers (e.g., over 10 wt%) in the matrix through simple mixing is difficult. Additionally, controlling the orientation of the fillers within the matrix presents a significant challenge. Finally, for thicker nanocomposites, sedimentation of the fillers is also an issue that also needs to be considered.

View Article Online
DOI: 10.1039/D4NR01356E

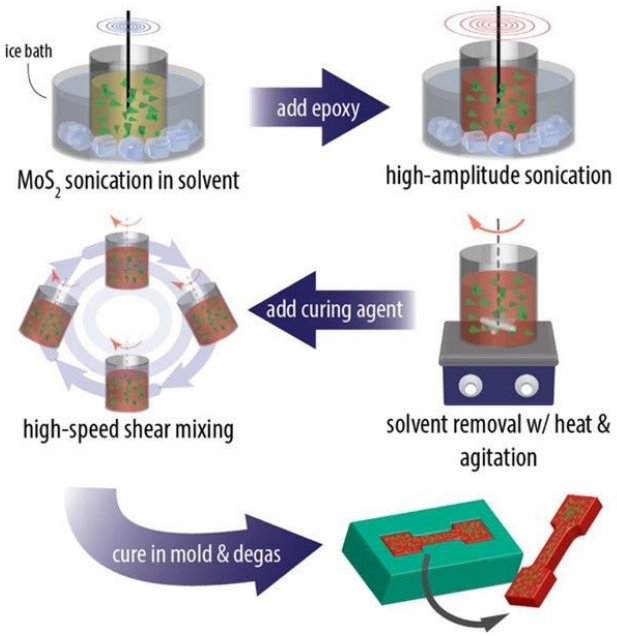

Figure 13. Solution casting method for the preparation of MoS_2/epoxy composites. Reproduced with permission from [143]. Copyright 2014 American Chemical Society.

Mechanical mixing, utilising high shear forces to disperse 2D materials in the matrix, is an alternative method to prepare polymer nanocomposites [144, 145]. Compared to solution casting, this method can avoid the use of toxic solvents and is more suitable for large-scale production. One example of a mechanical mixing process is the three-roll milling technique, in which shear forces generated by rollers can disperse 2D materials such as graphene [144, 145], hybrid MoS_2/h-BN [146] and MXene nanoplatelets [147] in the matrix. The drawbacks of mechanical mixing include difficulties in dispersing high filler contents homogeneously as a result of viscosity increase and a possible reduction in filler lateral size due to high shear forces.

4.1.2 Melt mixing

Melt mixing is another popular method that is commonly preferred by industry for the dispersion of nanofillers within thermoplastics [148-153]. The fillers are introduced into the polymers when the polymers are in a molten state, and then shear forces are exerted via rolls or screws to blend the

View Article Online
DOI: 10.1039/D4NR01256E

compounds. Sheng *et al.* [149] produced Ti_3C_2 MXene/thermoplastic-polyurethane (TPU) nanocomposites by melt mixing as shown in Figure 14a. Multilayer Ti_3C_2 MXene nanosheets were prepared by the selective etching-assisted liquid exfoliation method. A polyethylene glycol (PEG) aqueous solution was then added to the Ti_3C_2 MXene suspension and then mixed with molten TPU and PEG so that TPU/Ti_3C_2 nanocomposites were formed. The tensile strength of the composites was improved over that of the matrix by 47.1% to 20.6 MPa with 0.5 wt% Ti_3C_2. Problems associated with melt mixing include the high viscosity of some polymers or polymer/filler blends, which hinders the dispersion of fillers [154]. High mechanical forces are required in this case to improve the efficiency of the dispersion, but this can lead to wrinkling or crumpling of the fillers and sometimes fragmentation of the fillers into smaller sizes, all of which reduces their reinforcing capabilities [152]. The use of elevated temperatures during the melt mixing process can lead to disruption or decomposition of any functional groups in fillers.

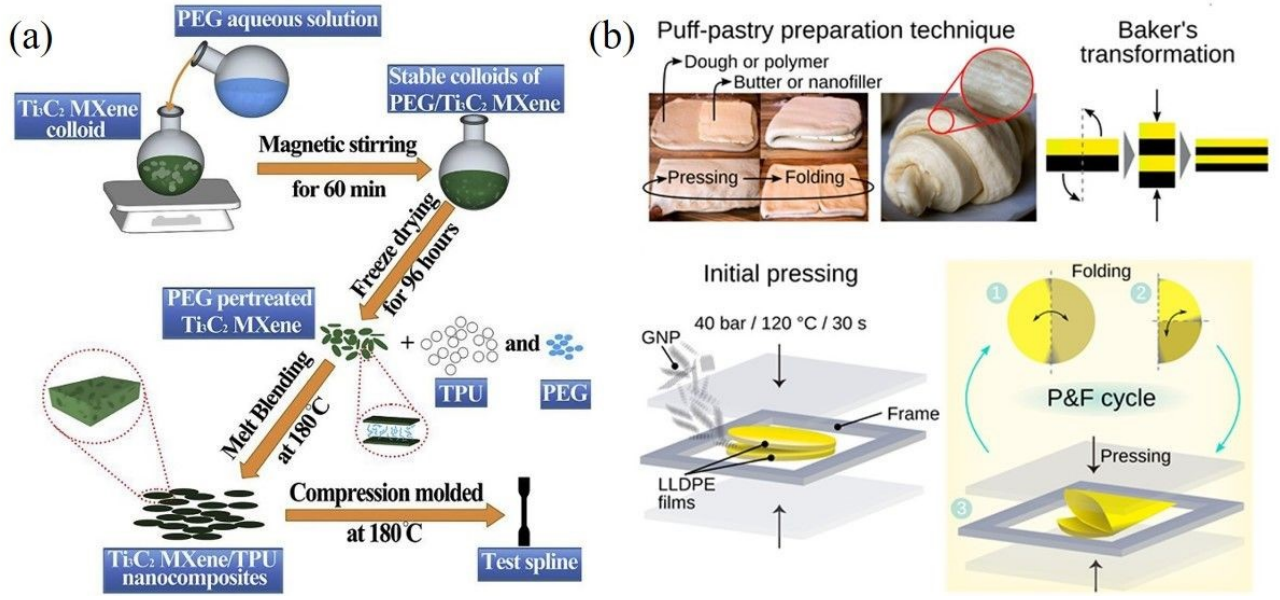

Figure 14. (a) Melt mixing method for the preparation of MXene/TPU composites. Reproduced with permission from [149]. Copyright 2019 Elsevier. (b) Puff-pastry preparation inspired pressing-and-folding method and illustration of this method for the fabrication of a GNP/LLDPE composite film. Reproduced with permission from [155]. Copyright 2018 America Chemical Society.

View Article Online
DOI: 10.1039/D4NR01356E

A press-and-folding (P&F) method inspired by puff-pastry preparation has been used to fabricate 2D nanosheets/polymer nanocomposites. Santagiuliana *et al.* [155] prepared graphene nanoplatelets (GNPs)/linear-low density polyethylene (LLDPE) composite films using the P&F method illustrated in Figure 14b. The GNPs were added to the middle of two LLDPE films to form a sandwich structure. The sandwich structure was then hot-pressed and folded twice and the P&F process was repeated several times to prepare the composites. The mechanical properties of the composites improved significantly with the increase of the number of P&F cycles due to a more homogeneous distribution of the GNPs in the composites. For example, the elastic modulus reinforcement was more than doubled after 500 P&F cycles compared to the unmodified nanocomposite. This study shows that P&F is an effective method to improve the dispersion of nanofillers in nanocomposites and therefore optimise their mechanical properties.

4.1.3 In situ polymerization

In situ polymerization, involving 2D nanosheets being mixed with monomers in solution or in emulsion state, is an effective approach for preparing well-dispersed polymer nanocomposites [156, 157]. The monomers can enter the interlayer space between 2D nanosheets before polymerization, leading to intercalation polymerization. This method displays some advantages over mixing with a polymer as it allows the homogeneous distribution of fillers in polymers and simultaneous exfoliation of the multilayer nanosheets. Tong *et al.* [157] prepared $Ti_3C_2T_x$ MXene/polypyrrole (PPy) composites via *in situ* polymerization as shown in Figure 15. The $Ti_3C_2T_x$ nanosheets were exfoliated by etching-assisted exfoliation in an HF solution and the pyrrole monomers were added to the solution. $Ti_3C_2T_x$/PPy composites with the nanosheeets well-aligned in the in-plane direction were obtained via centrifuging and drying in vacuum. A characteristic of *in situ* polymerization is the significant viscosity increase at relatively low filler contents (compared to solution blending or melt mixing), leading to processing difficulties (less efficient mixing) and agglomeration. As a result, a relatively low content of filler

View Article Online
DOI: 10.1039/D4NR01356E

(commonly less than 3 wt%) can be incorporated via *in situ* polymerization and the fact that it is a time-consuming process, hinders the full potential of its application for nanocomposites [158].

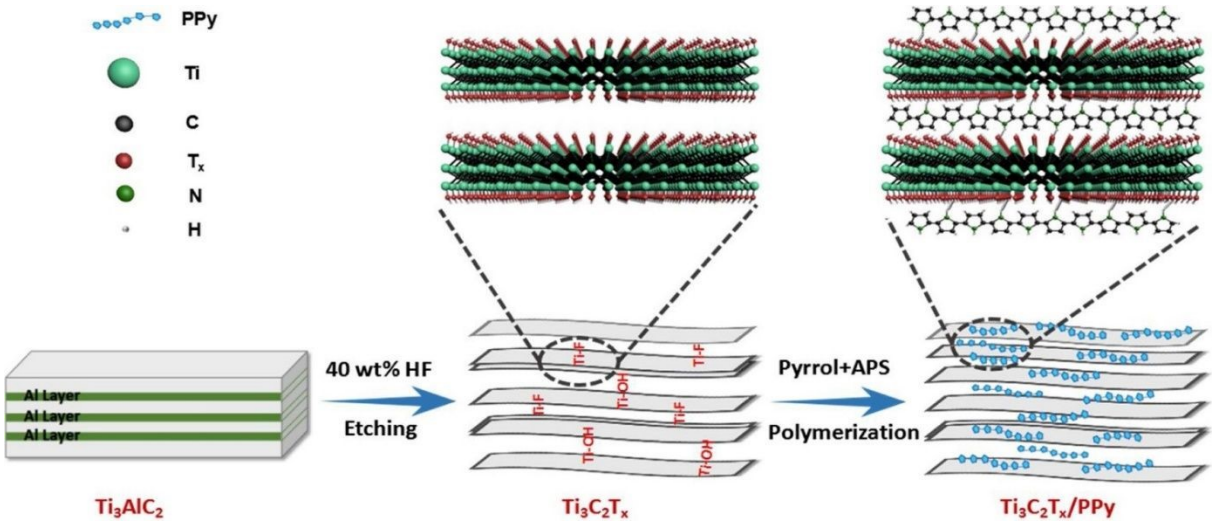

Figure 15. In situ polymerization for the preparation of $Ti_3C_2T_x$/polypyrrole (PPy) composites. Reproduced with permission from [157]. Copyright 2018 Elsevier.

4.1.4 Layer-by-layer assembly

Layer-by-layer (LBL) assembly was initially used for the fabrication of polymer films driven by ionic interactions [159]. Different forms of driving force have been utilised to assist the assembly process such as electrostatic attraction, hydrogen bonding, coordination bonding and charge transfer interactions [160]. The method has been applied widely to prepare nanocomposites based on graphene and graphene oxide nanosheets [161, 162]. Xiang *et al.* [163] prepared multilayer graphene/polymer composites through LBL assembly as shown in Figure 16. The substrate was coated with polyethylenimine (PEI) primer layer and the graphene was stabilized with polyvinylpyrrolidone (PVP). The substrate was dipped firstly into poly(acrylic acid) (PAA), and hydrogen bonds formed when the substrate was dipped into the PVP-stabilized graphene solution. Multilayer graphene/PAA/PVP composites were produced by repeating this process. The elastic modulus of the polymer was improved from 1.41 to 4.81 GPa with the addition of 3.9 vol% of graphene nanoplatelets. Overall, the LBL technique is a versatile approach to assemble 2D nanosheets with a controlled

View Article Online
DOI: 10.1039/D4NR01356E

distribution and alignment; however, novel strategies need to be explored for the improvement of the assembly efficiency. Overall, LBL assembly constitutes a scalable and highly-promising process to incorporate 2D materials into polymer nanocomposites.

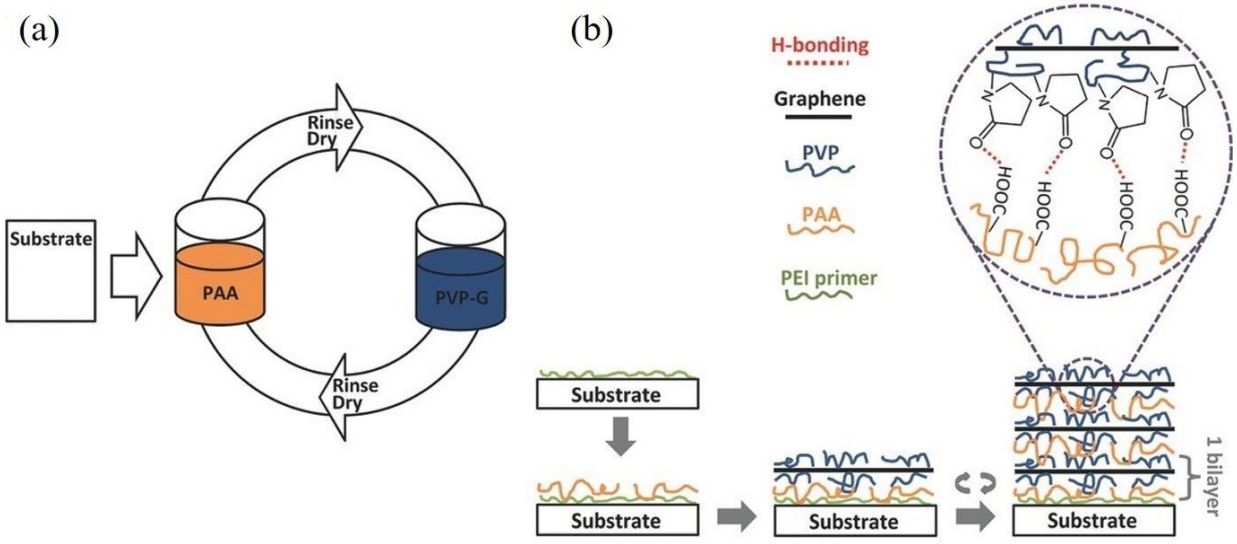

Figure 16. Layer-by-layer assembly for the preparation of graphene/polymer composites. Reproduced with permission from [163]. Copyright 2016 Wiley-VCH Verlag GmbH & Co. KGaA.

4.1.5 Other methods

Other strategies have been proposed to disperse 2D nanosheets into polymers such as vacuum filtration and freeze casting [164]. These methods show huge potential for the assembly of 2D nanosheets in polymers, as they can usually achieve an excellent distribution of nanofillers. Putz *et al*. [165] prepared GO/PVA and GO/PMMA nanocomposites with over 50 wt% filler using vacuum filtration as illustrated in Figure 17. The fabricated films displayed a high degree of order and good mechanical properties. For example, the Young's modulus of GO/PVA films reached 36.4 GPa with 50 wt% filler due to the formation to hydrogen bonds. Disadvantages include the long times needed to prepare the nanocomposites via evaporation, while the precise control of layered and ordered structures is still difficult.

View Article Online
DOI: 10.1039/D4NR01356E

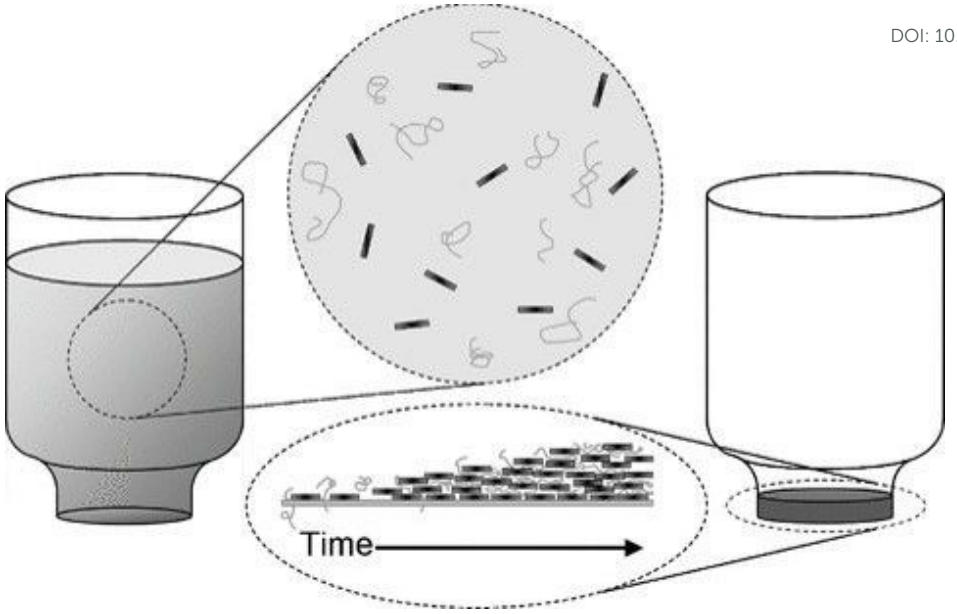

Figure 17. Vacuum filtration for the preparation of GO/PVA and GO/PMMA nancomposites. Reproduced with permission from [165]. Copyright 2010 Wiley-VCH Verlag GmbH & Co. KGaA.

4.2. Mechanisms of Reinforcement

4.2.1 Analytical model

In Section 3.1, we showed that shear-lag theory and interface slippage can be used to describe stress transfer from a matrix to 2D nanosheets. This means that continuum mechanics can be used to analyse the model nanocomposites with fillers of atomic thickness [23]. Opposing views have been expressed in the literature suggesting that polymer nanocomposites should be treated as molecular composites considering the nucleation and molecular confinement originating from nanoparticles, especially using carbon nanotubes [166]. Indeed the micromechanical theories are not able to account for the contribution of such factors. The application of classical composite micromechanics seems, however, to be able to model the mechanical properties of numerous polymer nanocomposites based on a wide range of 2D materials, particularly at low filler loadings [16].

When subjected to uniform homogeneous strain, the rule of mixtures can be used to describe the Young's modulus of the bulk nanocomposites E_c as

View Article Online
DOI: 10.1039/D4NR02356E

$$E_c = E_f V_f + E_m V_m \quad (10)$$

where E_f, E_m are the Young's modulus of the filler and the matrix, V_f, V_m are the volume fraction of the filler and the matrix ($V_f + V_m = 1$), respectively. Because of its simplicity, this equation has been applied widely to describe reinforcement from 2D nanosheets. Significant effects such as the orientation, the aspect ratio and the agglomeration of the fillers, on the mechanical reinforcement are ignored though and that is why a number of modifications for rule of mixtures have been proposed.

By taking the orientation and the aspect ratio of the fillers into consideration, Eq. (10) can be modified as

$$E_c = \eta_o \eta_l E_{eff} V_f + E_m V_m \quad (11)$$

in which E_{eff} is the effective modulus of the fillers, η_o is the Krenchel orientation factor and η_l is the length factor both of which take values from 0 to 1. The Krenchel orientation factor depends on the flake alignment while the length factor is dependent on the aspect ratio of fillers and interfacial shear strength. For aligned fillers ($\eta_o = 1$), when a strong interface ($\eta_l \to 1$) between the filler and the matrix is formed, the effective elastic modulus will be high and good mechanical reinforcement can be achieved. Otherwise, small aspect ratios, random distribution and low interfacial shear strength will have a negative effect upon the performance of nanosheets in polymer composites. The value of the orientation factor for two-dimensional nanofillers with a random distribution is 8/15 [167, 168], while in the case of one-dimensional nanofillers (i.e. carbon nanotubes) the random orientation factor equals 1/5 [23]. Given that the majority of polymer nanocomposite manufacturing methods lead to randomly oriented fillers, this is an vivid indication why the random orientation for 2D nanofillers produces better-performing nanocomposites compared to random 1D nanofillers. The spatial orientation of 2D nanofillers in a polymer matrix can be quantified through the use of polarized Raman spectroscopy [167, 169]. As illustrated in Figure 18a, GO nanoplatelets are randomly distributed in epoxy and PMMA with η_o= 8/15, while GO nanoplatelets tend align in the plane of PVA film.

View Article Online
DOI: 10.1039/D4NR01356E

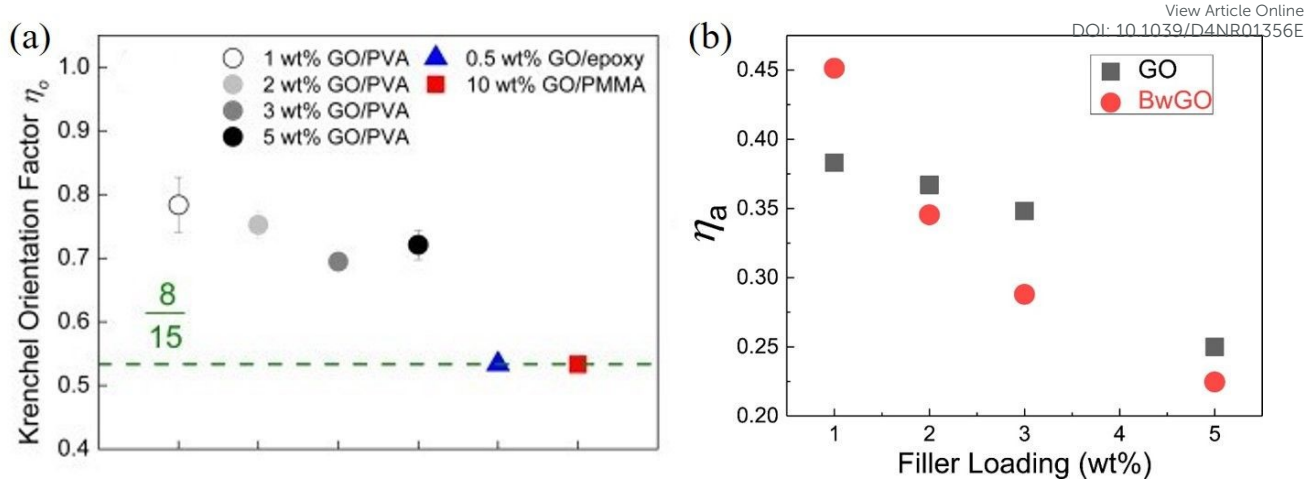

Figure 18. (a) Krenchel orientation factors of GO/PVA, GO/epoxy and GO/PMMA nanocomposites. Reproduced with permission from [167]. Copyright 2016 Elsevier. (b) Variations of agglomeration factor with GO and BwGO (the functional groups of GO were partially removed by base wash) filler loadings. Reproduced with permission from [170]. Copyright 2018 Elsevier.

Meanwhile, agglomeration is very important in controlling mechanical properties. The rule of mixtures will fail to describe the behaviour of polymer nanocomposites if agglomeration is extensive, especially at high loadings. Li *et al.* [170] proposed to include an agglomeration factor η_a to the modified rule of mixtures to account for the effect of agglomeration on the modulus of composites such that:

$$E_c = \eta_o \eta_l E_{eff} \eta_a V_f + E_m V_m \quad (12)$$

If no agglomeration takes place during the preparation of composites ($\eta_a = 1$), the effective volume fraction of fillers will be high and good stress transfer can be obtained. Otherwise, an increase in agglomeration will degrade the reinforcement significantly. The agglomeration factor generally decreases with an increase in filler loading. Even though BwGO (the functional groups of GO were partially removed by base washing) shows a better dispersion at low loadings, its agglomeration factor declines faster compared to that for GO due to the reduction of the number of functional groups (Figure 18b). Following the shear-lag theory in Section 3.1, the length factor can be determined by

View Article Online
DOI: 10.1039/D4NR01356E

$$\eta_{\mathrm{l}} = 1 - \frac{\tanh\left(ns/2\right)}{ns/2}. \tag{13}$$

Recently, Young *et al.* [171] evaluated the effect of aspect ratio, order of alignment and Young's modulus of nanosheets on the efficiency of reinforcement, based on the shear-lag theory and the rule of mixtures. Substituting Eq. (13) into the expression for the modulus of fillers

$$E_{\mathrm{f}} = E_{\mathrm{eff}}\eta_{\mathrm{o}}\left[1 - \frac{\tanh\left(ns/2\right)}{ns/2}\right] \tag{14}$$

For flexible matrices (small *ns*), Eq. (14) is expressed as

$$E_{\mathrm{f}} \approx E_{\mathrm{eff}}\eta_{\mathrm{o}}\frac{\left(ns/2\right)^2}{3} \tag{15}$$

Then, inserting the equations $n = \sqrt{\frac{2G_{\mathrm{m}}}{E_{\mathrm{f}}}\frac{t}{T}}$ and $G_{\mathrm{m}} = \frac{E_{\mathrm{m}}}{2(1+\nu)}$ into Eq. (15), the Young's modulus of the filler becomes

$$E_{\mathrm{f}} \approx \eta_{\mathrm{o}}\frac{s^2}{12}\frac{t}{T}\frac{E_{\mathrm{m}}}{(1+\nu)} \tag{16}$$

Quite interestingly, this equation predicts that the modulus of fillers is proportional to the modulus of the matrix and indepedent of the modulus of the nanofiller. Substituting Eq. (16) into Eq. (10), the following equation can be obtained

$$E_{\mathrm{c}} \approx E_{\mathrm{m}}\left[1 - V_{\mathrm{f}} + \frac{s^2}{12}\frac{\eta_{\mathrm{o}}}{(1+\nu)}V_{\mathrm{f}}^2\right] \tag{17}$$

This expression reveals that the modulus of the final composites is independent of the modulus of the nanofillers, while it is dependent on the modulus of the matrix, the aspect ratio and the volume fraction of the fillers. As can be seen from Figure 19a, Eq. (17) works well for a number of polymer matrices with varying degrees of stiffness. Additionally, the modulus of the nanofillers derived from Raman 2D modes show good agreement with the theoretical predictions after using the equation $E_{\mathrm{R}} = E_{\mathrm{gr}}\left[\left(\partial\omega_{\mathrm{2D}}/\partial\varepsilon\right)/\left(\partial\omega_{\mathrm{2D}}/\partial\varepsilon\right)_{\mathrm{ref}}\right]$ as stated in Section 3.3.

View Article Online
DOI: 10.1039/D4NR01356E

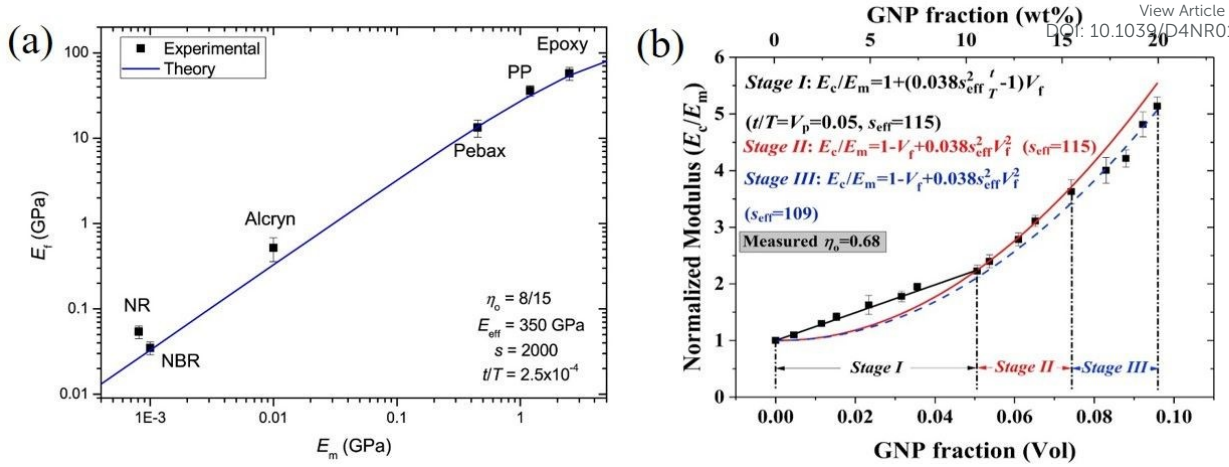

Figure 19 (a) Variation of the modulus of graphene nanoplatelets (GNPs) with the modulus of the matrices (dots: experiment data; blue line: theory predictions from Eq. (16) and Eq. (19)). Reproduced with permission from [171]. Copyright 2018 Elsevier. (b) Three stages for the reinforcement of GNPs on elastomers. Reproduced with permission from [153]. Copyright 2019 Elsevier.

More recently, the effects of the volume fraction of the fillers on the mechanical reinforcement of elastomers were studied further and the concept of a mechanical percolation threshold volume fraction V_p was proposed, above which the stiffness increases significantly from the interaction of neighbouring fillers, while below V_p, the rate of increase is much smaller as a result of the contributions of individual fillers [153]. For volume fractions of filler (V_f) below V_p, the shear-lag interfacial parameter t/T can be approximated to be equal to V_p and the following equation is obtained by substituting Eq. (16) into Eq. (10)

$$E_c/E_m = 1 + \left(\frac{s_{eff}^2}{12}\frac{\eta_o}{(1+\nu)}\frac{t}{T} - 1\right)V_f \quad (18)$$

where s_{eff} is the effective aspect ratio of the filler. For filler volume fractions above V_p, the following equation can be obtained after substituting t/T with V_f

$$E_c/E_m = 1 - V_f + \frac{s_{eff}^2}{12}\frac{\eta_o}{(1+\nu)}V_f^2 \quad (19)$$

According to Eqs. (18) and (19), the reinforcement process can be divided into three stages with

increasing filler loading as shown in Figure 19b. For the first stage of reinforcement ($V_f < V_p$), there is no interaction between individual fillers and the interfacial parameter t/T is proportional to V_p. For the second stage ($V_f > V_p$), the interaction between fillers starts to increase and the reinforcement is quadratically related to the volume fraction, as described by Eq. (19). For the final stage of reinforcement, at the highest levels of filler content, agglomeration occurs and the reinforcing efficiency is reduced, as can be seen from the reduction of the effective aspect ratio. The good agreement between the theory and experimental data in Figure 18c validates the accuracy of Eqs. (18) and (19) in the prediction of mechanical reinforcement of elastomers.

4.2.2 Semi-empirical model

There are some limitations and uncertainties about the use of rule of mixtures for the estimation of Young's modulus of polymer nanocomposites. As a result, other models have been proposed to evaluate the modulus enhancement of composites such as the semi-empirical one of Halpin-Tsai [172]. For well-aligned nanofillers, this model provides the Young's modulus in the longitudinal direction $E_{\parallel}$ and the transverse direction $E_{\perp}$as

$$E_{\parallel} = \left(\frac{1 + \xi\eta_{\parallel}V_f}{1 - \eta_{\parallel}V_f}\right)E_m \tag{20}$$

$$E_{\perp} = \left(\frac{1 + 2\eta_{\perp}V_f}{1 - \eta_{\perp}V_f}\right)E_m \tag{21}$$

Where

$$\eta_{\parallel} = \frac{E_f/E_m - 1}{E_f/E_m + \xi} \tag{22}$$

$$\eta_{\perp} = \frac{E_f/E_m - 1}{E_f/E_m + 2} \tag{23}$$

in which ξ is the geometry fitting parameter, which is related to the aspect ratio of fillers (ξ=2s for the well-aligned case). When $\xi \to 0$, the reinforcement is not effective enough; when $\xi \to \infty$, the reinforcement is highly effective and Eqs. (20) and (21) transforms to the rule of mixtures. For the 2D

173 View Article Online
DOI: 10.1039/D4NR01356E

random distribution of the fillers, the Young's modulus of the composites is given as

$$E_c = \left[\frac{3}{8}\left(\frac{1+\xi\eta_{\parallel}V_f}{1-\eta_{\parallel}V_f}\right)+\frac{5}{8}\left(\frac{1+2\eta_{\perp}V_f}{1-\eta_{\perp}V_f}\right)\right]E_m \quad (24)$$

in which $\xi = (2/3)s$.

Generally, low filler loadings can reinforce polymer nanocomposites effectively, while the use of fillers at high contents decreases the reinforcing efficiency due to the tendency of the fillers to agglomerate. With the current progress in preparation strategies that are presented in literature, polymer nanocomposites with well-dispersed fillers at high contents have been successfully fabricated and very large improvements of the mechanical properties of a wide range of polymers have been reported.

4.3. Mechanical Properties

As can be understood from the previous sections, a number of factors can affect the reinforcing efficiency and the final mechanical performance of the bulk nanocomposites; these include the aspect ratio, the orientation, the agglomeration and volume fraction of the fillers, the interfacial interaction between the fillers and the matrices and the modulus of the matrix. Considering the large family of 2D materials, it is highly desirable to investigate the levels of mechanical reinforcement that can be obtained from different 2D nanosheets. A large number of polymer nanocomposites based on different 2D nanofillers are reviewed in the following section.

4.3.1 Graphene nanocomposites

Graphene is quite arguably the most widely studied two-dimensional material due to its exceptional intrinsic properties and, as a result, numerous investigations have used graphene-related materials for the development of multifunctional polymer nanocomposites. A number of graphene-related materials have been used to reinforce polymers, ranging from graphene nanoplatelets of various thicknesses, lateral sizes and types of functionalization, to graphene oxide (GO) and reduced GO

(rGO). These GO-based materials display poorer mechanical properties but their functional groups can provide enhanced interfacial adhesion [174]. Wang *et al.* [175] studied the mechanical reinforcement of a PVA matrix by GO and rGO. The composites were prepared by the solution casting method and the stress-strain curves of GO/PVA and rGO/PVA composites are shown in Figure 20a and 20b. In terms of GO, 4 wt% GO provided the optimal reinforcement and the tensile strength of the matrix was improved to 55 MPa. On one hand, the presence of the functional groups of GO can lead to enhanced interfacial interactions between GO and the matrix. On the other hand, the ultimate performance of GO-based composites is not as good compared to ones based on rGO because the intrinsic mechanical properties of GO are relatively poor. In terms of rGO, it can be seen that 0.5 wt% provided optimum reinforcement where the tensile strength of PVA is more than tripled from 23 to 72 MPa. A further increase in loading degraded the tensile strength of the composites. This means that a low-content of rGO is more efficient in mechanical reinforcement due to its excellent mechanical properties, and the degradation in mechanical properties with a higher rGO content is possibly the result of agglomeration.

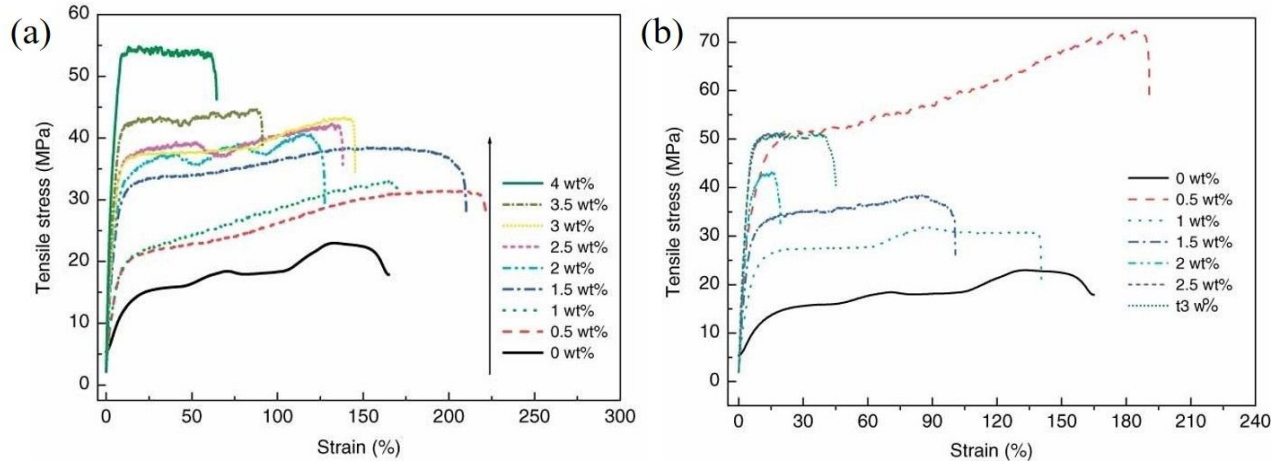

Figure 20. Variations of stress-strain curves with filler loading for (a) GO/PVA and (b) rGO/PVA nanocomposites, respectively. Reproduced with permission from [175]. Copyright 2011 Wiley-VCH Verlag GmbH & Co. KGaA.

In addition to the effects of functionalization and agglomeration, it is interesting to examine the relationship between the effective mechanical reinforcement and modulus of the matrix. Papageorgiou

View Article Online
DOI: 10.1039/D4NR01356E

et al. [16] extracted the Young's modulus E_f (using Eq 10) of GNP, GO and rGO from a large number of polymer nanocomposites with various values of matrix stiffness, as shown in Figure 21. As an update, the data released after 2017 (derived from Table 3) are added to Figure 21. Even though considerable scatter exists in the data as a result of numerous factors including orientation, agglomeration, aspect ratio, filler functionalization etc., the Young's modulus of graphene-based nanocomposites was found to increase linearly with the increase of the modulus of the matrix. For soft matrices, the low shear modulus of the polymers leads to ineffective stress transfer between the filler and the matrix and subsequently poor mechanical reinforcement. This is why the exceptional properties of 2D materials cannot be fully realised in elastomers even though the apparent percentage (%) increases over those of the elastomer matrix are usually impressive even at low filler contents. This conclusion is important for the study of the mechanical reinforcement from graphene in polymer nanocomposites and provides guidance for the application of other 2D nanosheets in polymer nanocomposites.

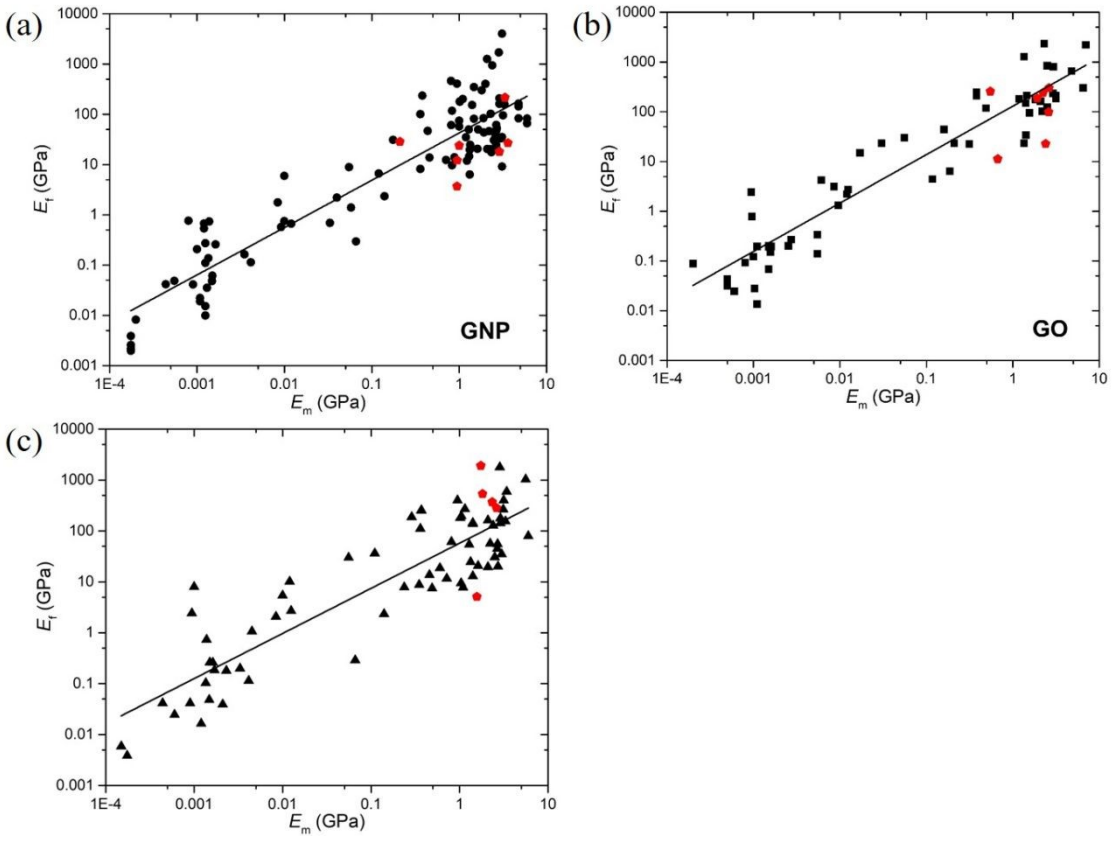

Figure 21. Variations of the Young's modulus of (a) GNP, (b) GO and (c) rGO with the modulus of

View Article Online
DOI: 10.1039/D4NR01356E

matrices. The red dots correspond to new data published after 2017 and provide an update to the previous figure presented in [16]. Reproduced with permission from [16]. Copyright 2017 Elsevier.

Fracture toughness is another important mechanical property affected by the addition of nanofillers to composites [176, 177]. Tang *et al.* [178] investigated the effects of nanofiller dispersion on the fracture toughness of graphene/epoxy nanocomposites prepared by solution casting. Ball milling was used to generate high shear stress to prevent agglomeration and improve dispersion of reduced GO (rGO) nanosheets, while the samples not processed by ball milling were found to be poorly-dispersed. It should be kept in mind, however, that high-energy milling procedures over long time periods can lead to a significant reduction of the aspect ratio of the fillers and as a consequence to poorer effective mechanical properties. The fracture toughness of the poorly-dispersed and well-dispersed composites was found to be increased by about 24% and 52%, respectively, upon the addition of 0.2 wt% rGO, as shown in Figure 22a. This study shows once again the importance of the dispersion of fillers in the improvement of the fracture toughness of composites. To further promote the dispersion of fillers, carboxyl terminated butadiene acrylonitrile (CTBN) was used and the effects of CTBN on the mechanical and thermal properties of graphene/epoxy nanocomposites were studied [179]. The addition of CTBN can supress the debonding between the flakes and the epoxy. Compared to the neat epoxy, the fracture toughness of the CTBN/epoxy composites was improved by ~70% with 10 wt% CTBN. The optimal loading of graphene was achieved at 3 wt% loading for which the fracture toughness of the epoxy was more than doubled. The mechanisms whereby the GNPs can affect crack propagation are illustrated in Figure 22c: (1) crack deflection and layer breakage; (2) separation between GNP layers; and (3) crack penetration and layer breakage.

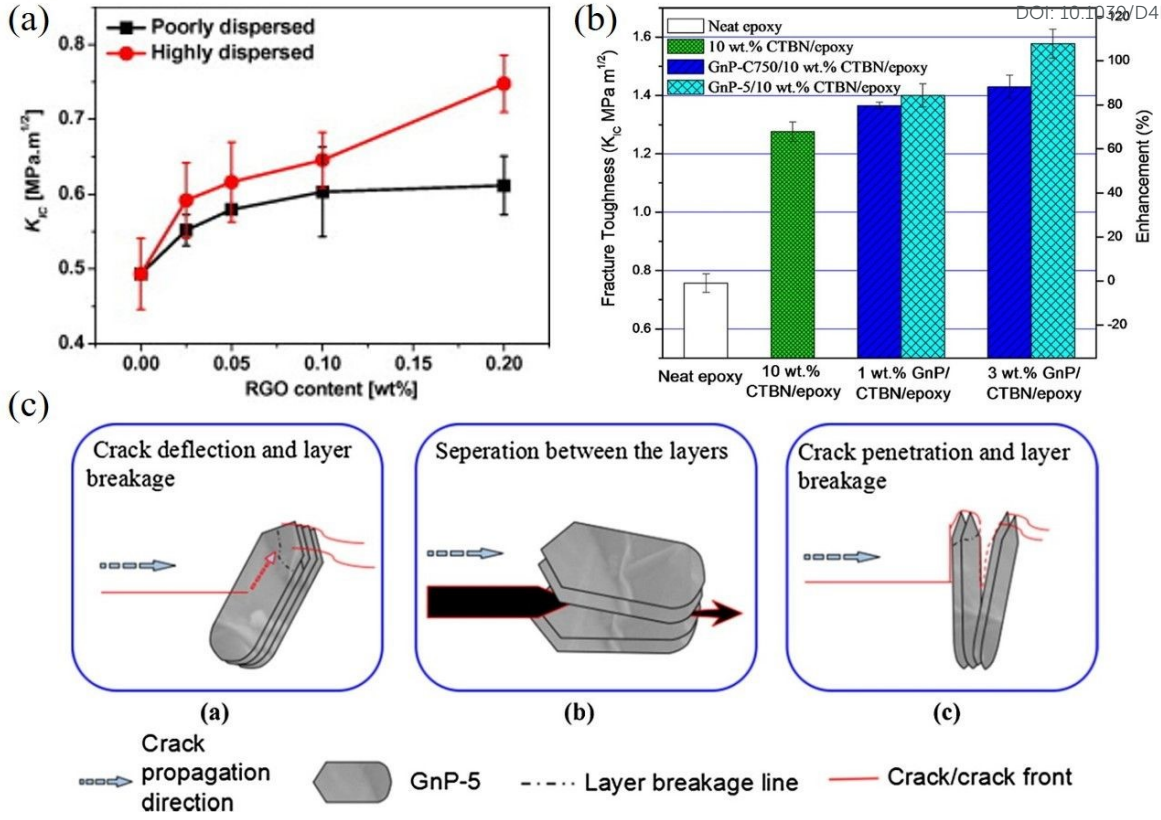

Figure 22. (a) Variations of K_{IC} of rGO/epoxy nanocomposites with rGO loading. Reproduced with permission from [178]. Copyright 2013 Elsevier. (b) Effects of CTBN and GNP on the fracture toughness of epoxy composites. (c) Crack propagation in GnP-5 flakes. Reproduced with permission from [179]. Copyright 2016 Elsevier.

Another intriguing concept for the utilisation of the geometry of the 2D fillers is the fabrication of nacre-type composites [164]. Nacre has high strength and toughness, which has been attributed to its hierarchical structure and abundant interfacial interactions. This has motivated researchers to construct nanocomposites with nacre-like microstructures to improve their mechanical properties [164]. Compared to graphene, GO is more advantageous in the improvement of tensile strength as the surface functional groups enable the formation of strong interlayer bonds. Li *et al*. [180] prepared GO/PVA composites with nacre-like structures using solution casting, while rGO/PVA composites were prepared by the reduction of the original GO/PVA composites (Figure 23a). The stress-strain curves of the composites fabricated are shown in Figure 23b. The Young's modulus and tensile strength were found to be 11.4

View Article Online
DOI: 10.1039/D4NR01356E

GPa and 118.0 MPa for GO/PVA nacre-composites, significantly higher than the values of 4.1 GPa and 67.1 MPa for the neat GO films. The tensile strength increased to 188.9 MPa and the Young's modulus decreased slightly to 10.4 GPa for rGO/PVA composites. The improvements in mechanical properties are thought to be due to the formation of hydrogen bonds and the hierarchical structure between the GO (or rGO) and PVA. When the composites are subjected to tension, the weak vdW bonds will break first and with an increase in loading, and the hydrogen bonds will also break. More energy is required to fracture the composites with enhanced hydrogen and oxygen bonds and therefore tensile strength is improved. In summary, a hierarchical structure and strong interlayer bonds are two key factors that can be tuned to improve the mechanical properties of the nanocomposites. Different methods such as vacuum filtration and freezing have been used to prepare polymer nanocomposites based on graphene derivatives [165, 181].

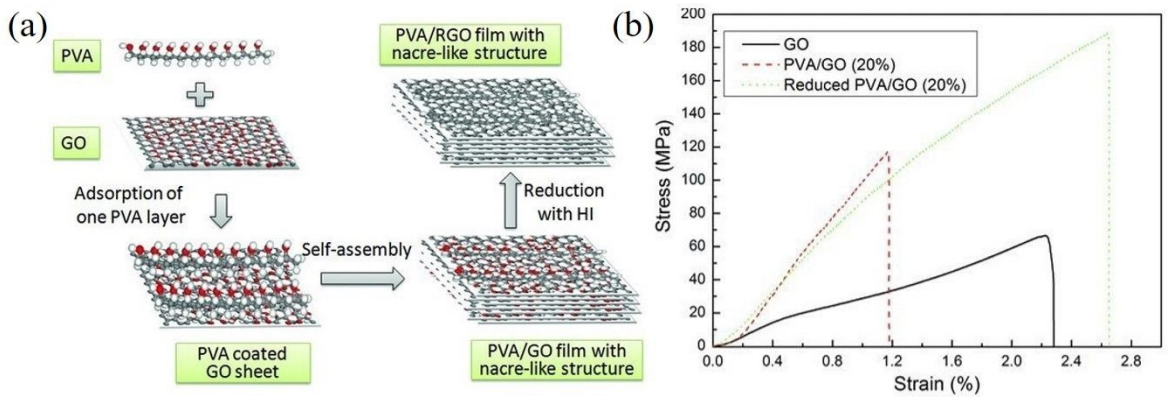

Figure 23. (a) Preparation of GO/PVA and rGO/PVA composites with nacre-like structures. (b) Stress-strain curves of GO films, GO/PVA and rGO/PVA composites. Reproduced with permission from [180]. Copyright 2012 Wiley-VCH Verlag GmbH & Co. KGaA.

Table 3. Mechanical properties of polymer nanocomposites based on graphene. (*when more than one optimum filler fractions are mentioned, they correspond to the optimum filler fractions for improvement of modulus, strength and toughness, sequentially.)

Filler	Matrix	Processing Method	Matrix modulus (GPa)	Optimum filler fraction*	Increase (%)			Ref.
					Young's modulus	Tensile strength	Fracture toughness	

View Article Online
DOI: 10.1039/D4NR01356E

f-rGO	PMMA	In situ polymerization	3.12	1 wt%	42	15		182
f-GNP	PMMA	Solution casting	1	2 wt%	24	20	–	183
GO	PMMA	Vacuum filtration	0.67	75 wt%	1019	1116	–	165
rGO	Epoxy	Solution casting	2.91	0.2 wt%	6	7	51	178
GNP	Epoxy	Solution casting	3.75	3 wt%	–	–	109	179
GO	Epoxy	Solution casting	3	0.1, 0.5, 1 wt%	12	13	63	184
GO	Epoxy	Solution casting	1.92	0.75, 0.5 wt%	40	3	–	185
GO	Epoxy	Solution casting	2.62	0.5 wt%	31	52	–	186
rGO	Epoxy	Solution casting	2.62	0.5 wt%	28	31	–	186
rGO	Epoxy	Solution casting	1.82	0.3 wt%	47	47	–	187
rGO	Epoxy	Freeze casting	–	1 wt%	–	–	314	188
f-GNP	Epoxy	Solution casting	3.35	2 wt%	71	23	124	189
GNP	Epoxy	Solution casting	2.89	78 wt%	411	–	–	190
GNP	Epoxy	Solution casting	–	5 wt%	–	–	51	191
GO	PVA	Vacuum filtration	2.6	50 wt%	1300	186	–	165
GO	PVA	Vacuum filtration	2.1	5, 3 wt%	190	69	–	192
f-rGO	PVA	Solution casting	2.34	1 wt%	82	48	–	193
GO	PVA	Solution casting	0.12	3 vol%	990	166	–	194
rGO	PVA	Solution casting	1.74	0.1, 0.3 wt%	55	48	–	195
f-GO	PLA	Solution casting	1.9	0.2, 0.2, 0.6 wt%	19.2	58	384	196
f-GO	PS	Solution casting	1.45	0.9 wt%	57.2	69.5	–	197
GO	PS/ PMMA	In situ polymerization	2.24	0.25 wt%	14	11	–	198
GNP	PVC	Solution casting	0.8	2 wt%	58	130	–	199
rGO	PP	Melt mixing	1.02	0.42 vol%	74	75	–	200
f-GNP	PI	In situ polymerization	2.3	3 wt%	610	84	–	201
f-GO	PI	In situ polymerization	0.55	1 wt%	257.2	58	–	202
GO	PVDF	Solution casting	1.4	2 wt%	192	92	–	203
f-rGO	PVDF	Solution casting	1.0	5, 1 wt%	585	317	–	
GO	CS	Solution casting	1.32	1 wt%	64	122	–	204
GO	CS	Vacuum filtration	2.4	95 wt%	842	391	–	205
GNP	HDPE	Melt mixing	0.95	10 wt%	56	23	–	206
GNP	PEEK	Melt mixing	3.61	10 wt%	44	–	–	207
GNP	PA6	Melt mixing	1.2	20 wt%	412	54	–	208
GO	Silk	Layer by layer	9.5	23.5 vol%	1426	200	–	209

View Article Online
DOI: 10.1039/D4NR01356E

GNP	Cellulose	Vacuum filtration	0.945	50 wt%	137	33		210
f-GNP	ABS	Solution casting	0.21	1 wt%	60	18	107.1	211
rGO	ANF	Vacuum filtration	1.57	50 wt%	125	-19	–	212

[a] PLA, polylactic acid; PS, polystyrene; PVC, poly(vinyl chloride); PP, polypropylene; PI, polyimide; PVDF, polyvinylidene fluoride; CS, chitosan; HDPE, high-density polyethylene; PEEK, poly(ether ether ketone); PA6, polyamide 6; GF, graphene fluoride; ABS, acrylonitrile butadiene styrene, ANF, aramid nanofiber.

4.3.2 Boron nitride nanocomposites

As mentioned earlier, h-BN nanosheets possess excellent mechanical properties as their Young's modulus is similar to that of graphene. Furthermore, it has been confirmed by AFM indentation [17] and Raman spectroscopy [100] that the increase of layer number to about ten does not degrade their mechanical properties due to strong interlayer interactions; h-BN nanosheets therefore show excellent potential in the mechanical reinforcement of polymer nanocomposites. However, the small lateral size of liquid exfoliated h-BN flakes and their poor interfacial shear strength with polymers hampers the realisation of their full potential. Zhi *et al.* [213] exfoliated boron nitride nanosheets (BNNSs) in *N*,*N*-dimethylformamide (DMF) and prepared BNNS/PMMA nanocomposites by solution blending. It was found that the Young's modulus of the PMMA was improved from 1.74 to 2.13 GPa with the addition of 0.3 wt% BN nanosheets and the tensile strength was improved by 11%.

In order to enhance the mechanical performance of BN-based composites, different surface functionalization strategies, including physical and chemical functionalization [214], have been applied in a number of studies. For example, Kim *et al.* [215] functionalized the BNNSs non-covalently with 1-pyrenebutyric acid (PBA) molecules and prepared BNNS/epoxy nanocomposites by solution blending, as seen from Figure 24a to 24d. Compared to the neat epoxy, the addition of 0.3 wt% BNNSs led to an improvement of Young's modulus and tensile strength from 2.7 to 3.3 GPa and from 46.7 to 71.9 MPa, corresponding to increases of 21% and 54%. Significantly, the fracture toughness of the composites was improved from 0.7 to 1.5 MJ m^{-3}. These significant improvements in the mechanical properties were attributed to the increased surface area and good stress transfer, as π-π interactions were established between the PBA molecules and BN nanosheets. In another study, the effects of non-

View Article Online
DOI: 10.1039/D4NR01256E

covalent functionalization on the storage modulus of h-BN /bisphenol E cyanate ester (BECy) composites were investigated, as shown in Figure 24e [216]. At 10 vol% loading, dopamine-treated h-BN composites show better reinforcement than pristine h-BN; while at 15 vol% loading, the performance of dopamine-treated h-BN samples was worse compared to pristine h-BN. The storage modulus of the composites at 25 ℃ was improved significantly from 2.0 to 7.1 GPa with 15 vol% of untreated h-BN. This shows the importance of controlling the degree of functionalization and the loading of fillers, as discussed in Section 3.2. There is a balance between the effect of improved dispersion as well as the better interfacial interactions upon the ultimate mechanical properties of nanocomposites, due to functionalization of the nanofillers.

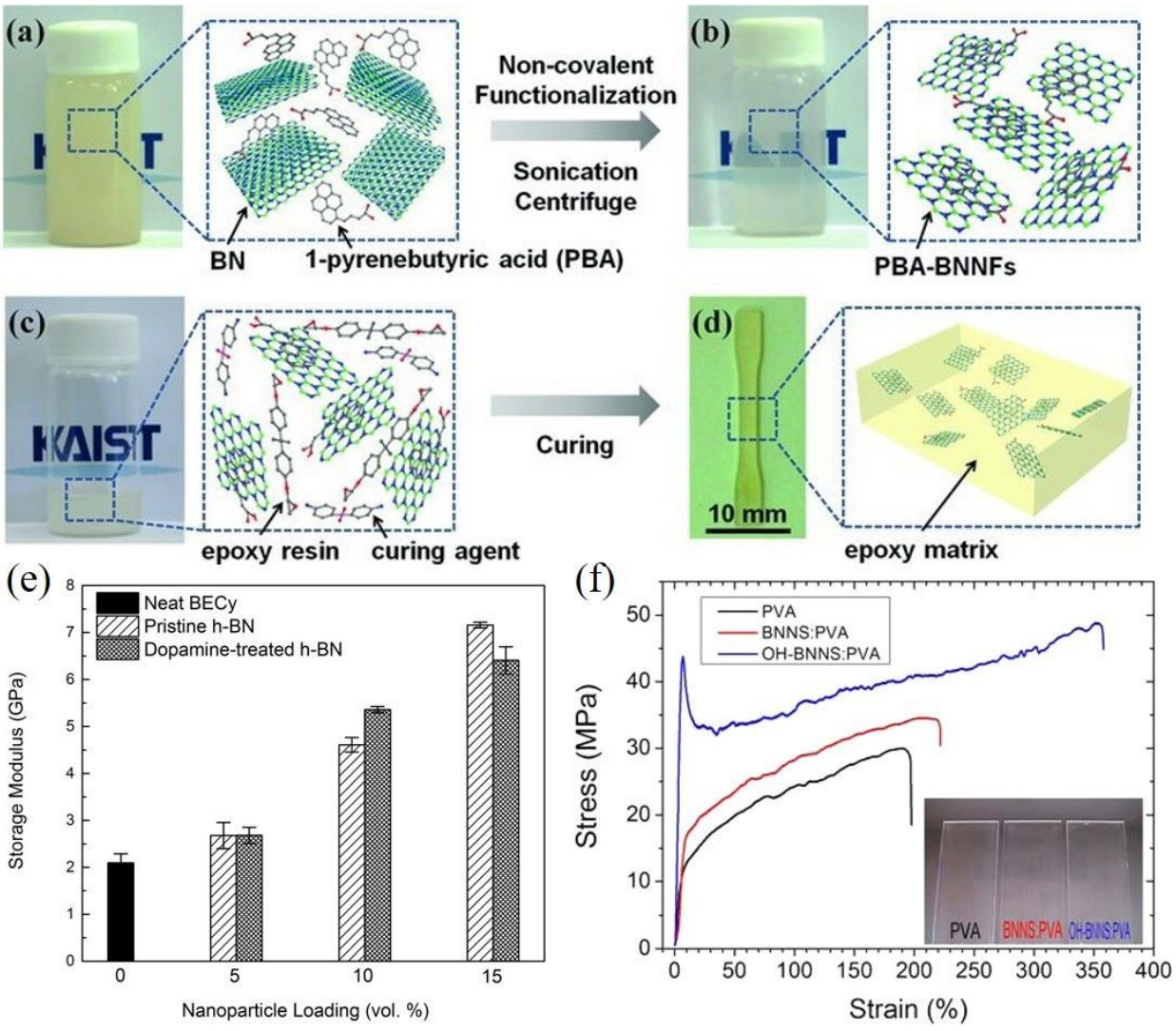

Figure 24. (a-d) Non-covalent functionalization of h-BN and solution blending for the preparation of

View Article Online
DOI: 10.1039/D4NR01556E

h-BN/epoxy composites. Reproduced with permission from [215]. Copyright 2013 Wiley-VCH Verlag GmbH & Co. KGaA. (e) Variations of storage modulus at 25 ℃ of BNNS/BECy composites with nanoparticle loading. Reproduced with permission from [216]. Copyright 2015 American Chemical Society. (f) Stress-strain curves of BNNS/PVA composites. Reproduced with permission from [217]. Copyright 2012 American Chemical Society.

Covalent functionalization has been used to improve the mechanical performance of h-BN-based nanocomposites. Sainsbury *et al.* [217] covalently functionalized BNNSs and prepared hydroxyl-functionalized BNNS (OH-BNNS) and isocyanate-functionalized BNNS (i-BNNS). The stress-strain curves of such BNNS/PVA composites are shown in Figure 24f. Compared to the neat PVA, the Young's modulus and tensile strength of the OH-BNNS/PVA composites were respectively increased from 0.4 to 1.1 GPa and from 30 to 49 MPa with only 0.1 wt% filler. Several factors contributed to the improvements in the mechanical properties of the nanocomposites. The lateral size of the exfoliated BN nanosheets was as large as 2 to 3 μm which is beneficial for stress transfer, while the covalent functionalization and the uniform alignment promoted the performance of the h-BN nanosheets in matrices. Recently, Liu *et al.* [218] covalently functionalized BNNSs using (3-aminopropyl) triethoxysilane (APTES) and fabricated APTES-BNNS/epoxy nanocomposites by solution blending. Compared with the neat epoxy, the storage modulus of the nanocomposites filled with 10 wt% of APTES-BNNSs at 35 °C was increased from 1.5 GPa to 4.3 GPa.

Apart from surface functionalization, different preparation and alignment approaches have been used to fabricate BNNS-based composites displaying homogeneous dispersion. Hu *et al.* [219] prepared h-BN/epoxy nanocomposites via hot pressing the mixture of BNNS and epoxy at 150 ℃ and under a pressure of 10 MPa. This fabrication strategy was found to improve the orientation of BN in an epoxy matrix significantly. For the neat matrix, the elastic modulus, tensile strength and fracture toughness were measured to be 0.6 GPa, 23.6 MPa, and 0.87 MJ m^{-3}. The maximum fracture toughness was

View Article Online
DOI: 10.1039/D4NR01356E

found to be 1.1 MJ m^{-3} at 10 wt% h-BN loading, showing an increase of 33%; while the maximum tensile strength was 39.3 MPa with 30 wt% of h-BN nanosheets. Finally, the Young's modulus increased by more than 600% to 4.63 GPa with 50 wt% of aligned h-BN in comparison to the value of 1.48 GPa obtained from 50 wt% randomly oriented h-BN, as shown in Figure 25a. As can be seen from the evaluation of individual mechanical properties as a function of filler loading, the tensile strength and fracture toughness are prone to be affected by the agglomeration of BNNSs and therefore reach their maximum values at lower loadings compared to Young's modulus. In another interesting study, a magnetic field was used to align BN nanosheets in epoxy matrix [220]. The effects of alignment on the Young's modulus of the epoxy composites with 20 wt% h-BN are shown in Figure 25b. Compared to the modulus of neat epoxy at 2.7 GPa, vertically-aligned composites (VmhBN-epoxy, z direction) show the highest elastic modulus at 4.55 GPa, while randomly-distributed (RmhBN-epoxy) and horizontally-aligned (VmhBN-epoxy, x-y direction) composites show similar modulus values (3.45 and 3.52 GPa). Overall, high degrees of orientation, induced by compressive or magnetic forces have been demonstrated to improve the mechanical properties of nanocomposites reinforced with BNNS effectively.

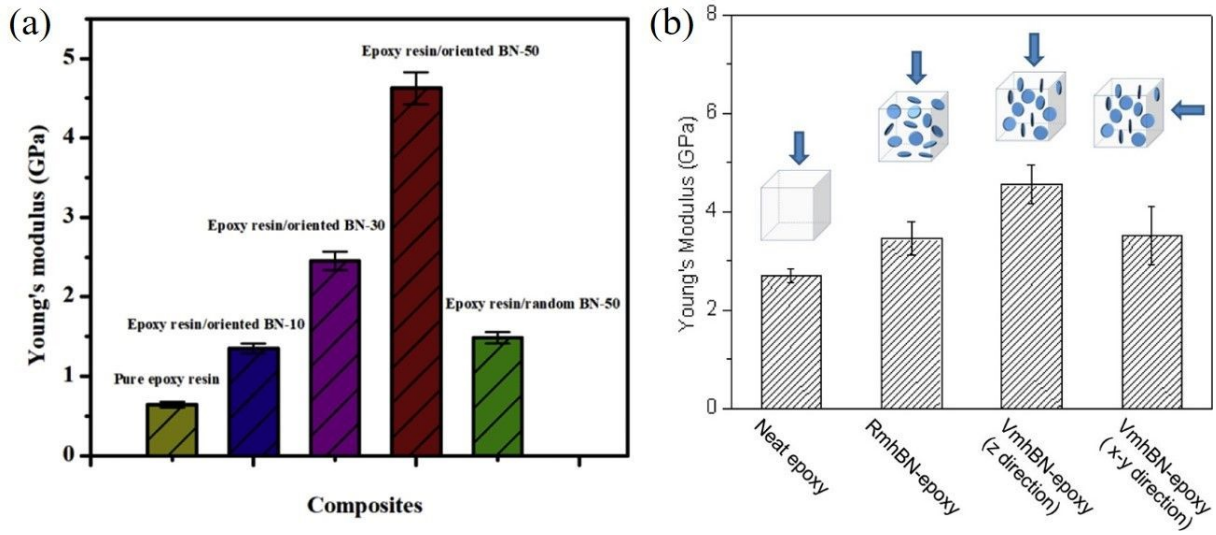

Figure 25. (a) Variation of the Young's modulus of the h-BN/epoxy nanocomposites with h-BN content. Reproduced with permission from [219]. Copyright 2018 Elsevier. (b) Variation of the Young's modulus of h-BN/epoxy nanocomposites with the orientation of h-BN. Reproduced with permission

from [220]. Copyright 2013 American Chemical Society.

View Article Online
DOI: 10.1039/D4NR01356E

Table 4. Mechanical properties of polymer nanocomposites based on boron nitride.

Filler	Matrix	Processing Method	Matrix modulus (GPa)	Optimum filler fraction*	Increase (%)			Ref.
					Young's modulus	Tensile strength	Fracture toughness	
BN	PMMA	Solution casting	1.74	0.3 wt%	22	11	–	213
BN	PMMA	Solution casting	2.2	3 wt%	132	–	–	221
f-BN	PMMA	Hot pressing	0.739	0.5 wt%	8.7	–	69.6	222
f-BN	Epoxy	Solution casting	2.749	0.3 wt%	21	54	107	223
BN	Epoxy	Hot pressing	0.64	50, 30, 10 wt%	623	66	30	219
BN	Epoxy	Solution casting	2.7	20 wt%	68.5	–	–	220
BN	Epoxy	Solution casting	–	2 wt%	–	–	121	224
BN	Epoxy	Freeze casting	–	2.08 vol%	–	–	600	224
f-BN	PVA	Solution casting	0.378	0.1 wt%	186	66	191	225
BN	PVA	Solution casting	2.5	0.12, 0.05 vol%	36	33	–	225
BN	PVA	Solution casting	1.52	0.5 wt%	39	27	–	226
BN	PVA	Vacuum filtration	0.053	27 vol%	1221	83	–	227
f-BN	PVA	Solution casting	0.18	0.2 wt%	73.6	109.3	–	228
f-BN	PVA	Vacuum filtration	0.4	60 wt%	1800	110	–	229
BN	PVC	Solution casting	2	0.12 vol%	37.5	60	–	230
f-BN	PS	Melt mixing	2.01	30 wt%	23	82	–	231
f-BN	PU	Solution casting	0.19	0.1 wt%	17	118	233	232
BN	PE	Solution casting	0.4	5 wt%	64.1	26	–	233
BN	UHMW PE	Solution casting	3.01	11 wt%	152	–	–	235
BN	PVDF	Electrospinning	0.002	1 wt%	200	900	2614	234
f-BN	PVDF	Electrospinning	0.87	30 wt%	24	151	–	236
BN	PDMS	Solution casting	–	28.6 wt%	–	75	36	236
f-BN	SBR	Mechanical mixing	0.002	90 phr	653	145	–	237
BN	PA66	Melt mixing	2.6	20 wt%	92	4	–	238
BN	PEN	Solution casting	2.637	5, 2 wt%	11	16	–	239
BN	ANF	Vacuum filtration	2.81	70 wt%	31.9	61.6	–	240

[a] PU, polyurethane; PE, polyethylene; UHMWPE, ultrahigh molecular weight polyethylene; SBR, styrene butadiene rubber; PA66, polyamide 66; PEN, polyarylene ether nitrile.

View Article Online
DOI: 10.1039/D4NR01356E

4.3.3 TMDC-based nanocomposites

TMDCs possess interesting mechanical properties and apart from their high values of elastic modulus, TMDCs show good compatibility with polymers. It has been found that stress can be transferred to few-layer TMDCs effectively so that they can be considered as mechanical-reinforcing agents in polymer nanocomposites. Riaz *et al*. [241] compared the role of MoS_2 nanosheets (MNSs) and MoS_2 quantum dots (MQDs) in the mechanical reinforcement of an epoxy resin. It was found that MQDs were more effective in reinforcing epoxy nanocomposites as shown in Figure 26a and 26b. With the addition of 0.2 wt% MQDs, K_{IC} and G_{IC} of epoxy were improved by 81% and 151%, higher than the counterpart of MNSs. Compared to the MNSs, the MQDs showed excellent dispersion and better interfacial interactions with the epoxy resin as illustrated in Figure 26c. As a consequence, the MQDs were able to fill the cavities in the matrix and improve the mechanical and interfacial properties.

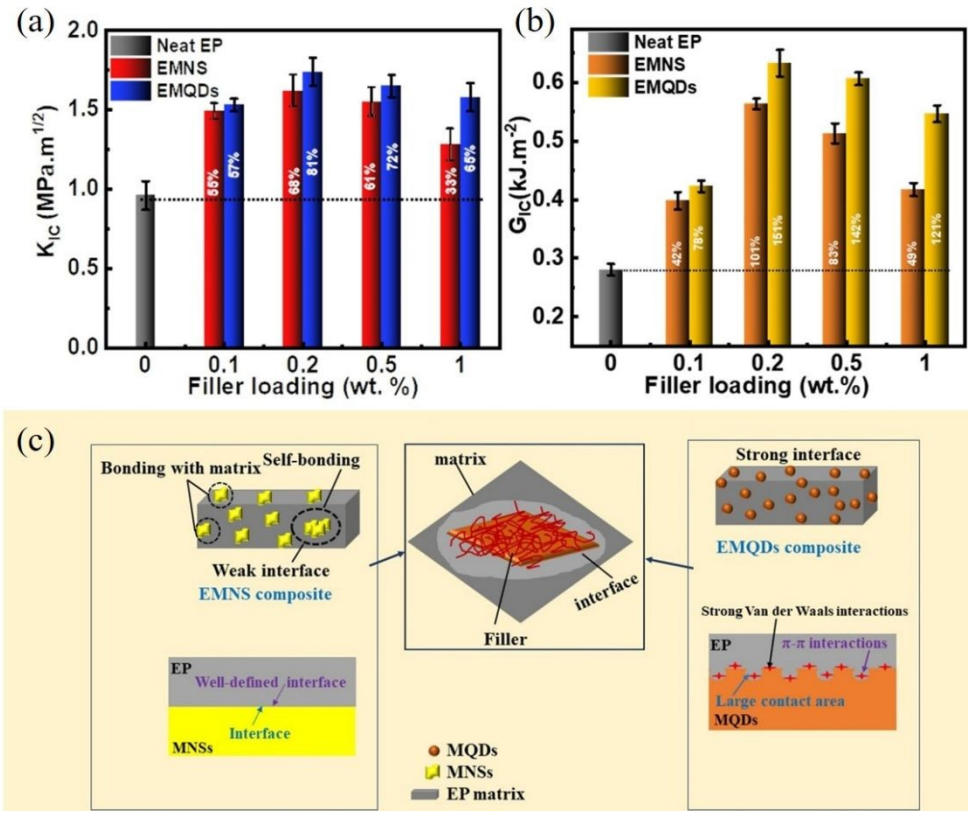

Figure 26. (a) K_{IC} and (b) G_{IC} of neat epoxy, epoxy/MNSs (EMNS) and epoxy/MQDs (EMQDs) nanocomposites. (c) Interfacial interactions of EMNS and EMQDs. Reproduced with permission from

[241]. Copyright 2021 Elsevier.

View Article Online
DOI: 10.1039/D4NR01356E

Poor interfacial strength between the matrix and the TMDCs restricts the reinforcing efficiency of the nanofiller. Non-covalent functionalization can therefore improve the interfacial interactions and hence the mechanical properties of the nanocomposites [242-244]. Feng *et al.* [242] prepared MoS_2/poly(ethylene oxide) (PEO) nanocomposites via solution blending. The exfoliation and non-covalent functionalization were conducted in a pluronic aqueous solution assisted by sonication. It was found that the addition of 0.9 wt% MoS_2 increased the Young's modulus of the neat PEO (0.84 GPa) by ~90%. The mechanical reinforcement in terms of the elastic modulus of the matrix showed good agreement with the Halpin−Tsai model in the case of the random distribution of 2D nanosheets. This improvement was attributed to the good interfacial interaction and gradient interfaces between the MoS_2 and PEO (due to non-covalent functionalization). The use of the surfactant during the exfoliation procedure improved the effective volume fraction of the MoS_2 nanosheets. Wang *et al*. [244] prepared lipoic acid-functionalized MoS_2/nylon-6 (PA6) composites via *in situ* polymerization. It was found that the elastic modulus and tensile strength of the pristine PA6 were enhanced by about 80% (to 2.45 GPa) and 78% (to 80.6 MPa), respectively, upon the addition of 1.0 wt% functionalized MoS_2. The weak van der Waals interfaces were modified by the chemical bonds, which led to an improvement in interfacial stress transfer. The *in situ* polymerization method is known to make the distribution of fillers more homogeneous [156, 157] in the case of MoS_2 nanosheets, although its use is generally limited by its restriction to low filler contents.

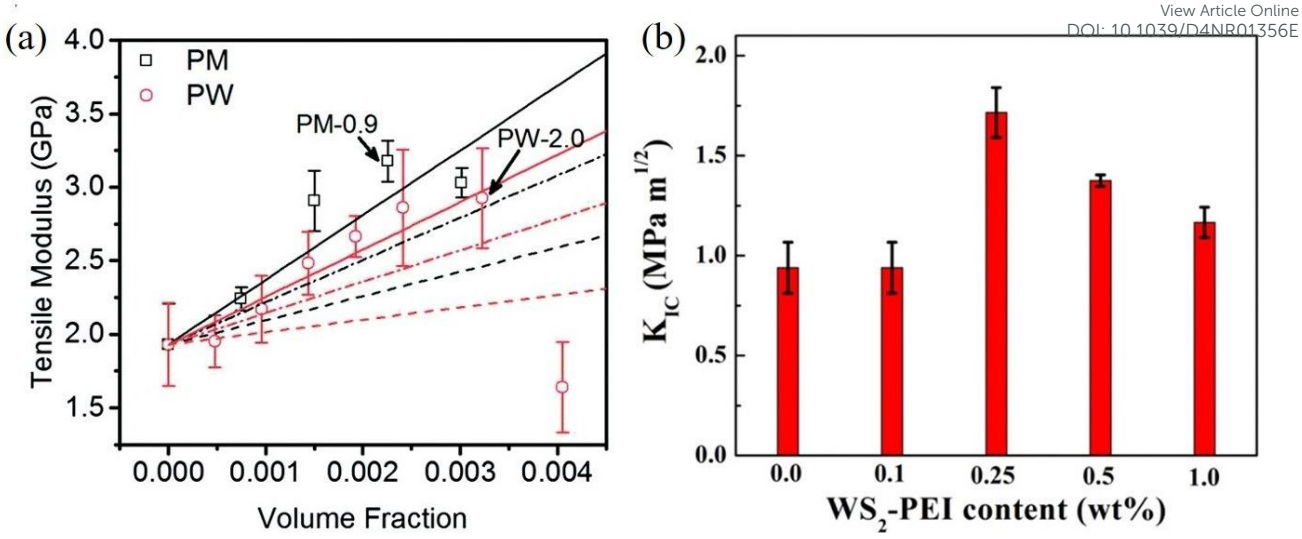

Figure 27. (a) Tensile modulus for the PVA composites based on MoS_2 (PM) and WS_2 (PW). Reproduced with permission from [245]. Copyright 2014 Royal Society of Chemistry. (b) Variation of facture toughness of WS_2/Epoxy composites with volume fraction. Reproduced with permission from [246]. Copyright 2017 American Chemical Society.

In addition to MoS_2, other TMDCs such as WS_2 [245, 246] and $MoSe_2$ [247] have also been used as reinforcing agents in polymer composites. For example, Kim *et al.* [245] compared the mechanical reinforcement of MoS_2 and WS_2 in a PVA matrix. The MoS_2 and WS_2 nanosheets were fabricated via intercalation-assisted liquid exfoliation (their lateral sizes were quite small, of the order of 50-200 nm), and the composites were prepared by solution blending. The variation of tensile modulus with volume fraction is shown in Figure 27a, where PM and PW represent the MoS_2- and WS_2-based PVA composites. Despite the small lateral size of the nanosheets it was found that the addition of 2.0 wt% WS_2 increases the elastic modulus of the composites by 52% from 1.93 GPa to 2.93 GPa, while the introduction of 0.9 wt% MoS_2 led to an increase of the modulus by 65% from 1.93 GPa to 3.18 GPa. This difference is due to the fact that the interactions between the MoS_2 and PVA are stronger than the interactions between the WS_2 and PVA, since more S-H-O bonds were formed between MoS_2 and PVA (confirmed by Fourier-transform infrared spectroscopy (FTIR)). Sasu *et al.* [246] functionalized WS_2 with polyethyleneimine (PEI) to increase its compatibility with an epoxy matrix and fabricated

View Article Online
DOI: 10.1039/D4NR01356E

WS_2/epoxy nanocomposites by solution casting. It was found the fracture toughness of the polymer was improved by about 83% with the addition of 0.25 wt% WS_2-PEI nanosheets as shown in Figure 27b. The compressive and flexural strengths were improved significantly (43% and 65%, respectively). In summary, thanks to their excellent mechanical properties and good affinity with the matrices, TMDCs are effective in improving the mechanical performance of polymer composites. More research needs to be conducted in the near future to improve production yields, increase the lateral size of processed flakes and to functionalize TMDC nanosheets chemically (especially covalently) in order to achieve a higher reinforcement efficiency.

Table 5. Mechanical properties of polymer nanocomposites based on TMDCs.

Filler	Matrix	Processing Method	Matrix modulus (GPa)	Optimum filler fraction*	Increase (%)			Ref.
					Young's modulus	Tensile strength	Fracture toughness	
MoS_2	Epoxy	Solution casting	3.45	0.2 wt%	9	33	66	143
f-MoS_2	Epoxy	Solution casting	–	0.25 wt%	–	–	81	248
MNQs	Epoxy	Solution casting	–	0.2 wt%	–	–	81	241
f-WS_2	Epoxy	Solution casting	–	0.25 wt%	–	–	83	246
MoS_2	PVA	Solution casting	3.4	3, 3, 2 wt%	42	56	300	1
f-MoS_2	PVA	Solution casting	–	2 wt%	–	57	–	249
f-MoS_2	PVA	Solution casting	1.93	0.9 wt%	65	–	–	244
f-WS_2	PVA	Solution casting	1.93	2 wt%	52	–	–	245
MoS_2	PVA	Solution casting	2.8	0.25 wt%	14	18	–	250
MoS_2	PEO	Solution casting	0.27	2 wt%	111	–	–	251
f-MoS_2	PEO	Solution casting	0.84	0.9 wt%	88.1	53.3	–	242
f-MoS_2	PA6	In situ polymerization	1.36	1 wt%	80	78	–	244
f-MoS_2	PE	In situ polymerization	0.515	1.23 wt%	56.5	114	–	252
f-MoS_2	PE	In situ polymerization	0.48	1.53 wt%	90	72	–	253
f-MoS_2	PE	In situ polymerization	0.515	0.47, 1.02 wt%	61	105	–	254
MoS_2	PS	Melt mixing	3.8	0.002 wt%	–2	27.5	100	255
f-MoS_2	PI	Solution casting	2.5	1 wt%	43	47	–	256

View Article Online
DOI: 10.1039/D4NR01356E

f-MoS_2	PP	In situ polymerization	0.85	0.52 wt%	61.2	11.4		257
f-MoS_2	WPU	Solution casting	0.12	4 wt%	85	140	–	258
MoS_2	CS	Solution casting	–	0.5 wt%	–	207	–	259
f-MoS_2	PVDF	Solution casting	–	7 wt%	–	61.5	–	260
MoS_2	CN	Solution casting	4.1	6 wt%	100	74	–	261

[a] WPU, waterborne polyurethane; CN, cellulose nanofibril.

4.3.4 MXene-based nanocomposites

Another 2D nanofiller that can be used for the mechanical reinforcement of polymers is MXene nanosheets. Because of their excellent mechanical properties and strong interfacial interactions, MXenes have been used to create multifunctional polymer nanocomposites. Liu *et al*. [262] prepared $Ti_3C_2T_x$/epoxy nanocomposites via solution blending as illustrated in Figure 28. $Ti_3C_2T_x$ MXene was mixed with the curing agent, methyltetrahydrophthalic anhydride (MTHPA), which facilitated the formation of strong chemical bonds and promoted the dispersion of the MXene. With the addition of 0.2 wt% MXene, the elastic modulus and tensile strength were improved from 2.6 to 3.5 GPa and 70.5 to 106.4 MPa, respectively. The flexural modulus and flexural strength were improved from 2.6 to 3.5 GPa and 119.1 to 157.0 MPa, respectively. These enhancements were comparable to the findings for graphene and graphene oxide, making MXenes attractive in the development of polymer nanocomposites with good mechanical properties.

View Article Online
DOI: 10.1039/D4NR01356E

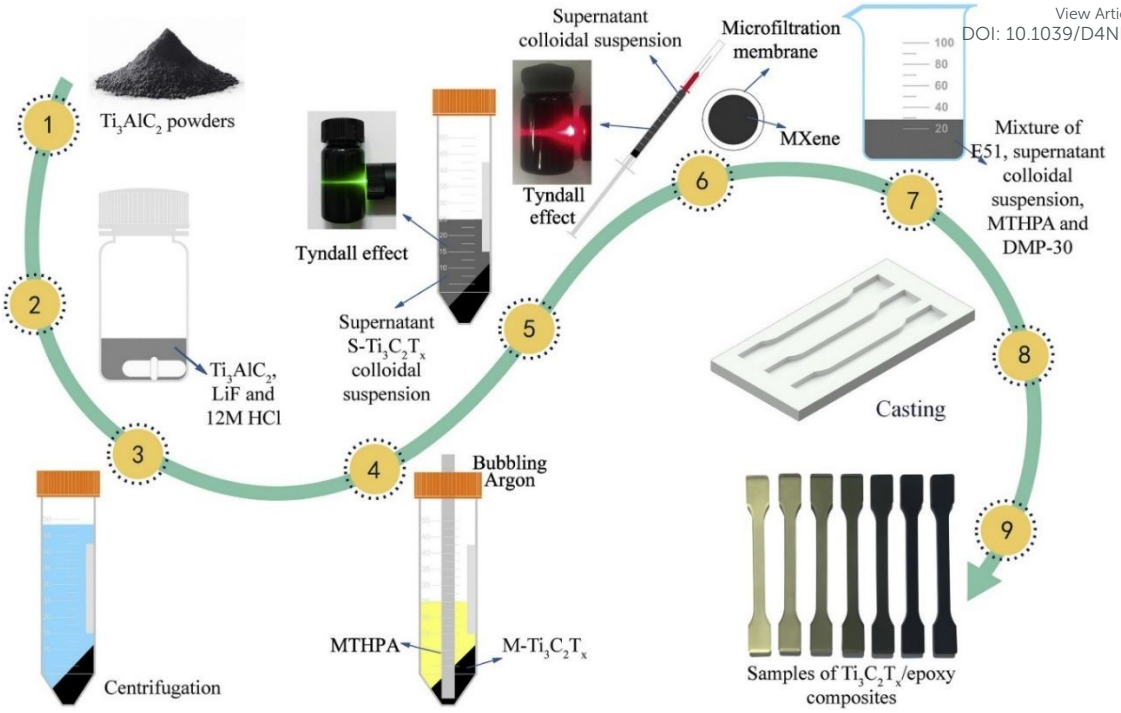

Figure 28. Preparation process of $Ti_3C_2T_x$/epoxy nanocomposites. Reproduced with permission from [262]. Copyright 2020 Elsevier.

As a result of the presence of abundant surface functional groups, MXenes have been combined with various polymers, such as PVA [263], waterborne polyurethane (WPU) [264, 265], cellulose nanofiber (CNF) [266, 267] and aramid nanofiber (ANF) [268, 269] to fabricate bioinspired nanocomposites with nacre structure. Cao *et al.* [266] prepared d-$Ti_3C_2T_x$/CNF nanocomposites with a nacre structure using vacuum filtration (Figure 29a and 29b). The stress-strain curves are shown in Figure 29c, and the optimal mechanical performance was achieved at 50 wt% $Ti_3C_2T_x$ content. The fracture toughness of the composites was improved by ~360% from 3.2 ± 0.2 MJ m^{-3} to 14.8 ± 0.4 MJ m^{-3}. Meanwhile, both the elastic modulus and tensile strength show improvements, increasing from 1.4 ± 0.1 to 3.8 ± 0.3 GPa and from 49.3 ± 4.8 to 135.4 ± 6.9 MPa, respectively. The improvement in mechanical properties is induced by the formation of abundant hydrogen bonds, as a number of terminal groups exist on d-$Ti_3C_2T_x$ nanosheets, while hydroxyl groups are present on the CNFs. In addition, a synergistic effect was observed due to the formation of a "brick-and-mortar" layered structure. With tensile loading,

View Article Online
DOI: 10.1039/D4NR01356E

interlayer hydrogen bonds will break and the d-$Ti_3C_2T_x$ nanosheets will slide over each other. The presence of CNFs reduces the slippage of nanosheets and delays crack propagation at higher loadings. As a result, a high tensile strength was observed. In another study, the tensile strength of $Ti_3C_2T_x$/CNF nanocomposites prepared using a similar method was as high as 416 MPa with 60 wt% $Ti_3C_2T_x$ after vacuum pressing as shown in Figure 29d and the Young's modulus increased to 46.5 GPa with 90 wt% $Ti_3C_2T_x$ [267]. Overall, as mentioned earlier, the excellent intrinsic mechanical properties and surface functional groups make MXenes very attractive candidates for the mechanical reinforcement of nanocomposites.

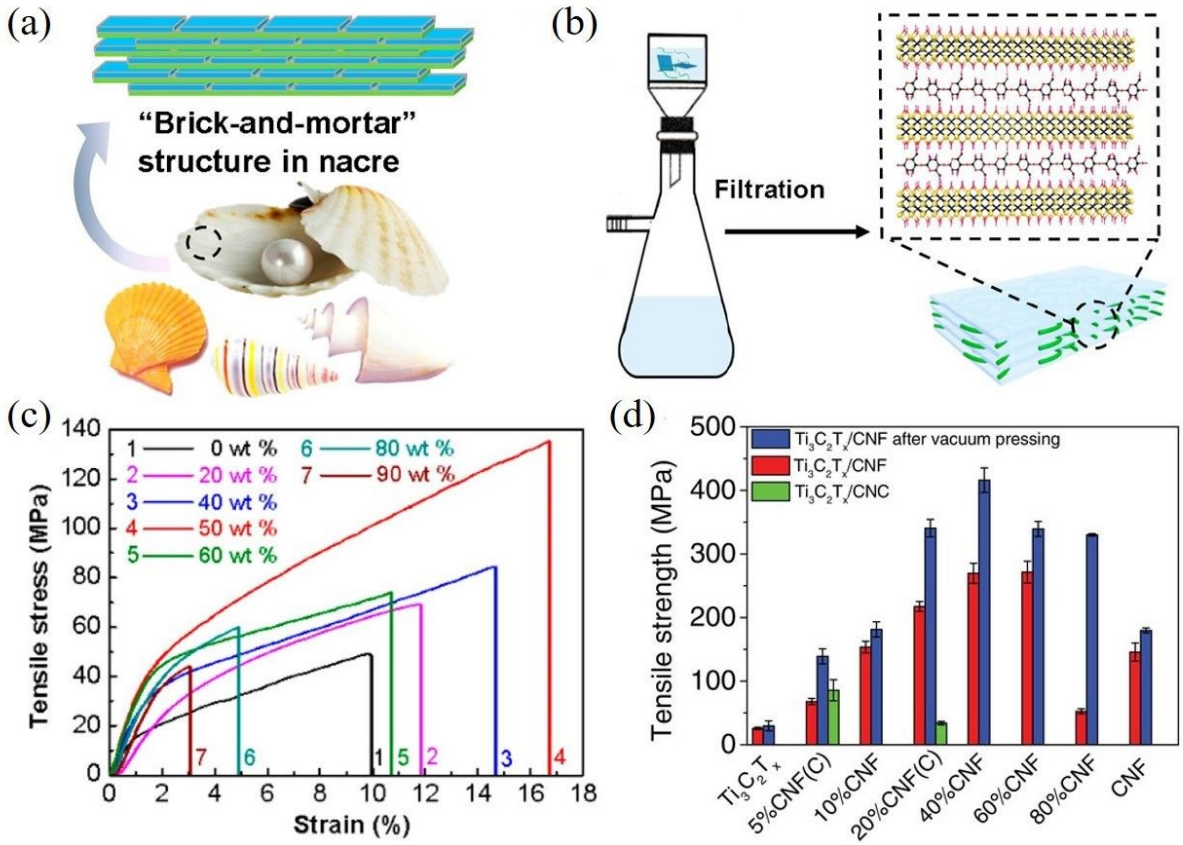

Figure 29. (a) Natural nacre with a "brick and mortar" structure. (b) Vacuum filtration for the preparation of $Ti_3C_2T_x$/CNF composites. (c) Stress-strain curves of $Ti_3C_2T_x$/CNF composites with different $Ti_3C_2T_x$ contents. Reproduced with permission from [266]. Copyright 2018 American Chemical Society. (d) Variations of tensile strength of $Ti_3C_2T_x$/CNF composites with different CNF content. Reproduced with permission from [267]. Copyright 2019 WILEY-VCH Verlag GmbH & Co. KGaA.

View Article Online
DOI: 10.1039/D4NR01356E

Table 6. Mechanical properties of polymer nanocomposites based on MXenes.

Filler	Matrix	Processing Method	Matrix modulus (GPa)	Optimum filler fraction*	Increase (%)			Ref.
					Young's modulus	Tensile strength	Fracture toughness	
Ti_3CN	Epoxy	Solution casting	4.5	90 wt%	182	–	–	142
f-$Ti_3C_2T_x$	Epoxy	Solution casting	2.6	0.2, 0.2, 1 wt%	35	51	107	262
$Ti_3C_2T_x$	Epoxy	Solution casting	3.62	5 wt%	21	–	–	270
f-$Ti_3C_2T_x$	Epoxy	Solution casting	–	0.5 wt%	–	–	70	271
$Ti_3C_2T_x$	Epoxy	Freeze casting	–	0.6 wt%	–	–	710	272
f-$Ti_3C_2T_x$	Epoxy/ PE	Solution casting	3.24	1 wt%	17	56	–	273
$Ti_3C_2T_x$	WEP	Solution casting	0.45	2 wt%	94	40	–	274
TSAC	PMMA	Solution casting	0.289	0.3 wt%	396.5	88	–	275
$Ti_3C_2T_x$	PVA	Vacuum filtration	1	40 wt%	270	203	–	163
$Ti_3C_2T_x$	PVA	Solution casting	2.21	0.6 wt%	27	24	–	169
$Ti_3C_2T_x$	PVA	Solution casting	–	10 wt%	–	205	346	276
f-$Ti_3C_2T_x$	PVA	Solution casting	3.56	2 wt%	64	67	–	277
$Ti_3C_2T_x$	PVC	Solution casting	0.024	10 wt%	177.47	173.55	–	278
$Ti_3C_2T_x$	PANI	Vacuum filtration	–	87.5 wt%	–	670	–	279
$Ti_3C_2T_x$	CNF	Vacuum filtration	1.4	50 wt%	171.4	174.6	362.5	280
$Ti_3C_2T_x$	CNF	Vacuum filtration	8.25	90, 40 wt%	467	131	–	267
$Ti_3C_2T_x$	CNF	Vacuum filtration	5.8	50, 40 wt%	21	24	–	280
$Ti_3C_2T_x$	ANF	Vacuum filtration	–	10 wt%	–	20	–	268
$Ti_3C_2T_x$	ANF	Vacuum filtration	6.2	40, 10, 10 wt%	123	19	13	269
f-$Ti_3C_2T_z$	PLA	Solution casting	–	1 wt%	–	–	144.3	281
$Ti_3C_2T_x$	PP	Melt mixing	–	2 wt%	–	35.3	–	282
$Ti_3C_2T_x$	TPU	Melt mixing	–	0.5 wt%	–	47.1	–	17
$Ti_3C_2T_x$	WPU	Vacuum filtration	2.53	80wt%	211	232	297	264
$Ti_3C_2T_x$	WPU	Solution casting	–	0.5 wt%	–	20	–	283
$Ti_3C_2T_x$	NR	Vacuum filtration	0.00055	6.71 vol%	15000	700	–	284
$Ti_3C_2T_x$	Nafion	Solution casting	0.1046	10 wt%	66	51	–	285

[a] WEP, waterborne epoxy; PANI, polyaniline; NR, natural rubber.

4.3.5 Black phosphorus nanocomposites

View Article Online
DOI: 10.1039/D4NR01356E

The anisotropic mechanical properties of BP make it an interesting nanofiller for the development of polymer nanocomposites. A major disadvantage of BP nanosheets is their instability in air which can restrict the manufacturing methods. Different strategies have been proposed to prepare air-stable BP nanosheets [286-290]. Chemical functionalization is an effective strategy to improve both the air stability and mechanical reinforcement from BP nanosheets. Qiu *et al*. [288] prepared BP/polyurethane acrylate (PUA) composites using solution blending. The BP nanosheets were functionalized using cobaltous phytate to improve their air-stability. It was found that 3 wt% functionalized BP can increase the storage modulus of the nanocomposites at 25 ℃ by 75% compared with the neat matrix (1.9 GPa). The tensile strength of the composites was improved by 60% to 21.1 MPa. Moreover, the BP nanocomposites were stable after being exposed to environmental conditions for 4 months. Ni *et al.* [287] prepared BP/PVA nanocomposites via solution casting and the lateral size of the BP nanosheets was in the order of 200 to 300 nm. The formation of P-O covalent bonds, confirmed by both Raman spectroscopy and X-ray photoelectron spectroscopy (XPS), stabilised the BP nanosheets and improved the mechanical properties of the nanocomposites. The Young's modulus of the pure PVA was doubled from 5.6 GPa to 11.4 GPa with the addition of 3.1 wt% nanosheets. The tensile strength was improved by ~88% from 168 MPa to 317 MPa. Moreover, the BP/PVA composites were stable after being exposed to environmental conditions for one year. Overall, chemical functionalization can not only stabilise BP nanosheets, but also improve the mechanical reinforcement due to strong interfacial interactions between the functionalized BP nanosheets and polymer matrices.

Protective layers have been utilised to fabricate air-stable BP nanosheets for the reinforcement of polymer nanocomposites [289, 290]. Qiu *et al.* [289] modified few-layer BP nanosheets by polyphosphazene (PZN) functionalization and fabricated BP/epoxy nanocomposites (Figure 30). The sandwich-like PZN-BP-PZN structure, shown in Figure 31, was formed through direct polymerization and the BP nanosheets were found to be stable in air due to the wrapping of the PZN hybrids. The hybrid structures also prevented BP nanosheets from agglomeration within the nanocomposite, as confirmed by TEM

images. Meanwhile, the mechanical properties of the epoxy composites were improved significantly with a small loading of BP nanosheets. For instance, the storage modulus of the composites at room temperature was improved by ~130% with 1 wt% of PZN-functionalized BP nanosheets. This was attributed to the excellent mechanical properties of BP nanosheets and good interfacial interactions between the PZN-BP-PZN and epoxy matrix.

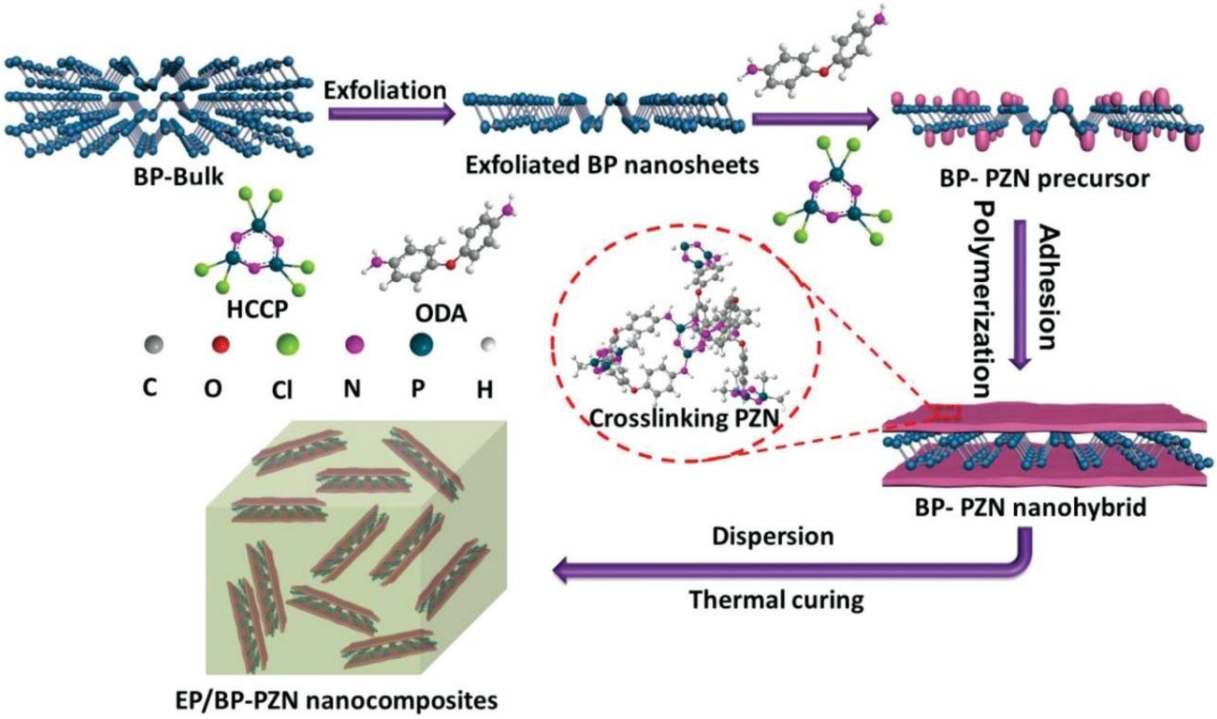

Figure 30. Preparation of PZN-functionalized BP nanosheets and BP/epoxy nanocomposites. Reproduced with permission from [289]. Copyright 2019 WILEY-VCH Verlag GmbH & Co. KGaA.

Overall, even though air instability may hinder the applications of BP nanosheets, it has provided opportunities for researchers to explore different strategies to fabricate air-stable BP nanosheets. These strategies promote the interactions between BP nanosheets and matrices, prevent BP nanosheets from agglomeration and therefore improve the final mechanical performance of the nanocomposites.

Table 7. Mechanical properties of polymer nanocomposites based on black phosphorus.

Filler	Matrix	Processing Method	Matrix modulus (GPa)	Optimum filler fraction*	Increase (%)			Ref.
					Young's modulus	Tensile strength	Fracture toughness	

View Article Online
DOI: 10.1039/D4NR01356E

f-BP	Epoxy	Solution casting	–	1 wt%	–	71		291
f-BP	Epoxy	Solution casting	–	1 wt%	–	27.2	–	292
f-BP	Epoxy	Solution casting	–	1 wt%	–	56	–	293
BP	PVDF	Solution casting	1.46	2.5 wt%	56.8	–	–	286
BP	PVA	Solution casting	5.6	3.11 wt%	104	88	–	287
BP	PVA	Solution casting	0.88	5 wt%	101.5	131.2	–	294
f-BP	TPU	Solution casting	–	0.5 wt%	–	27.6	–	295
f-BP	TPU	Solution casting	–	0.5 wt%	–	55	–	296
f-BP	NFC	Vacuum filtration	–	25 wt%	–	312	–	297
f-BP	PLA	Solution casting	–	1 wt%	–	11	–	298

[a] NFC, nanofibrillar cellulose.

4.3.6 Other nanocomposites

Polymer composites based on other 2D nanosheets such as covalent organic frameworks (COFs) [299-303] and metal organic frameworks (MOFs) [243, 304-306] have also been investigated. Mu *et al.* [299] prepared COFs/TPU nanocomposites, where the bulk COFs were exfoliated into nanosheets via a ball-milling method. The exfoliated nanosheets were mixed with the TPU and subsequently hot-pressed into nanocomposite films. It was found that the addition of 3.2 wt% COFs gave the optimal reinforcement, whereby the elastic modulus and tensile strength of the composites were improved by 45% and 64%, respectively. A good dispersion of COFs was reported as no obvious agglomeration was seen in SEM images. The interaction between the COFs nanosheets and TPU matrix was strong due to the formation of hydrogen bonds. In summary, strong interlayer interactions and good compatibility with matrices can improve the mechanical properties of composites based on COFs and MOFs to a certain extent. However, their relatively-poor intrinsic mechanical properties will hinder their further applications and hybrid structures or combinations with other fillers might be needed to achieve good reinforcement at low filler contents.

Table 8. Mechanical properties of polymer nanocomposites based on COFs and MOFs.

Filler	Matrix	Processing Method	Matrix modulus (GPa)	Optimum filler fraction*	Increase (%)			Ref.
					Young's modulus	Tensile strength	Fracture toughness	

View Article Online
DOI: 10.1039/D4NR01356E

COFs	TPU	Solution casting	–	3.2 wt%	45	64	–	299
COF	TPU	Solution casting	–	3 wt%	–	69.6	–	307
f-COFs	CS	Solution casting	0.0123	1.6 wt%	94.3	27.9	–	300
f-COFs	PLA	Solution casting	–	1 wt%	68.6	–	–	302
COF	PEG	Solution casting	0.36	50 wt%	154	116	–	303
MOF	Epoxy	Solution casting	1.56	1.2 wt%	–6	34	–	308
MOF	PI	In situ polymerization	17.8	3 wt%	85	35	–	309
f-MOFs	PLA	Solution casting	3.5	2 wt%	14	17	–	243
f-MOFs	PLA	Solution casting	–	5 wt%	–	47	–	306

5. Hybrid nanocomposites

Two or more nanofillers can be incorporated into a single matrix to improve the mechanical performance of polymer nanocomposites, leading to additive or synergistic effects. These synergistic effects are usually related to the creation of various interfacial bonds between the filler and the matrix that induce a significant improvement in the mechanical properties. Unlike the weak van der Waals bonds, the presence of both covalent and non-covalent bonds such as hydrogen bonds, ionic bonds and π-π interactions between the filler and the matrix can improve the interfacial shear strength and hence the stress transfer efficiency. The combination of these bonds within a composite can improve the mechanical performance synergistically. A number of papers have reported synergistic improvements of various properties of nanocomposites as a result of combinations of nanofillers with different geometries (2D, 1D, 0D and their combinations). There is therefore an opportunity to improve the mechanical properties of nanocomposites using hybrid fillers for the creation of different types of chemical bonds and constrain the movement of the macromolecular chains of the matrix effectively. In this section, we will review the combination of 2D fillers with fillers of different dimensions including 2D-2D, 2D-1D and 2D-0D and their additive or synergistic effects upon the mechanical reinforcement of nanocomposites.

5.1. 2D-2D nanocomposites

View Article Online
DOI: 10.1039/D4NR02356E

The exceptional multifunctional properties of different types of 2D nanosheets have led to a large number of publications dealing with the preparation and properties of 2D-2D hybrid nanocomposites [146, 310-322]. The intrinsic mechanical properties of hybrid nanosheets can lead to reinforcement of the composites, most commonly as a result of additive effects. More importantly, the use of hybrid nanosheets can promote uniform dispersions or the formation of ordered, stacked structures that are known to lead to improved stress transfer efficiency.

Cui *et al.* [311] prepared PS and polyamide 6 (PA6) composites reinforced with graphene nanoplatelets and h-BN nanosheets by hot pressing at 180 ℃ under 15 MPa pressure. The Young's modulus and hardness of the composites were characterized by nanoindentation. In terms of PS composites, the Young's modulus was only increased slightly from 4.32 to 4.7 GPa upon the addition of 20 wt% graphene (PSG20) or BN (PSB20) nanosheets. The addition of 1.5 wt% h-BN to PSG20 (PSG20-B1.5) improved the Young's modulus of the composites significantly from 4.7 to 6.3 GPa as shown in Figure 31a. According to the authors, the h-BN nanosheets were located between the graphene interspaces as illustrated in Figure 31b. This improved stress transfer efficiency from the matrix to nanosheets was the result of more interfaces being involved in stress transfer. Furthermore, the h-BN nanosheets were stacked on graphene nanosheets, which helped reduce stress concentrations and modified the crack propagation mechanism. These two factors synchronously improved the elastic modulus of the composites significantly. In another study, f-BNNS and $Ti_3C_2T_x$ MXene were introduced into a polybenzimidazole (PBI) matrix through ball milling as illustrated in Figure 31c [319]. With the addition of 25 wt% f-BNNS/ $Ti_3C_2T_x$, the yield and ultimate tensile strengths of the composites were improved by 61.1 % and 39.8% to 175.5 MPa and 189.6 MPa, respectively. The synergistic effect originates from the interaction between the f-BNNS and $Ti_3C_2T_x$, which not only prevents agglomeration but also facilitate the formation of bridge connections between the fillers. These studies show that the use of hybrid nanosheets can further improve the mechanical properties of composites compared with the use of individual types of nanosheets.

View Article Online
DOI: 10.1039/D4NR01356E

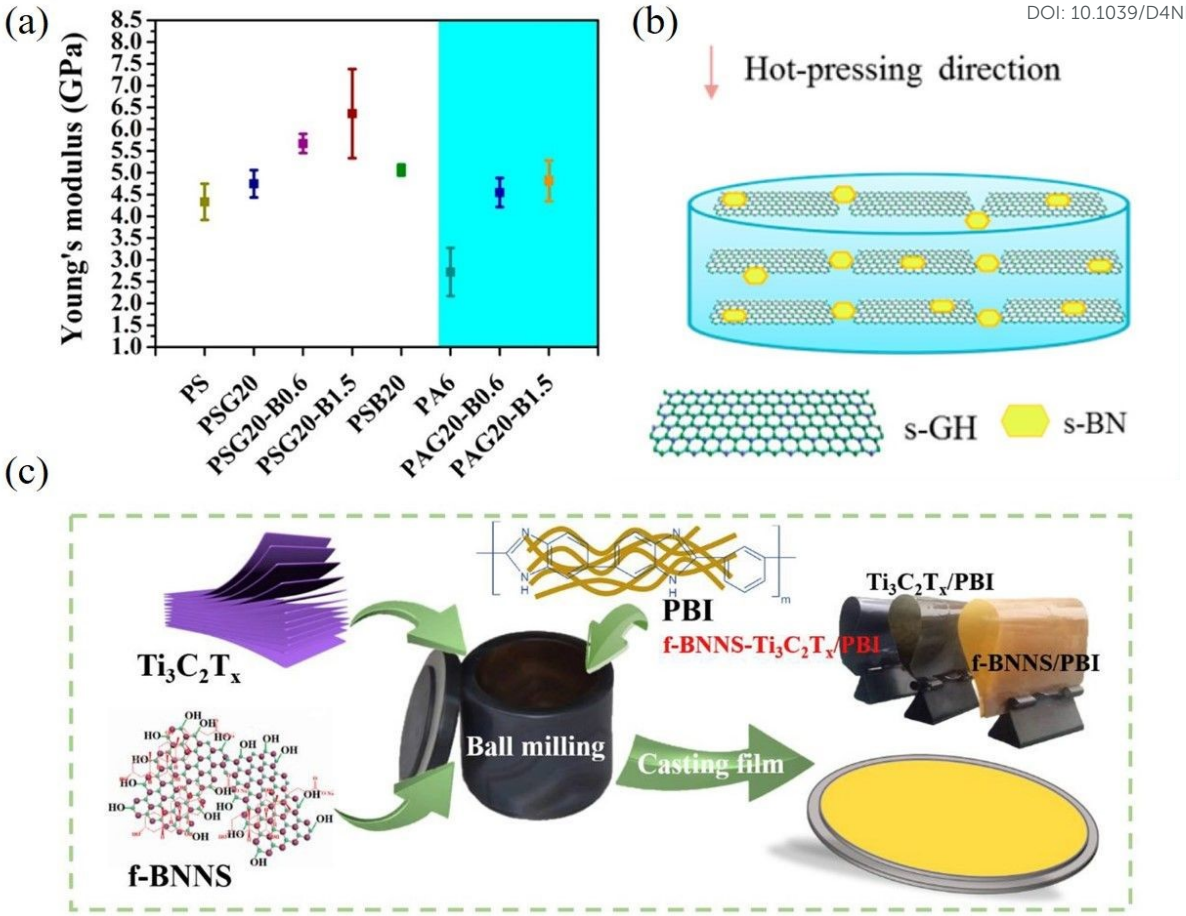

Figure 31. (a) Variation of the Young's modulus of PS and PA composites with the addition of graphene and BN. (b) Scheme for the stacking of graphene (s-GH) and BN (s-BN). Reproduced with permission from [311]. Copyright 2015 American Chemical Society. (c) Preparation process of PBI-based composite films. Reproduced with permission from [319]. Copyright 2019 Elsevier.

Wan *et al.* [317] demonstrated the synergistic effect between GO and MoS_2 for the the toughening of TPU nanocomposites. The GO/MoS_2/TPU composites were prepared by a filtration method, creating a nacre-type structure. The corresponding stress-strain curves for different contents of MoS_2 were obtained as shown in Figure 32a [317]. The TPU content was kept constant at 10 wt%. Compared with GO/TPU composites, the tensile strength and fracture toughness both increased with the addition of MoS_2 nanosheets and reached their maximum values at 4.4 wt% of MoS_2, as shown in Figure 32b and 33c. The tensile strength was improved by 40% from 166.7 MPa to 235.3 MPa. Additionally, the

View Article Online
DOI: 10.1039/D4NR01356E

toughness (determined from the area under the stress-strian curve) was more than doubled from 3.3 MJ m^{-3} to 6.9 MJ m^{-3}. The fractured morphology of rGO/MoS_2/TPU composites is shown in Figure 32d. According to the authors the application of an external load will result in the slippage of GO nanosheets and the formation of cracks due to the breakage of hydrogen bonds. The friction between GO and MoS_2 leads to the movement of MoS_2 nanosheets. Due to the excellent lubrication properties of layered MoS_2, more energy is required for crack propagation as the crack is deflected, and the toughness is enhanced. The incorporation of MoS_2 at loadings beyond 4.4 wt% degrades the tensile strength and toughness probably due to the restacking of the nanosheets. Recently, ultra-tough nanocomposites based on rGO+MXene [323], and rGO+BP [324] have been reported from the same group. Except for the toughening mechanism described above, the synergistic effects between covalent bonds and π-π interactions play an important role in the improvement of tensile strength. These studies demonstrate a promising strategy for the improvement of both the tensile strength and toughness of nanocomposites.

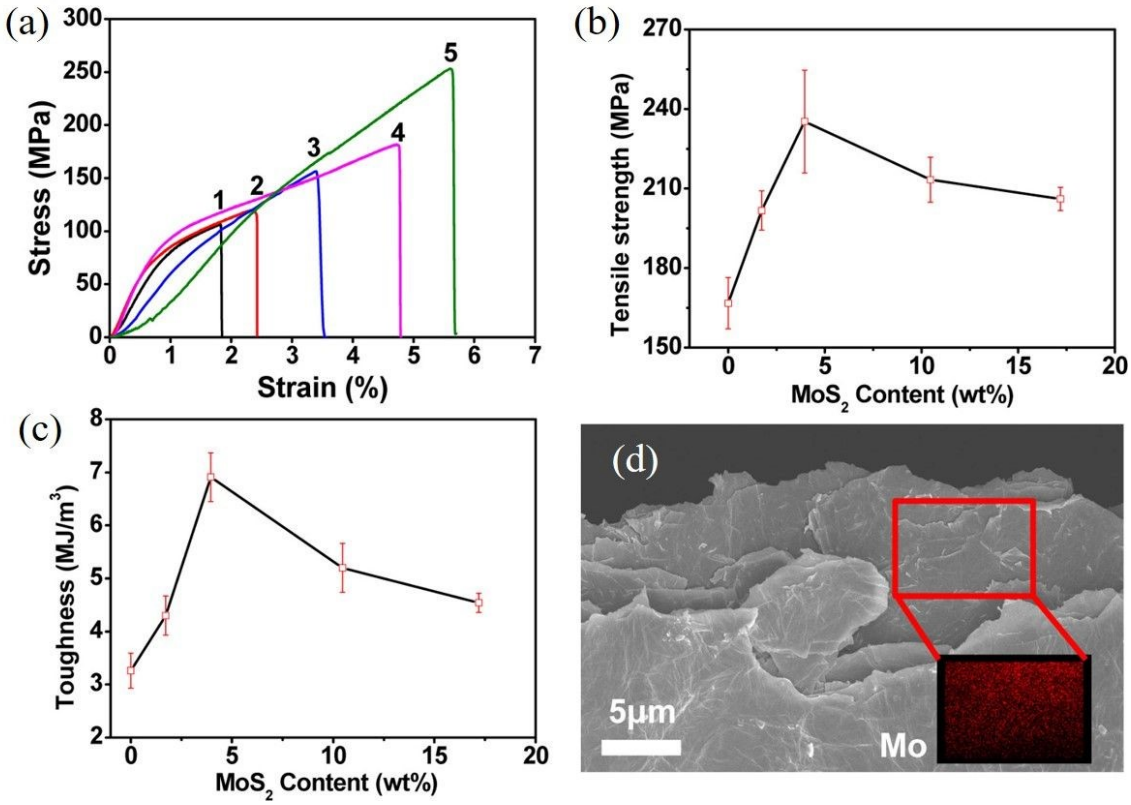

Figure 32. (a) Stress-strain curves of GO/MoS_2/TPU nanocomposites. 1 to 5 represent GO film,

GO/TPU, rGO/TPU, GO/MoS_2/TPU, and rGO/MoS_2/TPU composites, respectively. Dependence of the (a) Tensile strength and (b) toughness of the composites with the loading of MoS_2. (d) Fracture surface of the rGO/MoS_2/TPU composites. Reproduced with permission from [317]. Copyright 2015 American Chemical Society.

In summary, the use of hybrid nanosheets shows huge potential in the improvement of mechanical properties of nanocomposites due to additive or synergistic effects. The good mechanical properties and unique characteristics of diverse 2D nanosheets can be combined together to reinforce nanocomposites. To achieve additive or synergistic effects, it is important to promote homogeneous dispersion of hybrid nanosheets; otherwise, agglomeration phenomena may degrade the mechanical performance of the hybrid nanocomposites.

Table 9. Mechanical properties of hybrid 2D-2D nanocomposites. *when more than one optimum filler fractions are mentioned, they should correspond to the optimum filler fractions for improvement of modulus, strength and toughness, sequentially.

Filler 1	Filler 2	Matrix	Processing Method	Matrix modulus (GPa)	Optimum hybrid filler (f1/f2) fraction*	Increase (%)			Ref.
						Young's modulus	Tensile strength	Fracture toughness	
C	GNP	Epoxy	Freeze casting	–	5 wt%	–	–	81.4	325
C	GNP	PP	Melt mixing	0.6	3/20 wt%	285	17	–	3[illegible]
GNP	BN	PS	Hot pressing	4.32	20/1.5 wt%	46	–	–	31[illegible]
rGO	BN	PVA	Solution casting	2.3	0.8, 0.8, 1.6 wt%	22	18	100	312
GO	BN	PU	Solution casting	0.03	0.5 wt%	140	85	–	314
GNP	BN	PVDF	Solution casting	–	2.5/30 wt%	–	63	–	315
f-GO	f-BN	PU	Solution casting	0.05	3 wt%	76	62	–	316
f-GO	f-BN	TPU	Solution casting	0.036	10 wt%	2729	381	–	326
GNP	MoS_2	PVC	Melt mixing	0.0388	2/2 wt%	566	38	–	318
GO	$Ti_3C_2T_x$	EAA	Solution casting	0.1	10 wt%	354	78	–	327
GO	$Ti_3C_2T_x$	PI	Solution casting	11	1/0.3 wt%	18	54	–	328
GO	f-BP	PVA	Solution casting	–	25 wt%	–	114	236	329
GO	Clay	UP	Solution casting	3.27	1 wt%	93	130	–	330

View Article Online DOI: 10.1039/D4NR01356E

BN	MoS_2	Epoxy	Solution casting	0.34	0.25, 1 wt%	58	95		146
BN	MoS_2	PU	Solution casting	0.3	0.5 wt%	80	–	–	331
f-BN	$Ti_3C_2T_x$	PBI	Solution casting	2	25 wt%	97	39.8	–	319
MoS_2	WS_2	PLA	Solution casting	0.01	1/1 phr	47	86	58	321
MoS_2	Bi_2Se_3	Epoxy	Solution casting	–	1 wt%	–	31	–	322

[b] EAA, poly (ethylene-co-acrylic acid); UP, unsaturated polyester.

[b] GP, graphite platelet.

5.2. 2D-1D nanocomposites

The addition of 1D nanomaterials to composites based on 2D nanomaterials has been widely explored in an attempt to improve their mechanical performance. Several 1D nanomaterials possess excellent mechanical properties and good compatibility with polymer matrices. For example, the Young's modulus and tensile strength of carbon nanotubes (CNTs) were measured to be 1 TPa and 100 GPa [332]. Even though the elastic modulus of nanofibrillar cellulose (~150 GPa) is relatively low compared to CNTs, there are abundant hydroxyl groups on its surface which is beneficial for the formation of strong interfacial bonds with other fillers or matrices [164]. Therefore, 1D nanofillers can not only improve the mechanical properties of composites due to additive effects, but also promote the dispersion of 2D nanosheets in matrices and therefore lead to additional synergistic effects.

Carbon nanotubes are extensively used in hybrid nanocomposites, such as in combination with graphene [333-336], BN [337-342], MoS_2 [343-345] and MXenes [346-348]. Li *et al.* [333] prepared epoxy composites based on GNPs and CNTs. They compared the mechanical properties of the composites containing only GNPs or CNTs, and GNPs+CNTs (a mixture of GNPs and CNTs) or CNTs-GNPs (CNTs grown on GNPs), as seen from Figure 33a to 33d. It was found that the combination CNTs-GNPs not only gave the highest elastic modulus and tensile strength, but also the highest fracture strain. With the addition of 0.5 wt% CNTs-GNPs, the elastic modulus and tensile strength of the composites were improved by 40% and 36% respectively as shown in Figure 33f and 33g. Meanwhile, the fracture strain was not reduced in contrast to the other three cases where the fracture behaviour was degraded severely

View Article Online
DOI: 10.1039/D4NR01356E

(Figure 33h). These excellent mechanical properties were attributed to the formation of strong bonds between the CNTs and GNPs. The conjunction between CNTs and GNPs promoted the homogeneous distribution both nanofillers, and prevented both the GNPs from agglomeration and the CNTs from curling. This conjunction therefore promotes good stress transfer and hence the mechanical properties to be achieved.

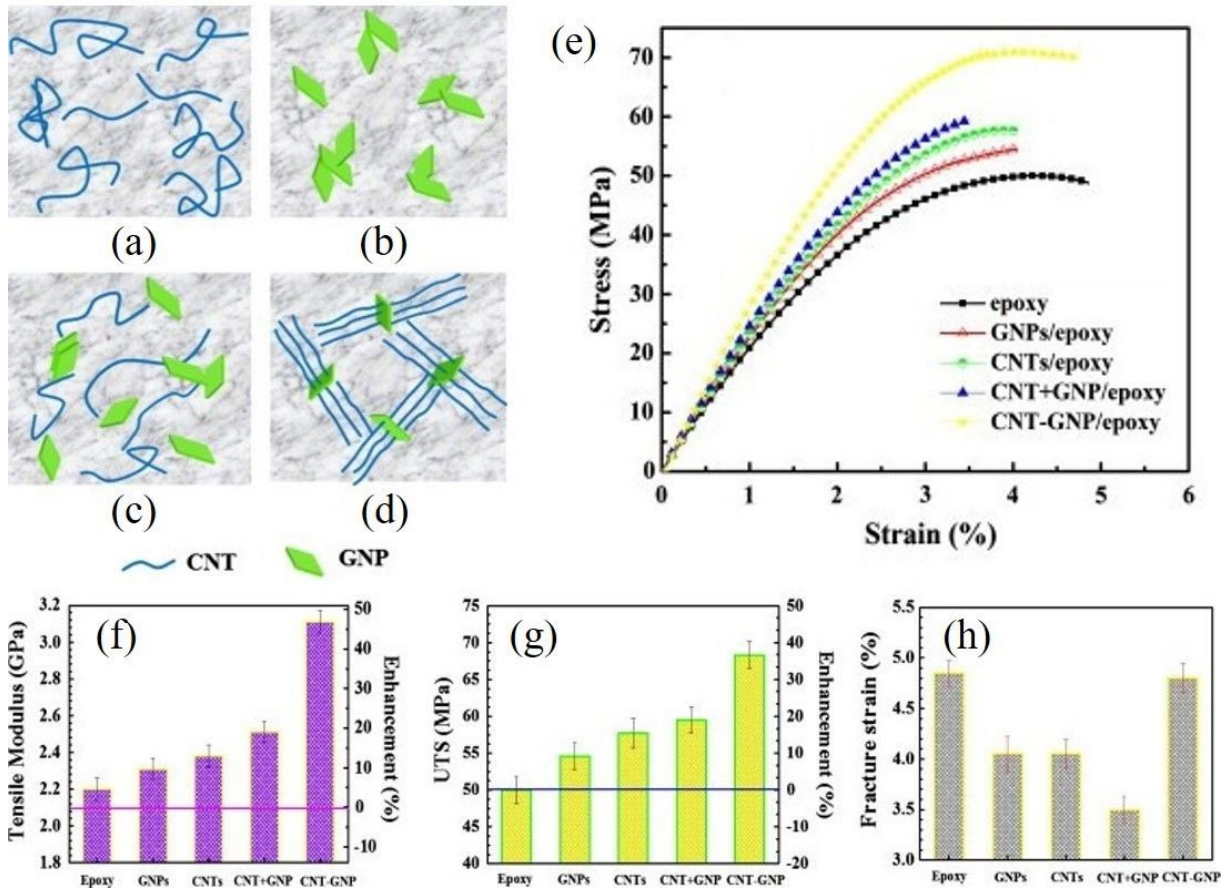

Figure 33. (a-d) CNTs, GNPs, CNTs and GNPs, and CNTs on GNPs. (e) Stress-strain curves of the epoxy composites based on CNTs and GNPs. (f-h) Variations of elastic modulus, tensile strength and fracture strain of epoxy composites with GNP and CNT. Reproduced with permission from [333]. Copyright 2012 Elsevier.

CNTs can act as bridges to connect 2D nanosheets and improve load transfer. For example, Park *et al.* [341] fabricated PI composites based on h-BN nanosheets and CNTs. The BN-Fe-CNT hybrids

View Article Online
DOI: 10.1039/D4NR01356E

were formed and each part was connected by amide bonds as shown in Figure 34a. This improved the mechanical performance of the final composites significantly. As seen from Figure 34b and 34c, the elastic modulus of the composites was increased from 2.1 to 5.4 GPa with the addition of 2 wt% of nanofillers. The tensile strength was improved considerably from 67 MPa to 174 MPa. Such improvements can be attributed once again to the enhanced stress transfer due to the formation of interlinked nanofillers. These interconnected nanofillers reduce the curling of the CNTs and the agglomeration of the h-BN nanosheets. Overall, the good intrinsic mechanical properties and strong interactions with the 2D nanosheets, as well as polymer chains, make CNTs appealing in the fabrication of hybrid 2D-1D nanocomposites.

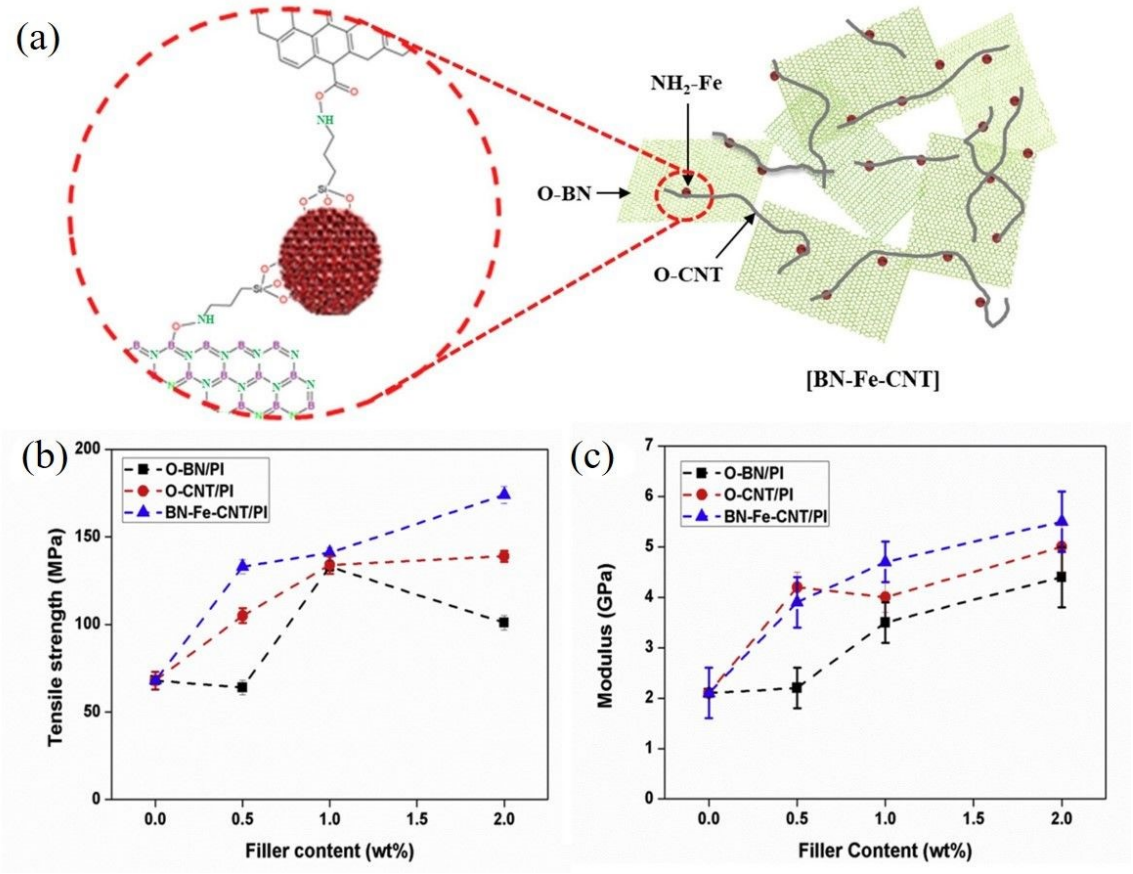

Figure 34. (a) Interconnection of BN-Fe-CNT. (b, c) Variations of tensile strength and modulus of PI composites with O-BN, O-CNT and BN-Fe-CNT. Reproduced with permission from [341]. Copyright 2020 Elsevier.

View Article Online
DOI: 10.1039/D4NR01356E

Recently, a liquid flow assisted method has been used to align 2D nanosheets in polymer nanocomposites [349]. The dispersion of 2D nanosheets was achieved by the superspreading of the reaction solution with GO and sodium alginate (NaAlg) on the surface of polyacrylamide hydrogel. Gel-drying was then used to prepare the nanocomposites. Based on this process, polymer nanocomposites with NaAlg, PVA, GO, nanoclay, and CNTs (5:4:1:2:0.03 by weight) showed impressive mechanical properties with an elastic modulus of nearly 200 GPa, a strength of 1215 MPa and a toughness of 6.9 MJ m^{-3}. This impressive mechanical performance was claimed to be because the aligned 2D nanosheets formed a critical interphase. This corresponds to the mechanism illustrated in Figure 19b, where the mechanical performance of the composites increases quadratically with the increase of filler loading due to strong interactions between the fillers and matrix. This study demonstrates a promising strategy for the alignment of 2D nanosheets in polymer nanocomposites. It shows that the tremendous potential of 2D nanosheets in the mechanical reinforcement of nanocomposites should be explored further.

Other one-dimensional materials, such as carbon fibres (CFs) [350-355] or glass fibers (GFs) [356], nanorods or nanowires (NWs) [357-361] and nanocelluloses [362-365] have also been incorporated into nanocomposites to improve their mechanical performance. For example, Papageorgiou *et al.* [351] studied the additive effect of GNPs and CFs on the mechanical properties of PEEK composites. The Young's modulus was improved from about 3.3 GPa to 4.5 GPa with the addition of 14 vol% GNPs. It was further improved to about 7 GPa with the addition of 34 vol% of a hybrid GNP/CF filler with the improvement being attributed to the additive effect of the presence of GNPs and CFs, in terms of their high values of elastic modulus. Furthermore, the high aspect ratio of GNPs restricted the movement of the macromolecular chains and promoted the stress transfer efficiency. Overall, the use of hybrid 1D and 2D nanofillers can improve the mechanical properties of composites due to additive effects. Synergistic effects can further contribute to the mechanical reinforcement.

View Article Online
DOI: 10.1039/D4NR01356E

Table 10. Mechanical properties of hybrid 2D-1D nanocomposites.

Filler 1	Filler 2	Matrix	Processing Method	Matrix moduls (GPa)	Optimum hybrid filler (f1/f2) fraction*	Increase (%)			Ref.
						Young's modulus	Tensile strength	Fracture toughness	
GNP	CNT	Epoxy	Solution casting	2.2	0.5 wt%	40	36	–	333
GNP	CNT	Epoxy	Mechanical mixing	–	0.5 wt%	–	–	76	366
GNP	MWCNT	UHMWPE	Hot pressing	0.401	0.5 wt%	37.1	30.8	–	334
GO	CNT	PVA	Solution casting	3.1	10/5, 6/3 wt%	106	80	–	367
GNP	MWCNT	Epoxy	Solution casting	2.646	0.9/0.1 wt%	27.1	35.4	–	368
f-GNP	f-CNT	TPU	Solution casting	0.0207	3 wt%	90	32	–	369
GNP	CNT	UHMWPE	Hot pressing	0.59	0.3/0.1 wt%	37.3	33.4	–	335
f-GO	f-CNT	PI	In situ polymerization	7.7	0.9/0.1 wt%	312	221	200	370
GO	CNT	PI	Solution casting	2.47	1.1 wt%	94	118	138	371
GNP	f-CNT	PLA	Melt mixing	1.5	0.5 wt%	66	44	–	372
GO	CNT	PS	Hot pressing	0.967	1.02 wt%	19	64	–	336
BN	MWCNT	Epoxy	Solution casting	3.25	0.5/0.3 wt%	38	25	–	337
BN	f-CNT	Nomex/PTFE	Solution casting	5.2	0.5/0.5 wt%	37.5	22.7	–	338
BN	CNT	Epoxy	Solution casting	2.03	7.6 wt%	37	300	–	339
f-BN	f-CNT	PI	Solution casting	2.1	2 wt%	170	160	–	341
BN	CNT	HDPE	Mechanical mixing	1.47	0.15/0.25 wt%	102	–	–	342
MoS_2	MWCNT	Epoxy	Solution casting	2.6	1 wt%	47.2	49.6	–	343
GO	CF	PU	Solution casting	0.00314	1.1 wt%	648	46	–	350
MoS_2	CF	Epoxy	Solution casting	1.25	0.8 wt%	53	77	–	355
GO	SiC	PPC	Solution casting	3	3 wt%	183	46	–	359
f-BN	Cu	PVA	Solution casting	1.33	10/0.1 wt%	303	123	–	361
GO	CNC	PVA	Solution casting	0.86	5 wt%	320	124	159	363
BN	CNC	PVA	Solution casting	2.3	3.2, 3.2, 0.8 wt%	49	42	100	365
f-BN/Ti_3C_2Tx	Ag	PBI	Solution casting	2	50.5	255	104	–	373

View Article Online
DOI: 10.1039/D4NR01356E

$Ti_3C_2T_x$	CNT	TPU	Hot pressing	–	3 wt%	–	79.5	–	348
$Ti_3C_2T_x$	CNT	NBR	Mechanical mixing	0.00078	21.1/2.9 vol%	429	146	–	347
$Ti_3C_2T_x$	f-CNT	WPU	Solution casting	0.044	0.95/0.05 wt%	69	25	–	374
$Ti_3C_2T_x$	MWCNT	PVA	Solution casting	2.23	0.6/0.6 wt%	52	48	–	375
$Ti_3C_2T_x$	MWCNT	Epoxy	Mechanical mixing	3	0.5/0.5 wt%	31	6	85	147
$Ti_3C_2T_x$	ATP	Epoxy	Solution casting	2.6	0.2/0.25, 0.2/1 wt%	38	88	195	376
$Ti_3C_2T_x$	CF	Epoxy	Solution casting	2.6	2 wt%	46	100	216	377
Ti_3C_2	SAF	PP	Melt mixing	0.879	0.3/5 wt%	35.3	28.1	–	378

[a] PTFE, polytetrafluoroethylene; PPC, poly(propylene carbonate); NBR, nitrile rubber.

[b] MWCNT, multiwall carbon nanotube; CNC, cellulose nanocrystal; ATP, attapulgite; SAF, short aramid fibre.

5.3. 2D-0D nanocomposites

Another strategy for improving the mechanical performance of 2D materials-based polymer nanocomposites is the introduction of zero-dimensional (0D) nanoparticles or nanospheres. Thanks to their spherical geometry, the combination of 0D and 2D nanofillers can create interlocking interfaces or core-shell structures that are more resistant to sliding or fracture. In addition, the presence of 0D nanofillers can inhibit the agglomeration of 2D nanosheets and promote homogeneous distributions in matrices. Different types of 0D nanoparticles such as SiO_2 [379-386], Al_2O_3 [387-390], Ag [391, 392], Fe_2O_3 [393], carbon black (CB) [394-396], nanodiamond (ND) [397-399], lignin [400], zinc ferrite (ZF) [401], and polyphosphazene (PZS) [402, 403] have been explored.

Silica nanoparticles are widely used in polymer nanocomposites considering their excellent mechanical properties (~ 150 GPa modulus) [404]. Zhang *et al.* [384] prepared SiO_2@ h-BN/PVA composites via two different methods: solution blending and vacuum filtration. The bulk h-BN was exfoliated into nanosheets by ball milling and the SiO_2@h-BN hybrids were prepared by hydrolysis as shown in Figure 36a. For the solution casting method, the mixtures were poured into a mould and dried

for twelve hours; for the vacuum filtration method, the mixtures were filtered by a vacuum system and dried in a vacuum oven. The Young's modulus and tensile strength were 1.8 GPa and 47 MPa for the neat PVA. It was found that composites prepared by vacuum filtration showed better mechanical performance due to a homogeneous distribution of fillers compared to the ones prepared by solution casting. On the other hand, the use of SiO_2 improved the mechanical properties of the composites significantly. The Young's modulus and tensile strength of the composites were improved to 4.2 GPa and 110 MPa with the addition of 14.5 wt% h-BN, while these properties were improved further to 5.9 GPa and 156 MPa with the addition of 15.2 wt% SiO_2@h-BN hybrids (14.5 wt% h-BN and 0.7 wt% SiO_2). This further improvement in mechanical properties with the addition of SiO_2 was attributed to a number of factors. As can be seen from Figure 36b more fillers and interfaces are involved in the crack propagation procedure with the addition of SiO_2, which leads to an increase in the resistance to fracture. This study demonstrates that the synergistic combination of 0D and 2D nanofillers is another effective strategy to improve the mechanical performance of nanocomposites.

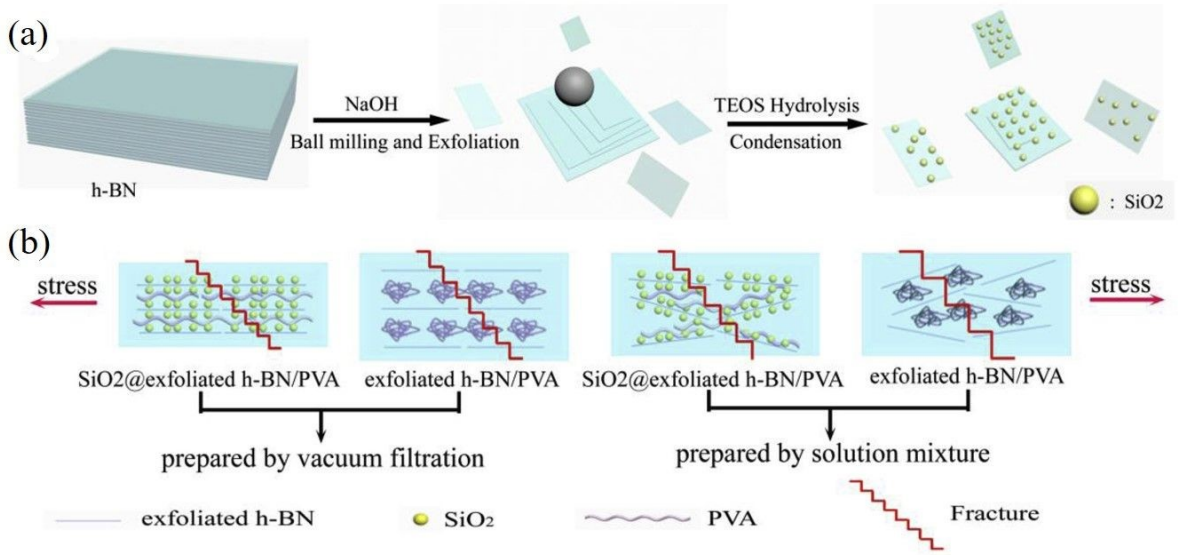

Figure 36. (a) Preparation of boron nitride nanosheets and SiO_2@BN bybrids. (b) Fracture behaviour of PVA composites with h-BN and SiO_2@h-BN prepared by solution casting and vacuum filtration. Reproduced with permission from [384]. Copyright 2018 Elsevier.

View Article Online
DOI: 10.1039/D4NR01356E

The wrapping of nanoparticles with nanosheets to form a core-shell structure is an effective technique to improve the mechanical properties of nanocomposites [385]. Zhou *et al.* [402] prepared PZS@MoS_2 structures whereby polyphosphazene (PZS) spheres were synthesized with active hydroxyl groups on their surface. The MoS_2 nanosheets were assembled onto the nanospheres to form core-shell structures using a hydrothermal process. The PZS@MoS_2/epoxy nanocomposites were then fabricated using solution blending and this strategy improved the storage modulus of the composites significantly. With the addition of 2 wt% PZS and MoS_2 (individually), the storage modulus was improved by 17.2 and 51.9% respectively. This means that the effective elastic modulus of PZS is relatively low compared to the value for MoS_2. Surprisingly, the storage modulus of the composite was improved by 91% with the addition of 2 wt% PZS@MoS_2as the hydroxyl groups in the PZS@MoS_2 hybrids improved the interfacial adhesion between the filler and the matrix. In addition, the core-shell structure with high stiffness restricted the movement of molecular chains and so improved the storage modulus of the nanocomposites.

An advantage of hybrid 2D-0D nanofillers is the formation of interlocking interfaces, which means that higher loading is needed to induce fracture failure. Zhang *et al*. [397] investigated the synergistic effect of GO and ND on the fracture toughness of epoxy nanocomposites. The NDs were processed by amine-terminated (3-aminopropyl) triethoxysilane and the GO nanosheets were processed by (3-glycidyloxypropyl) trimethoxysilane. Strong covalent bonds were formed between ND and GO as confirmed by XPS. The epoxy composites were prepared by the solution casting method and it was found that the flexural properties and fracture toughness of the composites were improved significantly as shown in Figure 37a and 37b. The strong covalent bonds between GO and ND improve the dispersion of NDs on GO nanosheets and prevents the GO nanosheets from agglomeration. Most importantly, the NDs play a crack pinning role in the enhancement of fracture toughness due to the formation of interlocking surfaces as shown in Figure 37c and 37d. More energy is required to overcome the locking surfaces for crack propagation and the fracture toughness of the composites is

View Article Online
DOI: 10.1039/D4NR01356E

therefore improved significantly.

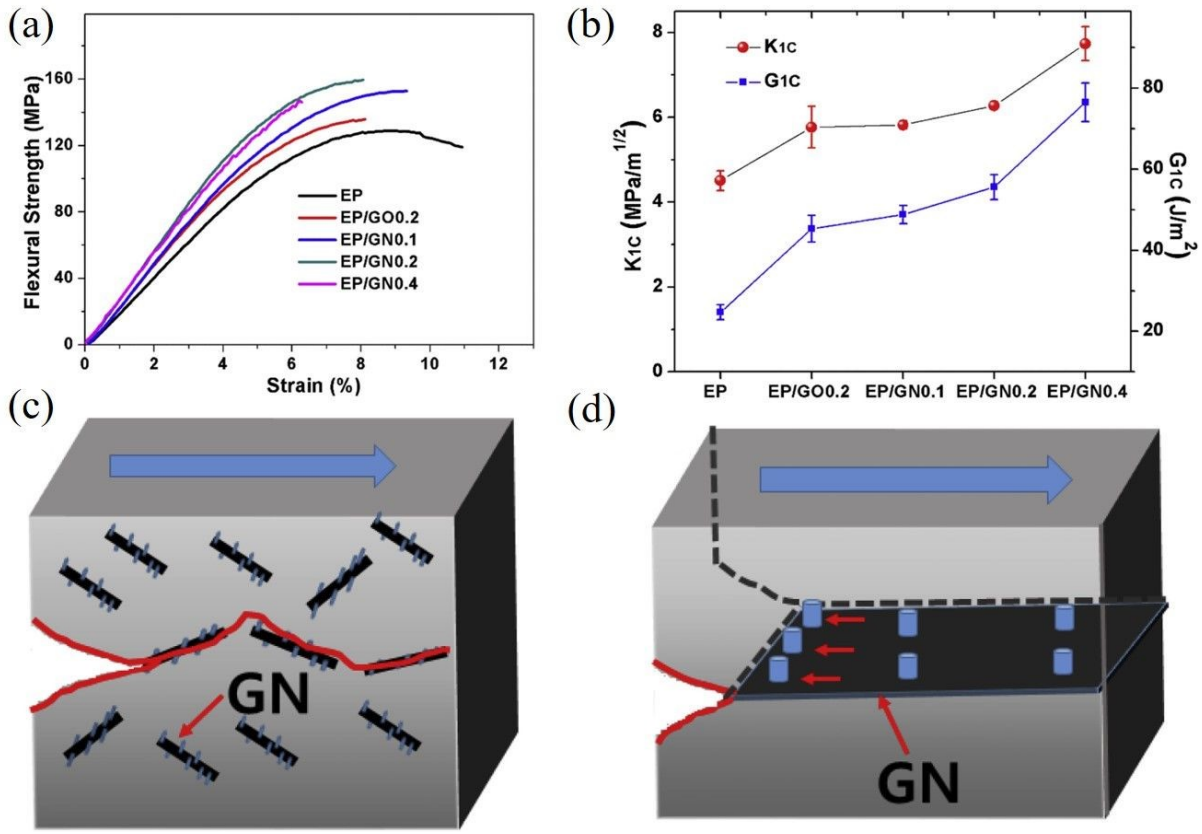

Figure 37. (a) Flexural stress-strain curves of epoxy and its nanocomposites. (b) Variation of fracture toughness of epoxy/GO/ND composites with filler content. (c, d) Crack propagation in epoxy/GO/ND composites. Reproduced with permission from [397]. Copyright 2017 Elsevier.

Table 11. Mechanical properties of hybrid 2D-0D nanocomposites.

Filler 1	Filler 2	Matrix	Processing Method	Matrix modulus (GPa)	Optimum hybrid filler (f1/f2) fraction*	Increase (%)			Ref.
						Young's modulus	Tensile strength	Fracture toughness	
GO	SiO_2	Epoxy	Solution casting	1.36	20, 10, 10 wt%	41	54	89	380
GO	SiO_2	Epoxy	Solution casting	2.64	0.1 wt%	22.86	32.18	–	382
GO	SiO_2	Epoxy	Solution casting	2.133	0.25 wt%	16	59	–	383
GO	ND	Epoxy	Solution casting	–	0.4 wt%	–	–	70	397
GO	LM	Epoxy	Solution casting	–	3.17 wt%	–	–	134	405
GO	Al_2O_3	PU	Solution casting	0.00018	10 wt%	211	41	–	387
rGO	Fe_2O_3	PMMA	In situ polymerization	2	2/2 wt%	137.86	124	–	393

View Article Online
DOI: 10.1039/D4NR01356E

BN	SiO_2	PVA	Vacuum filtration	1.8	15.2 wt%	228	232	–	384
BN	Ag	Epoxy	Solution casting	1.05	20, 5 wt%	33	20	–	391
f-BN	ND	Epoxy	Solution casting	2.3	29 wt%	60	–	–	398
BN	Lignin	PVA	Vacuum filtration	–	2.5 vol%	–	33	–	400
BN	Al_2O_3	PI	Solution casting	1.23	20 wt%	17	–	–	389
MoS_2	ND	PHBV	Solution casting	0.5294	1/2 wt%	113	94	–	399
MoS_2	SiO_2	Epoxy	Solution casting	1.18	3 wt%	46.5	68.7	–	385
MoS_2	CB	SBR	Solution casting	–	3 phr	–	50	–	396
f-MoS_2	SiO_2	PAN	Solution casting	–	2 wt%	–	42	–	386
Ti_3C_2T	ZHS	Epoxy	Solution casting	0.58	2 wt%	312	43	–	406

[a] PHBV, poly(3-hydroxybutyrate-co-3-hydroxyvalerate); PAN, polyacrylonitrile.

[b] LM, liquid metal; ZHS, zinc hydroxystannate.

6. Conclusions and Outlook

The large family of two-dimensional materials displays a range of mechanical properties that can be used to tune the ultimate properties of model, bulk and hybrid polymer nanocomposites. In this present review we have evaluated the possibilities that arise from the use of 2D materials in the mechanical reinforcement of polymers. Despite the possibilities that the inherent properties of 2D materials can offer, the maximisation of their reinforcement efficiency in bulk polymer nanocomposites is still difficult. A number of issues arise from the preparation methods that can either lead to the fabrication of very small aspect ratio flakes, that suffer from interface slippage under stress, or flakes that display high defect densities, that are known to affect the intrinsic properties adversely. Simultaneously, the quality of exfoliated 2D materials that are available commercially is considered to be quite poor, and the batch-to-batch variation is high, identifying the need for the standardization in the fabrication and nomenclature of 2D and graphene-related materials. A step in this direction has been the publication of the ISO terminology for 2D materials (ISO/TS 80004-13:2017).

With regards to model "sandwich" composites, it has been shown that the increase in the number of graphene layers leads to a reduction of the reinforcing efficiency of the material, since the interlayer van der Waals interactions are weak. For certain 2D materials, however, such as boron nitride and

View Article Online
DOI: 10.1039/D4NR01356E

molybdenum disulphide the strength and modulus of the nanoplatelets does not decrease with increasing layer number due to large positive sliding energies. If such materials can be produced in bulk quantities with large lateral dimensions, they might be considered to be promising alternatives to multilayer graphene in bulk polymer nanocomposites, while offering other multifunctional properties such as electrical insulation. Similarly, MXenes are a very interesting family of 2D materials that show good potential for polymer reinforcement as a result of their surface termination with various functional groups and their hydrophilic nature which contribute to a homogeneous dispersion and strong polymer/filler interfaces. Nevertheless, the use of harsh chemicals for the etching process during the production of MXenes raises concerns regarding safety and environmental impact and as a result more sustainable and less hazardous methods need to be developed for MXene synthesis to mitigate these issues.

We evaluated the use of Raman and photoluminescence spectroscopies for the study of the mechanical properties of 2D materials on the nanoscale, highlighting once again the importance of these particular techniques in the field. It should be also noted that classical micromechanical theories such as the shear lag theory predict the optimal reinforcement by using two-dimensional nanoscale specimens (model nanocomposites), under an assumption that there is no interfacial slippage. Under this scenario, the mechanical properties of bulk polymer nanocomposites can be very effectively modelled using composite micromechanics.

The translation of the impressive intrinsic properties of 2D materials from model nanocomposites to bulk nanocomposites presents a number of challenges. The presence of defects arising from bulk exfoliation methods such as liquid-phase exfoliation or electrochemical exfoliation, limit the mechanical properties of the nanoplatelets. Similarly, wrinkles on the surface of the 2D nanoplatelets or loops/folds that are commonly present as a result of the high shear stresses developed during processing limit the effective aspect ratio of the flakes. Additionally, a homogeneous distribution of the 2D nanoplatelets is of utmost importance in order to maximise the mechanical performance of the

View Article Online
DOI: 10.1039/D4NR01356E

nanocomposites. Finally, the development of a strong filler/matrix interface is a critical parameter in nanocomposites and further research into the easy functionalization of flakes for enhancing the interactions between the components of the system needs to be performed. Nevertheless, 2D materials are still more effective than their 1D counterparts when oriented randomly (this is common during standard industrial mixing processes). The effective modulus of 2D materials drops to less than half when they are randomly oriented, compared to tubular or fibre-shaped materials where the effective modulus is reduced by a factor of 5. Quite importantly, polymers reinforced with 2D materials can be processed much easier than those with nanotubes or nanofibers, as they do not form highly complex entanglements that are very difficult to break down and increase the viscosity significantly.

The advances in research upon 2D materials have opened up numerous prospects for the development of commercially-available polymer nanocomposites reinforced with 2D materials; the precise engineering of the structural characteristics, the aspect ratios and the surface chemistry of 2D materials along with progress in polymer processing hold the key for the further advances in this field.

References

1. K. S. Novoselov, A. K. Geim, S. V. Morozov, D. Jiang, Y. Zhang, S. V. Dubonos, I. V. Grigorieva and A. A. Firsov, *Science*, 2004, **306**, 666-669.
2. K. S. Novoselov, V. I. Fal'ko, L. Colombo, P. R. Gellert, M. G. Schwab and K. Kim, *Nature*, 2012, **490**, 192-200.
3. C. Si, Z. Sun and F. Liu, *Nanoscale*, 2016, **8**, 3207-3217.
4. W. Choi, N. Choudhary, G. H. Han, J. Park, D. Akinwande and Y. H. Lee, *Mater. Today*, 2017, **20**, 116-130.
5. J. Halim, S. Kota, M. R. Lukatskaya, M. Naguib, M. Q. Zhao, E. J. Moon, J. Pitock, J. Nanda, S. J. May, Y. Gogotsi and M. W. Barsoum, *Adv. Funct. Mater.*, 2016, **26**, 3118-3127.
6. A. Castellanos-Gomez, *J. Phys. Chem. Lett.*, 2015, **6**, 4280-4291.
7. C. L. Tan, X. H. Cao, X. J. Wu, Q. Y. He, J. Yang, X. Zhang, J. Z. Chen, W. Zhao, S. K. Han, G. H. Nam, M. Sindoro and H. Zhang, *Chem. Rev.*, 2017, **117**, 6225-6331.
8. A. A. Balandin, S. Ghosh, W. Z. Bao, I. Calizo, D. Teweldebrhan, F. Miao and C. N. Lau, *Nano Lett.*, 2008, **8**, 902-907.
9. K. S. Novoselov, A. K. Geim, S. V. Morozov, D. Jiang, M. I. Katsnelson, I. V. Grigorieva, S. V. Dubonos and A. A. Firsov, *Nature*, 2005, **438**, 197-200.
10. V. Palermo, I. A. Kinloch, S. Ligi and N. M. Pugno, *Adv. Mater.*, 2016, **28**, 6232-6238.
11. P. W. Liu, A. L. Cottrill, D. Kozawa, V. B. Koman, D. Parviz, A. T. Liu, J. F. Yang, T. Q. Tran, M. H. Wong, S. Wang and M. S. Strano, *Nano Today*, 2018, **21**, 18-40.

12. M. Dong, H. Zhang, L. Tzounis, G. Santagiuliana, E. Bilotti and D. G. Papageorgiou, *Carbon*, 2021, **185**, 57-81.

13. D. Akinwande, C. J. Brennan, J. S. Bunch, P. Egberts, J. R. Felts, H. J. Gao, R. Huang, J. S. Kim, T. Li, Y. Li, K. M. Liechti, N. S. Lu, H. S. Park, E. J. Reed, P. Wang, B. I. Yakobson, T. Zhang, Y. W. Zhang, Y. Zhou and Y. Zhu, *Extreme Mech. Lett.*, 2017, **13**, 42-77.

14. C. Androulidakis, K. H. Zhang, M. Robertson and S. Tawfick, *2D Mater.*, 2018, **5**, 28.

15. C. Lee, X. D. Wei, J. W. Kysar and J. Hone, *Science*, 2008, **321**, 385-388.

16. D. G. Papageorgiou, I. A. Kinloch and R. J. Young, *Prog. Mater. Sci.*, 2017, **90**, 75-127.

17. A. Falin, Q. R. Cai, E. J. G. Santos, D. Scullion, D. Qian, R. Zhang, Z. Yang, S. M. Huang, K. Watanabe, T. Taniguchi, M. R. Barnett, Y. Chen, R. S. Ruoff and L. H. Li, *Nat. Commun.*, 2017, **8**, 9.

18. S. Bertolazzi, J. Brivio and A. Kis, *ACS Nano*, 2011, **5**, 9703-9709.

19. L. Gong, I. A. Kinloch, R. J. Young, I. Riaz, R. Jalil and K. S. Novoselov, *Adv. Mater.*, 2010, **22**, 2694-2697.

20. T. Jiang, R. Huang and Y. Zhu, *Adv. Funct. Mater.*, 2014, **24**, 396-402.

21. X. K. Cai, Y. T. Luo, B. Liu and H. M. Cheng, *Chem. Soc. Rev.*, 2018, **47**, 6224-6266.

22. R. J. Young, I. A. Kinloch, L. Gong and K. S. Novoselov, *Compos. Sci. Technol.*, 2012, **72**, 1459-1476.

23. D. G. Papageorgiou, Z. L. Li, M. F. Liu, I. A. Kinloch and R. J. Young, *Nanoscale*, 2020, **12**, 2228-2267.

24. H. Zhan, D. Guo and G. X. Xie, *Nanoscale*, 2019, **11**, 13181-13212.

25. M. Yi and Z. G. Shen, *J. Mater. Chem. A*, 2015, **3**, 11700-11715.

26. Y. Huang, E. Sutter, N. N. Shi, J. B. Zheng, T. Z. Yang, D. Englund, H. J. Gao and P. Sutter, *ACS Nano*, 2015, **9**, 10612-10620.

27. Y. Hernandez, V. Nicolosi, M. Lotya, F. M. Blighe, Z. Y. Sun, S. De, I. T. McGovern, B. Holland, M. Byrne, Y. K. Gun'ko, J. J. Boland, P. Niraj, G. Duesberg, S. Krishnamurthy, R. Goodhue, J. Hutchison, V. Scardaci, A. C. Ferrari and J. N. Coleman, *Nat. Nanotechnol.*, 2008, **3**, 563-568.

28. Z. Li, R. J. Young, C. Backes, W. Zhao, X. Zhang, A. A. Zhukov, E. Tillotson, A. P. Conlan, F. Ding, S. J. Haigh, K. S. Novoselov and J. N. Coleman, *ACS Nano*, 2020, **14**, 10976-10985.

29. A. Ciesielski and P. Samori, *Chem. Soc. Rev.*, 2014, **43**, 381-398.

30. J. N. Coleman, M. Lotya, A. O'Neill, S. D. Bergin, P. J. King, U. Khan, K. Young, A. Gaucher, S. De, R. J. Smith, I. V. Shvets, S. K. Arora, G. Stanton, H. Y. Kim, K. Lee, G. T. Kim, G. S. Duesberg, T. Hallam, J. J. Boland, J. J. Wang, J. F. Donegan, J. C. Grunlan, G. Moriarty, A. Shmeliov, R. J. Nicholls, J. M. Perkins, E. M. Grieveson, K. Theuwissen, D. W. McComb, P. D. Nellist and V. Nicolosi, *Science*, 2011, **331**, 568-571.

31. K. R. Paton, E. Varrla, C. Backes, R. J. Smith, U. Khan, A. O'Neill, C. Boland, M. Lotya, O. M. Istrate, P. King, T. Higgins, S. Barwich, P. May, P. Puczkarski, I. Ahmed, M. Moebius, H. Pettersson, E. Long, J. Coelho, S. E. O'Brien, E. K. McGuire, B. M. Sanchez, G. S. Duesberg, N. McEvoy, T. J. Pennycook, C. Downing, A. Crossley, V. Nicolosi and J. N. Coleman, *Nat. Mater.*, 2014, **13**, 624-630.

32. M. Yi and Z. G. Shen, *Carbon*, 2014, **78**, 622-626.

33. W. W. Lei, V. N. Mochalin, D. Liu, S. Qin, Y. Gogotsi and Y. Chen, *Nat. Commun.*, 2015, **6**, 8.

34. J. Zheng, H. Zhang, S. H. Dong, Y. P. Liu, C. T. Nai, H. S. Shin, H. Y. Jeong, B. Liu

View Article Online
DOI: 10.1039/D4NR01356E

and K. P. Loh, *Nat. Commun.*, 2014, **5**, 7.

35. L. Y. Niu, M. J. Li, X. M. Tao, Z. Xie, X. C. Zhou, A. P. A. Raju, R. J. Young and Z. J. Zheng, *Nanoscale*, 2013, **5**, 7202-7208.

36. S. Stankovich, D. A. Dikin, R. D. Piner, K. A. Kohlhaas, A. Kleinhammes, Y. Jia, Y. Wu, S. T. Nguyen and R. S. Ruoff, *Carbon*, 2007, **45**, 1558-1565.

37. M. Naguib, M. Kurtoglu, V. Presser, J. Lu, J. J. Niu, M. Heon, L. Hultman, Y. Gogotsi and M. W. Barsoum, *Adv. Mater.*, 2011, **23**, 4248-4253.

38. Y. Zhang, L. Y. Zhang and C. W. Zhou, *Accounts Chem. Res.*, 2013, **46**, 2329-2339.

39. K. S. Kim, Y. Zhao, H. Jang, S. Y. Lee, J. M. Kim, K. S. Kim, J. H. Ahn, P. Kim, J. Y. Choi and B. H. Hong, *Nature*, 2009, **457**, 706-710.

40. R. Munoz and C. Gomez-Aleixandre, *Chem. Vapor Depos.*, 2013, **19**, 297-322.

41. X. S. Li, W. W. Cai, J. H. An, S. Kim, J. Nah, D. X. Yang, R. Piner, A. Velamakanni, I. Jung, E. Tutuc, S. K. Banerjee, L. Colombo and R. S. Ruoff, *Science*, 2009, **324**, 1312-1314.

42. Y. J. Zhan, Z. Liu, S. Najmaei, P. M. Ajayan and J. Lou, *Small*, 2012, **8**, 966-971.

43. B. Deng, P. C. Hsu, G. C. Chen, B. N. Chandrashekar, L. Liao, Z. Ayitimuda, J. X. Wu, Y. F. Guo, L. Lin, Y. Zhou, M. Aisijiang, Q. Xie, Y. Cui, Z. F. Liu and H. L. Peng, *Nano Lett.*, 2015, **15**, 4206-4213.

44. E. Schwerin, *ZAMM* 1929, **9**, 482-483.

45. C. R. Jin, A. Davoodabadi, J. L. Li, Y. L. Wang and T. Singler, *J. Mech. Phys. Solids*, 2017, **100**, 85-102.

46. J. Han, N. M. Pugno and S. Ryu, *Nanoscale*, 2015, **7**, 15672-15679.

47. A. Lipatov, H. D. Lu, M. Alhabeb, B. Anasori, A. Gruverman, Y. Gogotsi and A. Sinitskii, *Sci. Adv.*, 2018, **4**, 7.

48. K. Cao, S. Feng, Y. Han, L. Gao, T. Hue Ly, Z. Xu and Y. Lu, *Nat. Commun.*, 2020, **11**, 284.

49. C. Rong, T. Su, Z. Li, T. Chu, M. Zhu, Y. Yan, B. Zhang and F.-Z. Xuan, *Nat. Commun.*, 2024, **15**, 1566.

50. J. Varillas, J. Lukeš, A. Manikas, J. Maňák, J. Dluhoš, Z. Melníková, M. Kalbáč, C. Galiotis and O. Frank, *Int. J. Mech. Sci.*, 2024, **273**, 109208.

51. C. M. Stafford, C. Harrison, K. L. Beers, A. Karim, E. J. Amis, M. R. Vanlandingham, H. C. Kim, W. Volksen, R. D. Miller and E. E. Simonyi, *Nat. Mater.*, 2004, **3**, 545-550.

52. A. L. Volynskii, S. Bazhenov, O. V. Lebedeva and N. F. Bakeev, *J. Mater. Sci.*, 2000, **35**, 547-554.

53. M. Dong, Y. Sun, D. J. Dunstan and D. G. Papageorgiou, *Nanoscale*, 2022, **14**, 7872-7880.

54. N. Iguiniz, R. Frisenda, R. Bratschitsch and A. Castellanos-Gomez, *Adv. Mater.*, 2019, **31**, 6.

55. C. Di Giorgio, E. Blundo, G. Pettinari, M. Felici, F. Bobba and A. Polimeni, *Adv. Mater. Interfaces*, 2022, **9**, 2102220.

56. G. Wang, H. Hou, Y. Yan, R. Jagatramka, A. Shirsalimian, Y. Wang, B. Li, M. Daly and C. Cao, *International Journal of Extreme Manufacturing*, 2023, **5**, 032002.

57. G. H. Lee, R. C. Cooper, S. J. An, S. Lee, A. van der Zande, N. Petrone, A. G. Hammerherg, C. Lee, B. Crawford, W. Oliver, J. W. Kysar and J. Hone, *Science*, 2013, **340**, 1073-1076.

58. X. D. Wei, Z. X. Meng, L. Ruiz, W. J. Xia, C. Lee, J. W. Kysar, J. C. Hone, S. Keten and H. D. Espinosa, *ACS Nano*, 2016, **10**, 1820-1828.

59. J. W. Suk, R. D. Piner, J. H. An and R. S. Ruoff, *ACS Nano*, 2010, **4**, 6557-6564.

60. A. Castellanos-Gomez, M. Poot, G. A. Steele, H. S. J. van der Zant, N. Agrait and G. Rubio-Bollinger, *Adv. Mater.*, 2012, **24**, 772-775.

61. K. Liu, Q. M. Yan, M. Chen, W. Fan, Y. H. Sun, J. Suh, D. Y. Fu, S. Lee, J. Zhou, S. Tongay, J. Ji, J. B. Neaton and J. Q. Wu, *Nano Lett.*, 2014, **14**, 5097-5103.

62. Y. C. Yang, X. Li, M. R. Wen, E. Hacopian, W. B. Chen, Y. J. Gong, J. Zhang, B. Li, W. Zhou, P. M. Ajayan, Q. Chen, T. Zhu and J. Lou, *Adv. Mater.*, 2017, **29**, 7.

63. R. Zhang, V. Koutsos and R. Cheung, *Appl. Phys. Lett.*, 2016, **108**, 5.

64. Y. F. Sun, J. B. Pan, Z. T. Zhang, K. N. Zhang, J. Liang, W. J. Wang, Z. Q. Yuan, Y. K. Hao, B. L. Wang, J. W. Wang, Y. Wu, J. Y. Zheng, L. Y. Jiao, S. Y. Zhou, K. H. Liu, C. Cheng, W. H. Duan, Y. Xu, Q. M. Yan and K. Liu, *Nano Lett.*, 2019, **19**, 761-769.

65. J. W. Li, N. V. Medhekar and V. B. Shenoy, *J. Phys. Chem. C*, 2013, **117**, 15842-15848.

66. V. N. Borysiuk, V. N. Mochalin and Y. Gogotsi, *Nanotechnology*, 2015, **26**, 10.

67. A. Lipatov, M. Alhabeb, H. D. Lu, S. S. Zhao, M. J. Loes, N. S. Vorobeva, Y. Dall'Agnese, Y. Gao, A. Gruverman, Y. Gogotsi and A. Sinitskii, *Adv. Electron. Mater.*, 2020, **6**, 10.

68. J. Tao, W. F. Shen, S. Wu, L. Liu, Z. H. Feng, C. Wang, C. G. Hu, P. Yao, H. Zhang, W. Pang, X. X. Duan, J. Liu, C. W. Zhou and D. H. Zhang, *ACS Nano*, 2015, **9**, 11362-11370.

69. H. Chen, P. Huang, D. Guo and G. X. Xie, *J. Phys. Chem. C*, 2016, **120**, 29491-29497.

70. L. Vaquero-Garzon, R. Frisenda and A. Castellanos-Gomez, *Nanoscale*, 2019, **11**, 12080-12086.

71. F. Banhart, J. Kotakoski and A. V. Krasheninnikov, *ACS Nano*, 2011, **5**, 26-41.

72. X. Zhao, D. G. Papageorgiou, L. Y. Zhu, F. Ding and R. J. Young, *Nanoscale*, 2019, **11**, 14339-14353.

73. L. Song, L. J. Ci, H. Lu, P. B. Sorokin, C. H. Jin, J. Ni, A. G. Kvashnin, D. G. Kvashnin, J. Lou, B. I. Yakobson and P. M. Ajayan, *Nano Lett.*, 2010, **10**, 3209-3215.

74. W. J. Chen, X. C. Gui, L. L. Yang, H. Zhu and Z. K. Tang, *Nanoscale Horiz.*, 2019, **4**, 291-320.

75. C. S. Ruiz-Vargas, H. L. L. Zhuang, P. Y. Huang, A. M. van der Zande, S. Garg, P. L. McEuen, D. A. Muller, R. G. Hennig and J. Park, *Nano Lett.*, 2011, **11**, 2259-2263.

76. G. Lopez-Polin, C. Gomez-Navarro, V. Parente, F. Guinea, M. I. Katsnelson, F. Perez-Murano and J. Gomez-Herrero, *Nat. Phys.*, 2015, **11**, 26-31.

77. R. Grantab, V. B. Shenoy and R. S. Ruoff, *Science*, 2010, **330**, 946-948.

78. R. J. T. Nicholl, H. J. Conley, N. V. Lavrik, I. Vlassiouk, Y. S. Puzyrev, V. P. Sreenivas, S. T. Pantelides and K. I. Bolotin, *Nat. Commun.*, 2015, **6**, 7.

79. G. Lopez-Polin, J. Gomez-Herrero and C. Gomez-Navarro, *Nano Lett.*, 2015, **15**, 2050-2054.

80. R. C. Cooper, C. Lee, C. A. Marianetti, X. D. Wei, J. Hone and J. W. Kysar, *Phys. Rev. B*, 2013, **87**, 11.

81. P. Zhang, L. L. Ma, F. F. Fan, Z. Zeng, C. Peng, P. E. Loya, Z. Liu, Y. J. Gong, J. N. Zhang, X. X. Zhang, P. M. Ajayan, T. Zhu and J. Lou, *Nat. Commun.*, 2014, **5**, 7.

82. S. S. Wang, Z. Qin, G. S. Jung, F. J. Martin-Martinez, K. Zhang, M. J. Buehler and J. H. Warner, *ACS Nano*, 2016, **10**, 9831-9839.

83. A. A. Griffith and G. I. Taylor, 1921, **221**, 163-198.

84. A. J. Kinloch and R. J. Young, *Fracture behaviour of polymers*, Springer Science & Business Media, Dordrecht, 2013.

85. X. Zhao, B. Mao, M. Liu, J. Cao, S. J. Haigh, D. G. Papageorgiou, Z. Li and R. J. Young, *Adv. Funct. Mater.*, 2022, **32**, 2202373.

86. X. L. Wei, S. Xiao, F. X. Li, D. M. Tang, Q. Chen, Y. Bando and D. Golberg, *Nano Lett.*, 2015, **15**, 689-694.

87. G. Jung, Z. Qin and M. J. Buehler, *Extreme Mech. Lett.*, 2015, **2**, 52-59.

88. S. R. Na, X. H. Wang, R. D. Piner, R. Huang, C. G. Willson and K. M. Liechti, *ACS Nano*, 2016, **10**, 9616-9625.

89. Y. C. Yang, Z. G. Song, G. Y. Lu, Q. H. Zhang, B. Y. Zhang, B. Ni, C. Wang, X. Y. Li, L. Gu, X. M. Xie, H. J. Gao and J. Lou, *Nature*, 2021, **594**, 57-61.

90. C. H. Cao, S. Mukherjee, J. Y. Howe, D. D. Perovic, Y. Sun, C. V. Singh and T. Filleter, *Sci. Adv.*, 2018, **4**, 9.

91. M. K. Blees, A. W. Barnard, P. A. Rose, S. P. Roberts, K. L. McGill, P. Y. Huang, A. R. Ruyack, J. W. Kevek, B. Kobrin, D. A. Muller and P. L. McEuen, *Nature*, 2015, **524**, 204-207.

92. R. J. Young and P. A. Lovell, *Introduction to Polymers*, CRC Press, Boca Raton, 2011.

93. H. L. Cox, *British Journal of Applied Physics*, 1952, **3**, 72-79.

94. Z. H. Ni, T. Yu, Y. H. Lu, Y. Y. Wang, Y. P. Feng and Z. X. Shen, *ACS Nano*, 2008, **2**, 2301-2305.

95. T. M. G. Mohiuddin, A. Lombardo, R. R. Nair, A. Bonetti, G. Savini, R. Jalil, N. Bonini, D. M. Basko, C. Galiotis, N. Marzari, K. S. Novoselov, A. K. Geim and A. C. Ferrari, *Phys. Rev. B*, 2009, **79**, 8.

96. M. Y. Huang, H. G. Yan, C. Y. Chen, D. H. Song, T. F. Heinz and J. Hone, *Proc. Natl. Acad. Sci. U. S. A.*, 2009, **106**, 7304-7308.

97. O. Frank, M. Mohr, J. Maultzsch, C. Thomsen, I. Riaz, R. Jalil, K. S. Novoselov, G. Tsoukleri, J. Parthenios, K. Papagelis, L. Kavan and C. Galiotis, *ACS Nano*, 2011, **5**, 2231-2239.

98. D. Yoon, Y. W. Son and H. Cheong, *Phys. Rev. Lett.*, 2011, **106**, 4.

99. I. Polyzos, M. Bianchi, L. Rizzi, E. N. Koukaras, J. Parthenios, K. Papagelis, R. Sordan and C. Galiotis, *Nanoscale*, 2015, **7**, 13033-13042.

100. C. Androulidakis, E. N. Koukaras, M. Poss, K. Papagelis, C. Galiotis and S. Tawfick, *Phys. Rev. B*, 2018, **97**, 6.

101. C. Rice, R. J. Young, R. Zan, U. Bangert, D. Wolverson, T. Georgiou, R. Jalil and K. S. Novoselov, *Phys. Rev. B*, 2013, **87**, 5.

102. Y. L. Wang, C. X. Cong, C. Y. Qiu and T. Yu, *Small*, 2013, **9**, 2857-2861.

103. H. J. Conley, B. Wang, J. I. Ziegler, R. F. Haglund, S. T. Pantelides and K. I. Bolotin, *Nano Lett.*, 2013, **13**, 3626-3630.

104. Z. W. Li, Y. W. Lv, L. W. Ren, J. Li, L. A. Kong, Y. J. Zeng, Q. Y. Tao, R. X. Wu, H. F. Ma, B. Zhao, D. Wang, W. Q. Dang, K. Q. Chen, L. Liao, X. D. Duan, X. F. Duan and Y. Liu, *Nat. Commun.*, 2020, **11**, 8.

105. A. M. Dadgar, D. Scullion, K. Kang, D. Esposito, E. H. Yang, I. P. Herman, M. A. Pimenta, E. J. G. Santos and A. N. Pasupathy, *Chemistry of Materials*, 2018, **30**, 5148-5155.

106. F. Wang, I. A. Kinloch, D. Wolverson, R. Tenne, A. Zak, E. O'Connell, U. Bangert and R. J. Young, *2D Mater.*, 2017, **4**, 14.

107. F. Wang, S. Li, M. A. Bissett, I. A. Kinloch, Z. Li and R. J. Young, *2D Mater.*, 2020, **7**, 045022.

108. M. F. Liu, Y. L. Zhuo, A. Sarycheva, Y. Gogotsi, M. A. Bissett, R. J. Young and I. A. Kinloch, *ACS Appl. Mater. Interfaces*, 2022, **14**, 10681-10690.

109. X. Wang, K. Tantiwanichapan, J. W. Christopher, R. Paiella and A. K. Swan, *Nano Lett.*, 2015, **15**, 5969-5975.

110. H. Yan, M. Zhang, S. Wang, H. Li, S. Kunsági-Máté and S. Yin, *Appl. Surf. Sci.*, 2023, **610**, 155531.

111. Y. Huang and R. J. Young, *Compos. Sci. Technol.*, 1994, **52**, 505-517.

112. R. J. Young, L. Gong, I. A. Kinloch, I. Riaz, R. Jalil and K. S. Novoselov, *ACS Nano*, 2011, **5**, 3079-3084.

113. G. Anagnostopoulos, C. Androulidakis, E. N. Koukaras, G. Tsoukleri, I. Polyzos, J. Parthenios, K. Papagelis and C. Galiotis, *ACS Appl. Mater. Interfaces*, 2015, **7**, 4216-4223.

114. Z. Liu, M. Amani, S. Najmaei, Q. Xu, X. L. Zou, W. Zhou, T. Yu, C. Y. Qiu, A. G. Birdwell, F. J. Crowne, R. Vajtai, B. I. Yakobson, Z. H. Xia, M. Dubey, P. M. Ajayan and J. Lou, *Nat. Commun.*, 2014, **5**, 9.

115. M. Dong, R. J. Young, D. J. Dunstan and D. G. Papageorgiou, *Composites Science and Technology*, 2023, **233**, 109892.

116. I. Niehues, A. Blob, T. Stiehm, R. Schmidt, V. Jadrisko, B. Radatovic, D. Capeta, M. Kralj, S. M. de Vasconcellos and R. Bratschitsch, *2D Mater.*, 2018, **5**.

117. A. C. Manikas, M. G. Pastore Carbone, C. R. Woods, Y. Wang, I. Souli, G. Anagnostopoulos, M. Hadjinicolaou, K. S. Novoselov and C. Galiotis, *Nanoscale*, 2019, **11**, 14354-14361.

118. M. G. Pastore Carbone, G. Tsoukleri, A. C. Manikas, E. Makarona, C. Tsamis and C. Galiotis, *J. Compos. Sci.*, 2019, **3**, 42.

119. G. Guo and Y. Zhu, *J. Appl. Mech.*, 2015, **82**, 031005.

120. Z. L. Li, I. A. Kinloch, R. J. Young, K. S. Novoselov, G. Anagnostopoulos, J. Parthenios, C. Galiotis, K. Papagelis, C. Y. Lu and L. Britnell, *ACS Nano*, 2015, **9**, 3917-3925.

121. Z. L. Li, R. J. Young, D. G. Papageorgiou, I. A. Kinloch, X. Zhao, C. Yang and S. J. Hao, *2D Mater.*, 2019, **6**, 11.

122. C. Androulidakis, E. N. Koukaras, J. Rahova, K. Sampathkumar, J. Parthenios, K. Papagelis, O. Frank and C. Galiotis, *ACS Appl. Mater. Interfaces*, 2017, **9**, 26593-26601.

123. J. Yu, S. Kim, E. Ertekin and A. M. van der Zande, *ACS Appl. Mater. Interfaces*, 2020, **12**, 10801-10808.

124. Q. H. Zhang, Z. Y. Chang, G. Z. Xu, Z. Y. Wang, Y. P. Zhang, Z. Q. Xu, S. J. Chen, Q. L. Bao, J. Z. Liu, Y. W. Mai, W. H. Duan, M. S. Fuhrer and C. X. Zheng, *Adv. Funct. Mater.*, 2016, **26**, 8707-8714.

125. G. R. Wang, Z. H. Dai, L. Q. Liu, H. Hu, Q. Dai and Z. Zhang, *ACS Appl. Mater. Interfaces*, 2016, **8**, 22554-22562.

126. F. Najafi, G. Wang, S. Mukherjee, T. Cui, T. Filleter and C. V. Singh, *Compos. Sci. Technol.*, 2020, **194**, 108140.

127. Y. Y. Cui, G. R. Wang, W. X. Wang, X. W. Cui, W. L. Dong, C. Y. Wang, M. H. Jin, T. He, Z. Zhang and L. Q. Liu, *Compos. Sci. Technol.*, 2022, **225**, 8.

128. L. Gong, R. J. Young, I. A. Kinloch, I. Riaz, R. Jalil and K. S. Novoselov, *ACS Nano*, 2012, **6**, 2086-2095.

129. C. Androulidakis, E. N. Koukaras, G. Paterakis, G. Trakakis and C. Galiotis, *Nat. Commun.*, 2020, **11**, 1595.

130. A. P. Sgouros, C. Androulidakis, G. Tsoukleri, G. Kalosakas, N. Delikoukos, S. Signetti, N. M. Pugno, J. Parthenios, C. Galiotis and K. Papagelis, *ACS Appl. Mater. Interfaces*, 2021, **13**, 4473-4484.

131. W. M. Wang, Z. L. Li, A. J. Marsden, M. A. Bissett and R. J. Young, *2D Mater.*, 2021, **8**, 8.

132. Y. Y. Li, Z. X. Hu, S. H. Lin, S. K. Lai, W. Ji and S. P. Lau, *Adv. Funct. Mater.*, 2017, **27**, 9.

133. C. Androulidakis, D. Sourlantzis, E. N. Koukaras, A. C. Manikas and C. Galiotis, *Nanoscale Adv.*, 2019, **1**, 4972-4980.

134. I. Vlassiouk, G. Polizos, R. Cooper, I. Ivanov, J. K. Keum, F. Paulauskas, P. Datskos and S. Smirnov, *ACS Appl. Mater. Interfaces*, 2015, **7**, 10702-10709.

135. P. W. Liu, Z. Jin, G. Katsukis, L. W. Drahushuk, S. Shimizu, C. J. Shih, E. D. Wetzel, J. K. Taggart-Scarff, B. Qing, K. J. Van Vliet, R. Li, B. L. Wardle and M. S. Strano, *Science*, 2016, **353**, 364-367.

136. B. Wang, Z. C. Li, C. H. Wang, S. Signetti, B. V. Cunning, X. Z. Wu, Y. Huang, Y. Jiang, H. F. Shi, S. Ryu, N. M. Pugno and R. S. Ruoff, *Adv. Mater.*, 2018, **30**, 10.

137. C. Pavlou, M. G. P. Carbone, A. C. Manikas, G. Trakakis, C. Koral, G. Papari, A. Andreone and C. Galiotis, *Nat. Commun.*, 2021, **12**, 9.

138. S.-I. Kim, J.-Y. Moon, S.-K. Hyeong, S. Ghods, J.-S. Kim, J.-H. Choi, D. S. Park, S. Bae, S. H. Cho, S.-K. Lee and J.-H. Lee, *Nat. Commun.*, 2024, **15**, 2172.

139. A. Kundu, W. K. Seong, S. K. Jalali, N. M. Pugno and R. S. Ruoff, *arXiv preprint arXiv:2405.11888*, 2024.

140. K. S. Hu, D. D. Kulkarni, I. Choi and V. V. Tsukruk, *Prog. Polym. Sci.*, 2014, **39**, 1934-1972.

141. S. Thakur, P. Bandyopadhyay, S. H. Kim, N. H. Kim and J. H. Lee, *Compos. Pt. A-Appl. Sci. Manuf.*, 2018, **110**, 284-293.

142. C. B. Hatter, J. Shah, B. Anasori and Y. Gogotsi, *Compos. Pt. B-Eng.*, 2020, **182**, 7.

143. O. Eksik, J. Gao, S. A. Shojaee, A. Thomas, P. Chow, S. F. Bartolucci, D. A. Lucca and N. Koratkar, *ACS Nano*, 2014, **8**, 5282-5289.

144. Y. Li, H. Zhang, H. Porwal, Z. Huang, E. Bilotti and T. Peijs, *Compos. Part A: Appl. Sci. Manuf.*, 2017, **95**, 229-236.

145. Y. Li, H. Zhang, M. Crespo, H. Porwal, O. Picot, G. Santagiuliana, Z. H. Huang, E. Barbieri, N. M. Pugno, T. Peijs and E. Bilotti, *ACS Appl. Mater. Interfaces*, 2016, **8**, 24112-24122.

146. H. Ribeiro, J. P. C. Trigueiro, W. M. Silva, C. F. Woellner, P. S. Owuor, A. Cristian Chipara, M. C. Lopes, C. S. Tiwary, J. J. Pedrotti, R. Villegas Salvatierra, J. M. Tour, N. Chopra, I. N. Odeh, G. G. Silva and P. M. Ajayan, *ACS Appl. Mater. Interfaces*, 2019, **11**, 24485-24492.

147. M. Dong, O. Tomes, A. Soul, Y. Hu, E. Bilotti, H. Zhang and D. G. Papageorgiou, *ACS Appl. Nano Mater.*, 2024, **7**, 3314-3325.

148. D. G. Papageorgiou, Z. Terzopoulou, A. Fina, F. Cuttica, G. Z. Papageorgiou, D. N. Bikiaris, K. Chrissafis, R. J. Young and I. A. Kinloch, *Compos. Sci. Technol.*, 2018, **156**, 95-102.

149. X. X. Sheng, Y. F. Zhao, L. Zhang and X. Lu, *Compos. Sci. Technol.*, 2019, **181**, 8.

150. M. F. Liu, S. H. Li, I. A. Kinloch, R. J. Young and D. G. Papageorgiou, *2D Mater.*, 2020, **7**, 025031.

151. M. F. Liu, I. A. Kinloch, R. J. Young and D. G. Papageorgiou, *Nanoscale*, 2020, **12**, 3377-3386.

152. M. F. Liu, D. G. Papageorgiou, S. H. Li, K. L. Lin, I. A. Kinloch and R. J. Young, *Compos. Pt. A-Appl. Sci. Manuf.*, 2018, **110**, 84-92.

153. M. F. Liu, I. A. Kinloch, R. J. Young and D. G. Papageorgiou, *Compos. Pt. B-Eng.*, 2019, **178**, 8.

154. C. Vilaverde, R. M. Santos, M. C. Paiva and J. A. Covas, *Compos. Pt. A-Appl. Sci. Manuf.*, 2015, **78**, 143-151.

155. G. Santagiuliana, O. T. Picot, M. Crespo, H. Porwal, H. Zhang, Y. Li, L. Rubini, S. Colonna, A. Fina, E. Barbieri, A. B. Spoelstra, G. Mirabello, J. P. Patterson, L. Botto, N. M. Pugno, T. Peijs and E. Bilotti, *ACS Nano*, 2018, **12**, 9040-9050.

156. H. W. Wei, J. D. Dong, X. J. Fang, W. H. Zheng, Y. T. Sun, Y. Qian, Z. X. Jiang and Y. D. Huang, *Compos. Sci. Technol.*, 2019, **169**, 52-59.

157. Y. Tong, M. He, Y. M. Zhou, X. Zhong, L. D. Fan, T. Y. Huang, Q. Liao and Y. J. Wang, *Appl. Surf. Sci.*, 2018, **434**, 283-293.

158. M. Bhattacharya, *Materials*, 2016, **9**, 35.

159. G. Decher, *Science*, 1997, **277**, 1232-1237.

160. F. X. Xiao, M. Pagliaro, Y. J. Xu and B. Liu, *Chem. Soc. Rev.*, 2016, **45**, 3088-3121.

View Article Online
DOI: 10.1039/D4NR01356E

161. M. Yang, Y. Hou and N. A. Kotov, *Nano Today*, 2012, **7**, 430-447.
162. H. Chen, M. B. Müller, K. J. Gilmore, G. G. Wallace and D. Li, *Adv. Mater.*, 2008, **20**, 3557-3561.
163. F. M. Xiang, D. Parviz, T. M. Givens, P. Tzeng, E. M. Davis, C. M. Stafford, M. J. Green and J. C. Grunlan, *Adv. Funct. Mater.*, 2016, **26**, 2143-2149.
164. C. J. Huang and Q. F. Cheng, *Compos. Sci. Technol.*, 2017, **150**, 141-166.
165. K. W. Putz, O. C. Compton, M. J. Palmeri, S. T. Nguyen and L. C. Brinson, *Adv. Funct. Mater.*, 2010, **20**, 3322-3329.
166. G. Marom and H. D. Wagner, *J. Mater. Sci.*, 2017, **52**, 8357-8361.
167. Z. L. Li, R. J. Young, N. R. Wilson, I. A. Kinloch, C. Valles and Z. Li, *Compos. Sci. Technol.*, 2016, **123**, 125-133.
168. Z. L. Li, R. J. Young, I. A. Kinloch, N. R. Wilson, A. J. Marsden and A. P. A. Raju, *Carbon*, 2015, **88**, 215-224.
169. M. Dong, Y. Hu, H. Zhang, E. Bilotti, N. Pugno, D. Dunstan and D. G. Papageorgiou, *JCOMC*, 2024, **13**, 100427.
170. Z. L. Li, J. W. Chu, C. Yang, S. J. Hao, M. A. Bissett, I. A. Kinloch and R. J. Youn, *Compos. Sci. Technol.*, 2018, **163**, 116-122.
171. R. J. Young, M. F. Liu, I. A. Kinloch, S. H. Li, X. Zhao, C. Valles and D. G. Papageorgiou, *Compos. Sci. Technol.*, 2018, **154**, 110-116.
172. J. C. H. Affdl and J. L. Kardos, 1976, **16**, 344-352.
173. J. J. Liang, Y. Huang, L. Zhang, Y. Wang, Y. F. Ma, T. Y. Guo and Y. S. Chen, *Adv. Funct. Mater.*, 2009, **19**, 2297-2302.
174. C. Vallés, I. A. Kinloch, R. J. Young, N. R. Wilson and J. P. Rourke, *Compos. Sci. Technol.*, 2013, **88**, 158-164.
175. J. C. Wang, X. B. Wang, C. H. Xu, M. Zhang and X. P. Shang, *Polym. Int.*, 2011, **60**, 816-822.
176. X. Mi, N. Liang, H. Xu, J. Wu, Y. Jiang, B. Nie and D. Zhang, *Prog. Mater. Sci.*, 2022, **130**, 100977.
177. M. Y. Khalid, A. Kamal, A. Otabil, O. Mamoun and K. Liao, *Chem. Eng. J. Adv.*, 2023, **16**, 100537.
178. L.-C. Tang, Y.-J. Wan, D. Yan, Y.-B. Pei, L. Zhao, Y.-B. Li, L.-B. Wu, J.-X. Jiang and G.-Q. Lai, *Carbon*, 2013, **60**, 16-27.
179. F. Z. Wang, L. T. Drzal, Y. Qin and Z. X. Huang, *Compos. Pt. A-Appl. Sci. Manuf.*, 2016, **87**, 10-22.
180. Y. Q. Li, T. Yu, T. Y. Yang, L. X. Zheng and K. Liao, *Adv. Mater.*, 2012, **24**, 3426-3431.
181. N. F. Zhao, M. Yang, Q. Zhao, W. W. Gao, T. Xie and H. Bai, *ACS Nano*, 2017, **11**, 4777-4784.
182. L. X. Gong, Y. B. Pei, Q. Y. Han, L. Zhao, L. B. Wu, J. X. Jiang and L. C. Tang, *Compos. Sci. Technol.*, 2016, **134**, 144-152.
183. C. Valles, D. G. Papageorgiou, F. Lin, Z. L. Li, B. Spencer, R. J. Young and I. A. Kinloch, *Carbon*, 2020, **157**, 750-760.
184. D. R. Bortz, E. G. Heras and I. Martin-Gullon, *Macromolecules*, 2012, **45**, 238-245.
185. M. Huskić, S. Bolka, A. Vesel, M. Mozetič, A. Anžlovar, A. Vizintin and E. Žagar, *Eur. Polym. J.*, 2018, **101**, 211-217.
186. R. Aradhana, S. Mohanty and S. K. Nayak, *Polymer*, 2018, **141**, 109-123.
187. W. Zheng, W. G. Chen, Q. Zhao, S. X. Ren and Y. Q. Fu, *Polymer*, 2019, **163**, 171-177.
188. C. J. Huang, J. S. Peng, S. J. Wan, Y. Du, S. X. Dou, H. D. Wagner, A. P. Tomsia, L. Jiang and Q. F. Cheng, *Angew. Chem. Int. Edit.*, 2019, **58**, 7636-7640.

189. J. Cha, J. Kim, S. Ryu and S. H. Hong, *Compos. Pt. B-Eng.*, 2019, **162**, 283-288.
190. F. Cilento, A. Martone, M. G. Pastore Carbone, C. Galiotis and M. Giordano, *Compos. Sci. Technol.*, 2021, **211**, 108873.
191. J. Guest, I. A. Kinloch and R. J. Young, *J. Mater. Sci.*, 2023, **58**, 9473-9485.
192. Y. Xu, W. Hong, H. Bai, C. Li and G. Shi, *Carbon*, 2009, **47**, 3538-3543.
193. S. Lee, J.-U. Jin, J. R. Hahn, S. Ryu and N.-H. You, *Compos. B: Eng.*, 2024, **271**, 111142.
194. X. Zhao, Q. H. Zhang, D. J. Chen and P. Lu, *Macromolecules*, 2010, **43**, 2357-2363.
195. X. D. Wang, X. H. Liu, H. Y. Yuan, H. Liu, C. T. Liu, T. X. Li, C. Yan, X. R. Yan, C. Y. Shen and Z. H. Guo, *Mater. Des.*, 2018, **139**, 372-379.
196. L. Zhang, Y. Li, H. Wang, Y. Qiao, J. Chen and S. Cao, *Chem. Eng. J.*, 2015, **264**, 538-546.
197. M. Fang, K. G. Wang, H. B. Lu, Y. L. Yang and S. Nutt, *J. Mater. Chem.*, 2009, **19**, 7098-7105.
198. S. S. Rahman, M. Arshad, M. Zubair, M. Ghasri-Khouzani, A. Qureshi and A. Ullah, *Mater. Today Commun.*, 2020, **25**, 101633.
199. S. Vadukumpully, J. Paul, N. Mahanta and S. Valiyaveettil, *Carbon*, 2011, **49**, 198-205.
200. P. G. Song, Z. H. Cao, Y. Z. Cai, L. P. Zhao, Z. P. Fang and S. Y. Fu, *Polymer*, 2011, **52**, 4001-4010.
201. O.-K. Park, J.-Y. Hwang, M. Goh, J. H. Lee, B.-C. Ku and N.-H. You, *Macromolecules*, 2013, **46**, 3505-3511.
202. C. Min, Z. He, H. Liang, D. Liu, C. Dong, H. Song and Y. Huang, *Polym. Compos.*, 2020, **41**, 1624-1635.
203. M. El Achaby, F. Z. Arrakhiz, S. Vaudreuil, E. M. Essassi and A. Qaiss, *Appl. Surf. Sci.*, 2012, **258**, 7668-7677.
204. X. Yang, Y. Tu, L. Li, S. Shang and X.-m. Tao, *ACS Appl. Mater. Interfaces*, 2010, **2**, 1707-1713.
205. S. Wan, J. Peng, Y. Li, H. Hu, L. Jiang and Q. Cheng, *ACS Nano*, 2015, **9**, 9830-9836.
206. S. Lin, M. A. S. Anwer, Y. N. Zhou, A. Sinha, L. Carson and H. E. Naguib, *Compos. Pt. B-Eng.*, 2018, **132**, 61-68.
207. J. A. Puertolas, M. Castro, J. A. Morris, R. Rios and A. Anson-Casaos, *Carbon*, 2019, **141**, 107-122.
208. B. Mayoral, E. Harkin-Jones, P. N. Khanam, M. A. AlMaadeed, M. Ouederni, A. R. Hamilton and D. Sun, *RSC Adv.*, 2015, **5**, 52395-52409.
209. K. Hu, M. K. Gupta, D. D. Kulkarni and V. V. Tsukruk, *Adv. Mater.*, 2013, **25**, 2301-2307.
210. Y. Yang, C.-L. Luo, X.-D. Chen and M. Wang, *Compos. Sci. Technol.*, 2023, **233**, 109913.
211. S. J. Lee, J. Baek and I.-Y. Jeon, *Polymer*, 2024, **294**, 126727.
212. M. Yan, X. Chen, Y. Xu, Y. Pan, J. Li, J. Li, T. Wu, H. Zheng, X. Chen and J. He, *Compos. Commun.*, 2023, **37**, 101428.
213. C. Zhi, Y. Bando, C. Tang, H. Kuwahara and D. Golberg, *Adv. Mater.*, 2009, **21**, 2889-2893.
214. Q. H. Weng, X. B. Wang, X. Wang, Y. Bando and D. Golberg, *Chem. Soc. Rev.*, 2016, **45**, 3989-4012.
215. D. Lee, S. H. Song, J. Hwang, S. H. Jin, K. H. Park, B. H. Kim, S. H. Hong and S. Jeon, *Small*, 2013, **9**, 2602-2610.
216. H. C. Wu and M. R. Kessler, *ACS Appl. Mater. Interfaces*, 2015, **7**, 5915-5926.

217. T. Sainsbury, A. Satti, P. May, Z. M. Wang, I. McGovern, Y. K. Gun'ko and J. Coleman, *J. Am. Chem. Soc.*, 2012, **134**, 18758-18771.

218. Z. Liu, J. H. Li and X. H. Liu, *ACS Appl. Mater. Interfaces*, 2020, **12**, 6503-6515.

219. J. T. Hu, Y. Huang, X. L. Zeng, Q. Li, L. L. Ren, R. Sun, J. B. Xu and C. P. Wong, *Compos. Sci. Technol.*, 2018, **160**, 127-137.

220. Z. Y. Lin, Y. Liu, S. Raghavan, K. S. Moon, S. K. Sitaraman and C. P. Wong, *ACS Appl. Mater. Interfaces*, 2013, **5**, 7633-7640.

221. M. Kiran, K. Raidongia, U. Ramamurty and C. N. R. Rao, *Scr. Mater.*, 2011, **64**, 592-595.

222. Z. Cui, A. P. Martinez and D. H. Adamson, *Nanoscale*, 2015, **7**, 10193-10197.

223. S. Han, Q. Meng, Z. Qiu, A. Osman, R. Cai, Y. Yu, T. Liu and S. Araby, *Polymer*, 2019, **184**, 121884.

224. H. Wang, R. Lu, L. Li, C. Liang, J. Yan, R. Liang, G. Sun, L. Jiang and Q. Cheng, *Nano Res.*, 2023, DOI: 10.1007/s12274-023-6101-4, 1-9.

225. U. Khan, P. May, A. O'Neill, A. P. Bell, E. Boussac, A. Martin, J. Semple and J. N. Coleman, *Nanoscale*, 2013, **5**, 581-587.

226. W. M. Wang, Z. L. Li, A. J. Marsden, M. A. Bissett and R. J. Young, *Compos. Sci. Technol.*, 2022, **218**, 8.

227. J. Zhang, X. N. Wang, C. P. Yu, Q. L. Li, Z. Li, C. W. Li, H. F. Lu, Q. C. Zhang, J. X. Zhao, M. Hu and Y. G. Yao, *Compos. Sci. Technol.*, 2017, **149**, 41-47.

228. W. Cai, D. C. Zhang, B. B. Wang, Y. Q. Shi, Y. Pan, J. L. Wang, W. Z. Hu and Y. Hu, *Compos. Sci. Technol.*, 2018, **168**, 74-80.

229. J. Yang, C. Cao, W. Qiao, J. Qiao, H. Gao, W. Bai, Z. Li, P. Wang, C. Tang and Y. Xue, *ACS Appl. Nano Mater.*, 2022, **5**, 15600-15610.

230. R. Jan, P. May, A. P. Bell, A. Habib, U. Khan and J. N. Coleman, *Nanoscale*, 2014, **6**, 4889-4895.

231. S. U. Rehman, S. Javaid, M. Shahid, N. M. Ahmad, B. Rashid, C. R. Szczepanski and A. Shahzad, *Journal*, 2023, **15**, 235.

232. A. Chaurasia, A. Verma, A. Parashar and R. S. Mulik, *J. Phys. Chem. C*, 2019, **123**, 20059-20070.

233. N. Tajaddod, K. Song, E. C. Green, Y. Y. Zhang and M. L. Minus, *Macromol. Mater. Eng.*, 2016, **301**, 315-327.

234. J. Zhang, D. Liu, Q. Han, L. Jiang, H. Shao, B. Tang, W. Lei, T. Lin and C. H. Wang, *Compos. Pt. B-Eng.*, 2019, **175**, 107157.

235. D. L. Zhang, J. W. Zha, W. K. Li, C. Q. Li, S. J. Wang, Y. Q. Wen and Z. M. Dang, *Compos. Sci. Technol.*, 2018, **156**, 1-7.

236. Z. Xu, L. Bai, Y. Zhang, J. Cao and J. Zheng, *Compos. Sci. Technol.*, 2023, **240**, 110076.

237. Y. Zhang, Y. Fan, U. Kamran and S.-J. Park, *Compos. Part A: Appl. Sci. Manuf.*, 2022, **156**, 106869.

238. J. You, H. H. Choi, Y. M. Lee, J. Cho, M. Park, S. S. Lee and J. H. Park, *Compos. Pt. B-Eng.*, 2019, **164**, 710-719.

239. Q. Xiao, W. Han, R. Yang, Y. You, R. Wei and X. Liu, *Polym. Compos.*, 2018, **39**, E1598-E1605.

240. L.-H. Zhao, L. Wang, Y.-F. Jin, J.-W. Ren, Z. Wang and L.-C. Jia, *Compos. B: Eng.*, 2022, **229**, 109454.

241. S. Riaz and S. J. Park, *Compos. Pt. A-Appl. Sci. Manuf.*, 2021, **146**, 11.

242. X. M. Feng, W. Y. Xing, H. Y. Yang, B. H. Yuan, L. Song, Y. Hu and K. M. Liew, *ACS Appl. Mater. Interfaces*, 2015, **7**, 13164-13173.

243. P. P. Chen, X. Liang, Y. Xu, Y. F. Zhou and W. Y. Nie, *Appl. Surf. Sci.*, 2018, **440**,

View Article Online
DOI: 10.1039/D4NR01356E

1143-1149.
244. X. Wang, E. N. Kalali and D. Y. Wang, *J. Mater. Chem. A*, 2015, **3**, 24112-24120.
245. S. K. Kim, J. J. Wie, Q. Mahmood and H. S. Park, *Nanoscale*, 2014, **6**, 7430-7435.
246. M. Sahu, L. Narashimhan, O. Prakash and A. M. Raichur, *ACS Appl. Mater. Interfaces*, 2017, **9**, 14347-14357.
247. J. L. Wang, C. Ma, X. W. Mu, W. Cai, L. X. Liu, X. Zhou, W. Z. Hu and Y. Hu, *J. Hazard. Mater.*, 2018, **352**, 36-46.
248. M. Sahu, L. Narasimhan, A. M. Raichur, A. Sover, R. C. Ciobanu, N. Lucanu and M. J. P. Aradoaei, *Polymers*, 2021, **13**, 4440.
249. S.-D. Jiang, G. Tang, Z.-M. Bai, Y.-Y. Wang, Y. Hu and L. Song, *RSC Adv.*, 2014, **4**, 3253-3262.
250. A. O'Neill, U. Khan and J. N. Coleman, *Chem. Mat.*, 2012, **24**, 2414-2421.
251. S. Biccai, C. S. Boland, D. P. O'Driscoll, A. Harvey, C. Gabbett, D. R. O'Suilleabhain, A. J. Griffin, Z. Li, R. J. Young and J. N. Coleman, *ACS Nano*, 2019, **13**, 6845-6855.
252. H. X. Zhang, E. B. Ko, J. H. Park, Y. K. Moon, X. Q. Zhang and K. B. Yoon, *Compos. Pt. A-Appl. Sci. Manuf.*, 2017, **93**, 82-87.
253. H. Zhang, Y. K. Moon, X. Q. Zhang, J. S. Liu, H. X. Zhang and K. B. Yoon, *Eur. Polym. J.*, 2017, **87**, 60-68.
254. H. Zhang, Y. K. Moon, X. Q. Zhang, H. X. Zhang and K. B. Yoon, *RSC Adv.*, 2016, **6**, 112429-112434.
255. C. L. C. Rodriguez, M. A. B. S. Nunes, P. S. Garcia and G. J. M. Fechine, *Polym. Test.*, 2021, **93**, 106882.
256. H. Yuan, X. H. Liu, L. M. Ma, Z. G. Yang, H. G. Wang, J. Q. Wang and S. R. Yang, *Compos. Pt. A-Appl. Sci. Manuf.*, 2017, **95**, 220-228.
257. H. X. Zhang, X. Q. Zhang and K. B. Yoon, *Polymers*, 2017, **9**, 490.
258. X. Wang, W. Y. Xing, X. M. Feng, B. Yu, L. Song, G. H. Yeoh and Y. Hu, *Compos. Sci. Technol.*, 2016, **127**, 142-148.
259. X. M. Feng, X. Wang, W. Y. Xing, K. Q. Zhou, L. Song and Y. Hu, *Compos. Sci. Technol.*, 2014, **93**, 76-82.
260. L. Jiang, H. Xie, Y. Hou, S. Wang, Y. Xia, Y. Li, G.-H. Hu, Q. Yang, C. Xiong and Z. Gao, *Ceram. Int.*, 2019, **45**, 11347-11352.
261. T. Wu, Y. Song, Z. Shi, D. Liu, S. Chen, C. Xiong and Q. Yang, *Nano Energy*, 2021, **80**, 105541.
262. L. Liu, G. Ying, D. Wen, K. Zhang, C. Hu, Y. Zheng, C. Zhang, X. Wang and C. Wang, *Materials & Design*, 2021, **197**, 109276.
263. Z. Ling, C. E. Ren, M. Q. Zhao, J. Yang, J. M. Giammarco, J. S. Qiu, M. W. Barsoum and Y. Gogotsi, *Proc. Natl. Acad. Sci. U. S. A.*, 2014, **111**, 16676-16681.
264. Z. Liu, W. Wang, J. Tan, J. Liu, M. Zhu, B. Zhu and Q. Zhang, *J. Mater. Chem. C*, 2020, **8**, 7170-7180.
265. Z. Liu, W. Wang, J. Liu, B. Zhu, G. Zhang, J. Wang, H. Zhang and Q. Zhang, *Chemical Engineering Journal*, 2022, **430**, 132852.
266. W. T. Cao, F. F. Chen, Y. J. Zhu, Y. G. Zhang, Y. Y. Jiang, M. G. Ma and F. Chen, *ACS Nano*, 2018, **12**, 4583-4593.
267. W. Q. Tian, A. VahidMohammadi, M. S. Reid, Z. Wang, L. Q. Ouyang, J. Erlandsson, T. Pettersson, L. Wagberg, M. Beidaghi and M. M. Hamedi, *Adv. Mater.*, 2019, **31**, 1902977.
268. F. Xie, F. Jia, L. Zhuo, Z. Lu, L. Si, J. Huang, M. Zhang and Q. Ma, *Nanoscale*, 2019, **11**, 23382-23391.
269. C. Weng, T. Xing, H. Jin, G. Wang, Z. Dai, Y. Pei, L. Liu and Z. Zhang, *Compos.*

View Article Online
DOI: 10.1039/D4NR01356E

Part A: Appl. Sci. Manuf., 2020, **135**, 105927.

270. L. Wang, L. X. Chen, P. Song, C. B. Liang, Y. J. Lu, H. Qiu, Y. L. Zhang, J. Kong and J. W. Gu, *Compos. Pt. B-Eng.*, 2019, **171**, 111-118.

271. R. Wazalwar, M. Tripathi and A. M. Raichur, *ACS Appl. Polym. Mater.*, 2022, **4**, 2573-2584.

272. H. Wang, R. Lu, J. Yan, J. Peng, A. P. Tomsia, R. Liang, G. Sun, M. Liu, L. Jiang and Q. Cheng, *Angew. Chem-Int. Edit.*, 2023, **62**, e202216874.

273. K. Wang, L. Shen, Q. Zhu, R. Bo, R. Lu, X. Lu and Z. Fu, *Chem. Eng. J.*, 2023, **452**, 139156.

274. Z. Chi, C. Wang, Y. Dong, Y. Zhou, H. Xu, Z. Islam, C. Qian and Y. Fu, *Compos. Sci. Technol.*, 2022, **225**, 109505.

275. X. Zhang, J. Xu, H. Wang, J. Zhang, H. Yan, B. Pan, J. Zhou and Y. Xie, *Angew. Chem. Int. Ed.*, 2013, **52**, 4361-4365.

276. Y. Yi, S. Feng, Z. Zhou and C. Lu, *Compos. Part A: Appl. Sci. Manuf.*, 2022, **163**, 107232.

277. J. H. Woo, N. H. Kim, S. I. Kim, O.-K. Park and J. H. Lee, *Compos. B: Eng.*, 2020, **199**, 108205.

278. S. Mazhar, A. A. Qarni, Y. Ul Haq, Z. Ul Haq and I. Murtaza, *Ceram. Int.*, 2020, **46**, 12593-12605.

279. Y. Zhang, L. Wang, J. Zhang, P. Song, Z. Xiao, C. Liang, H. Qiu, J. Kong and J. Gu, *Compos. Sci. Technol.*, 2019, **183**, 107833.

280. Z. Zhan, Q. Song, Z. Zhou and C. Lu, *J. Mater. Chem. C*, 2019, **7**, 9820-9829.

281. Y. Xue, J. Feng, S. Huo, P. Song, B. Yu, L. Liu and H. Wang, *Chem. Eng. J.*, 2020, **397**, 125336.

282. Y. Q. Shi, C. Liu, L. Liu, L. B. Fu, B. Yu, Y. C. Lv, F. Q. Yang and P. A. Song, *Chem. Eng. J.*, 2019, **378**, 122267.

283. W. Q. Zhi, S. L. Xiang, R. J. Bian, R. Z. Lin, K. H. Wu, T. W. Wang and D. Y. Cai, *Compos. Sci. Technol.*, 2018, **168**, 404-411.

284. J. Q. Luo, S. Zhao, H. B. Zhang, Z. M. Deng, L. L. Li and Z. Z. Yu, *Compos. Sci. Technol.*, 2019, **182**, 107754.

285. Y. Liu, J. Zhang, X. Zhang, Y. Li and J. Wang, *ACS Appl. Mater. Interfaces*, 2016, **8**, 20352-20363.

286. G. Tiouitchi, M. Raji, O. Mounkachi, M. A. Ali, A. Mahmoud, F. Boschini, H. Essabir, R. Bouhfid and A. Qaiss, *Compos. Pt. B-Eng.*, 2019, **175**, 107165.

287. H. Ni, X. C. Liu and Q. F. Cheng, *J. Mater. Chem. A*, 2018, **6**, 7142-7147.

288. S. L. Qiu, B. Zou, H. B. Sheng, W. W. Guo, J. L. Wang, Y. Y. Zhao, W. Wang, R. K. K. Yuen, Y. C. Kan and Y. Hu, *ACS Appl. Mater. Interfaces*, 2019, **11**, 13652-13664.

289. S. L. Qiu, Y. F. Zhou, X. Zhou, T. Zhang, C. Y. Wang, R. K. K. Yuen, W. Z. Hu and Y. Hu, *Small*, 2019, **15**, 33-57.

290. B. Zou, S. Qiu, X. Ren, Y. Zhou, F. Zhou, Z. Xu, Z. Zhao, L. Song, Y. Hu and X. Gong, *J. Hazard. Mater.*, 2020, **383**, 121069.

291. W. Yang, J. Liang, S. Qiu, Y. Zhou, B. Zou, J. Wang, L. Song and Y. Hu, *Compos. Part A: Appl. Sci. Manuf.*, 2022, **163**, 107255.

292. W. Yang, S. Qiu, Y. Zhou, J. Wang, B. Zou and L. Song, *Chemosphere*, 2022, **303**, 135012.

293. S. Qiu, W. Yang, X. Wang and Y. Hu, *Chem. Eng. J.*, 2023, **453**, 139759.

294. J. Guo, L. Yang, L. Zhang and C. Li, *Polymer*, 2022, **255**, 125036.

295. W. Cai, T. M. Cai, L. X. He, F. K. Chu, X. W. Mu, L. F. Han, Y. Hu, B. B. Wang and W. Z. Hu, *J. Hazard. Mater.*, 2020, **387**, 121971.

296. W. Cai, Y. X. Hu, Y. Pan, X. Zhou, F. K. Chu, L. F. Han, X. W. Mu, Z. Y. Zhuang,

View Article Online
DOI: 10.1039/D4NR01356E

X. Wang and W. Y. Xing, *Journal of Colloid and Interface Science*, 2020, **561**, 32-45.

297. S. Qiu, X. Ren, X. Zhou, T. Zhang, L. Song and Y. Hu, *ACS Appl. Mater. Interfaces*, 2020, **12**, 36639-36651.

298. Y. Zhou, J. Huang, J. Wang, F. Chu, Z. Xu, W. Hu and Y. Hu, *Polymer Degradation and Stability*, 2020, **178**, 109194.

299. X. W. Mu, J. Zhan, X. M. Feng, B. H. Yuan, S. L. Qiu, L. Song and Y. Hu, *ACS Appl. Mater. Interfaces*, 2017, **9**, 23017-23026.

300. X. W. Mu, J. Zhan, X. M. Feng, W. Cai, L. Song and Y. Hu, *Compos. Pt. A-Appl. Sci. Manuf.*, 2018, **110**, 162-171.

301. X. W. Mu, J. Zhan, J. L. Wang, W. Cai, B. H. Yuan, L. Song and Y. Hu, *J. Colloid Interface Sci.*, 2019, **539**, 609-618.

302. P. García-Arroyo, M. P. Arrieta, D. Garcia-Garcia, R. Cuervo-Rodríguez, V. Fombuena, M. J. Mancheño and J. L. Segura, *Polymer*, 2020, **196**, 122466.

303. Z. F. Wang, Q. Yu, Y. B. Huang, H. D. An, Y. Zhao, Y. F. Feng, X. Li, X. L. Shi, J. J. Liang, F. S. Pan, P. Cheng, Y. Chen, S. Q. Ma and Z. J. Zhang, *Acs Central Science*, 2019, **5**, 1352-1359.

304. Y. W. Yang, J. Zan, W. J. Yang, F. W. Qi, C. X. He, S. H. Huang, S. P. Peng and C. J. Shuai, *Mater. Chem. Front.*, 2020, **4**, 973-984.

305. S. Ma, Y. Hou, Y. Xiao, F. Chu, T. Cai, W. Hu and Y. Hu, *Mater. Chem. Phys.*, 2020, **247**, 122875.

306. X. G. Wang, S. H. Wang, W. J. Wang, H. F. Li, X. D. Liu, X. Y. Gu, S. Bourbigot, Z. W. Wang, J. Sun and S. Zhang, *Compos. Pt. B-Eng.*, 2020, **183**, 107568.

307. M. Afshari and M. Dinari, *Composites Part A: Applied Science and Manufacturing*, 2021, **147**, 106453.

308. A. R. Ghohrodi, M. Ramezanzadeh and B. Ramezanzadeh, *Prog. Org. Coat.*, 2022, **164**, 106693.

309. Y. Li, J. Yin, Y. Feng, J. Li, H. Zhao, C. Zhu, D. Yue, Y. Liu, B. Su and X. Liu, *Chem. Eng. J.*, 2022, **429**, 132228.

310. Y. J. Ren, Y. F. Zhang, H. M. Fang, T. P. Ding, J. L. Li and S. L. Bai, *Compos. Pt. A-Appl. Sci. Manuf.*, 2018, **112**, 57-63.

311. X. L. Cui, P. Ding, N. Zhuang, L. Y. Shi, N. Song and S. F. Tang, *ACS Appl. Mater. Interfaces*, 2015, **7**, 19068-19075.

312. J. Zhang, W. W. Lei, D. Liu and X. G. Wang, *Compos. Sci. Technol.*, 2017, **151**, 252-257.

313. J. C. Li, X. Y. Zhao, W. J. Wu, Z. X. Zhang, Y. Xian, Y. T. Lin, Y. L. Lu and L. Q. Zhang, *Carbon*, 2020, **162**, 46-55.

314. H. Ribeiro, J. P. C. Trigueiro, C. F. Woellner, J. J. Pedrotti, D. R. Miquita, W. M. Silva, M. C. Lopes, G. J. M. Fechine, M. A. Luciano, G. G. Silva and P. M. Ajayan, *Polym. Test.*, 2020, **87**, 106510.

315. Q. S. Song, W. Zhu, Y. Deng, D. L. He and J. J. Feng, *Compos. Sci. Technol.*, 2018, **168**, 381-387.

316. X. Y. Li, P. Bandyopadhyay, T. Kshetri, N. H. Kim and J. H. Lee, *J. Mater. Chem. A*, 2018, **6**, 21501-21515.

317. S. J. Wan, Y. C. Li, J. S. Peng, H. Hu, Q. F. Cheng and L. Jiang, *ACS Nano*, 2015, **9**, 708-714.

318. Y. C. Guo, Y. Xue, X. H. Zuo, L. X. Zhang, Z. H. Yang, Y. C. Zhou, C. Marmorat, S. He and M. Rafailovich, *Polym. Degrad. Stab.*, 2017, **144**, 155-166.

319. Z. J. Liu, C. G. Yin, V. Cecen, J. C. Fan, P. H. Shi, Q. J. Xu and Y. L. Min, *Polymer*, 2019, **179**, 121613.

320. Y. L. Xiao, Z. Y. Jin, L. X. He, S. C. Ma, C. Y. Wang, X. W. Mu and L. Song,

View Article Online
DOI: 10.1039/D4NR01356E

Compos. Pt. B-Eng., 2020, **182**, 107616.

321. T. Krasian, W. Punyodom and P. Worajittiphon, *Chem. Eng. J.*, 2019, **369**, 563-575.

322. Y. Hou, Y. Hu, S. Qiu, L. Liu, W. Xing and W. Hu, *J. Hazard. Mater.*, 2019, **364**, 720-732.

323. T. Zhou, C. Wu, Y. Wang, A. P. Tomsia, M. Li, E. Saiz, S. Fang, R. H. Baughman, L. Jiang and Q. Cheng, *Nat. Commun.*, 2020, **11**, 2077.

324. T. Zhou, H. Ni, Y. Wang, C. Wu, H. Zhang, J. Zhang, A. P. Tomsia, L. Jiang and Q. Cheng, 2020, **117**, 8727-8735.

325. P. Yang, S. Ghosh, T. Xia, J. Wang, M. A. Bissett, I. A. Kinloch and S. Barg, *Compos. Sci. Technol.*, 2022, **218**, 109199.

326. S. Saha, W. Son, N. H. Kim and J. H. Lee, *J. Mater. Chem. A*, 2022, **10**, 4376-4391.

327. O. B. Seo, S. Saha, N. H. Kim and J. H. Lee, *J. Membr. Sci.*, 2021, **640**, 119839.

328. J. Yan, C. Wu, J. Hou, X. Zhang, Y. Liu, Y. Zhang, P. Li, H. Che, Z. Xing and Y. Wang, *Tribol. Int.*, 2023, **189**, 109000.

329. W. Yang, S. Qiu, Y. Zhou, B. Zou, J. Wang, P. Jia and L. Song, *ACS Appl. Nano Mater.*, 2022, **5**, 14841-14849.

330. A. Farshidfar, S. Bazgir, A. A. Katbab and A. Vaziri, *Polym. Test.*, 2023, **120**, 107951.

331. H. Ribeiro, J. P. C. Trigueiro, M. C. Lopes, J. J. Pedrotti, C. F. Woellner, W. M. Silva, G. G. Silva and P. M. Ajayan, *J. Appl. Polym. Sci.*, 2018, **135**, 46560.

332. B. Peng, M. Locascio, P. Zapol, S. Y. Li, S. L. Mielke, G. C. Schatz and H. D. Espinosa, *Nat. Nanotechnol.*, 2008, **3**, 626-631.

333. W. K. Li, A. Dichiara and J. B. Bai, *Compos. Sci. Technol.*, 2013, **74**, 221-227.

334. P.-G. Ren, Y.-Y. Di, Q. Zhang, L. Li, H. Pang and Z.-M. Li, *Macromol. Mater. Eng.*, 2012, **297**, 437-443.

335. T. K. Gupta, M. Choosri, K. M. Varadarajan and S. Kumar, *J. Mater. Sci.*, 2018, **53**, 7939-7952.

336. H. Xu, X. Li, P. Li, L. Ma, H. Li, L. Shi, M. Wang, H. Chen and G. Song, *Compos. Sci. Technol.*, 2020, **195**, 108191.

337. H. Ulus, T. Ustun, V. Eskizeybek, O. S. Sahin, A. Avci and M. Ekrem, *Appl. Surf. Sci.*, 2014, **318**, 37-42.

338. J. Y. Yuan, Z. Z. Zhang, M. M. Yang, L. F. Wu, P. L. Li, F. Guo, X. H. Men and W. M. Liu, *Compos. Pt. A-Appl. Sci. Manuf.*, 2019, **123**, 132-140.

339. Y. Li, X. Tian, W. Yang, Q. Li, L. Hou, Z. Zhu, Y. Tang, M. Wang, B. Zhang, T. Pan and Y. Li, *Chem. Eng. J.*, 2019, **358**, 718-724.

340. N. Domun, K. R. Paton, H. Hadavinia, T. Sainsbury, T. Zhang and H. Mohamud, *Materials*, 2017, **10**, 1179.

341. O. K. Park, P. S. Owuor, Y. M. Jaques, D. S. Galvao, N. H. Kim, J. H. Lee, C. S. Tiwary and P. M. Ajayan, *Compos. Sci. Technol.*, 2020, **188**, 107977.

342. N. D. Badgayan, S. K. Sahu, S. Samanta and P. S. R. Sreekanth, *J. Mech. Behav. Biomed. Mater.*, 2018, **80**, 180-188.

343. K. Zhou, J. Liu, Y. Shi, S. Jiang, D. Wang, Y. Hu and Z. Gui, *ACS Appl. Mater. Interfaces*, 2015, **7**, 6070-6081.

344. C. Ji, C. Z. Yan, Y. Wang, S. X. Xiong, F. R. Zhou, Y. Y. Li, R. Sun and C. P. Wong, *Compos. Pt. B-Eng.*, 2019, **163**, 363-370.

345. D. Wang, X. W. Mu, W. Cai, X. Zhou, L. Song, C. Ma and Y. Hu, *Compos. Pt. A-Appl. Sci. Manuf.*, 2019, **121**, 36-44.

346. Z. H. Zhou, W. Panatdasirisuk, T. S. Mathis, B. Anasori, C. H. Lu, X. X. Zhang, Z. W. Liao, Y. Gogotsi and S. Yang, *Nanoscale*, 2018, **10**, 6005-6013.

347. M. Aakyiir, J. A. Oh, S. Araby, Q. H. Zheng, M. Naeem, J. Ma, P. Adu, L. Q. Zhang

View Article Online
DOI: 10.1039/D4NR01356E

and Y. W. Mai, *Compos. Sci. Technol.*, 2021, **214**, 9.

348. P. Jia, J. Lu, R. He, G. Jiang, X. Jiang, B. Wang, L. Song and Y. Hu, *Chem. Eng. J.*, 2022, **450**, 138184.

349. C. Zhao, P. Zhang, J. Zhou, S. Qi, Y. Yamauchi, R. Shi, R. Fang, Y. Ishida, S. Wang, A. P. Tomsia, M. Liu and L. Jiang, *Nature*, 2020, **580**, 210-215.

350. S. A. Jiang, Q. F. Li, J. W. Wang, Z. L. He, Y. H. Zhao and M. Q. Kang, *Compos. Pt. A-Appl. Sci. Manuf.*, 2016, **87**, 1-9.

351. D. G. Papageorgiou, M. F. Liu, Z. L. Li, C. Valles, R. J. Young and I. A. Kinloch, *Compos. Sci. Technol.*, 2019, **175**, 60-68.

352. A. K. Pathak, M. Borah, A. Gupta, T. Yolcozeki and S. R. Dhakate, *Compos. Sci. Technol.*, 2016, **135**, 28-38.

353. X. Q. Zhang, X. Y. Fan, C. Yan, H. Z. Li, Y. D. Zhu, X. T. Li and L. P. Yu, *ACS Appl. Mater. Interfaces*, 2012, **4**, 1543-1552.

354. Z. Xu, G. Lin and G. Sui, *J. Appl. Polym. Sci.*, 2020, **137**, 49212.

355. Y. Wu, Y. He, C. Chen, H. Li, Y. Xia and T. Zhou, *Prog. Org. Coat.*, 2019, **129**, 178-186.

356. D. G. Papageorgiou, I. A. Kinloch and R. J. Young, *Compos. Sci. Technol.*, 2016, **137**, 44-51.

357. R. G. Wang, Z. Li, W. B. Liu, W. C. Jiao, L. F. Hao and F. Yang, *Compos. Sci. Technol.*, 2013, **87**, 29-35.

358. N. N. Hong, J. Zhan, X. Wang, A. A. Stec, T. R. Hull, H. Ge, W. Y. Xing, L. Song and Y. Hu, *Compos. Pt. A-Appl. Sci. Manuf.*, 2014, **64**, 203-210.

359. H. Qu, Y. Wang, Y. S. Ye, W. Zhou, S. P. Bai, X. P. Zhou, H. Y. Peng, X. L. Xie and Y. W. Mai, *J. Mater. Chem. A*, 2017, **5**, 22361-22371.

360. Y. M. Yao, X. L. Zeng, R. Sun, J. B. Xu and C. P. Wong, *ACS Appl. Mater. Interfaces*, 2016, **8**, 15645-15653.

361. C.-G. Yin, Z.-J. Liu, R. Mo, J.-C. Fan, P.-H. Shi, Q.-J. Xu and Y.-L. Min, *Polymer*, 2020, **195**, 122455.

362. S. Montes, P. M. Carrasco, V. Ruiz, G. Cabanero, H. J. Grande, J. Labidi and I. Odriozola, *Compos. Sci. Technol.*, 2015, **117**, 26-31.

363. N. El Miri, M. El Achaby, A. Fihri, M. Larzek, M. Zahouily, K. Abdelouahdi, A. Barakat and A. Solhy, *Carbohydr. Polym.*, 2016, **137**, 239-248.

364. J. L. Duan, S. S. Gong, Y. Gao, X. L. Xie, L. Jiang and Q. F. Cheng, *ACS Appl. Mater. Interfaces*, 2016, **8**, 10545-10550.

365. J. Zhang, W. W. Lei, J. Y. Chen, D. Liu, B. Tang, J. L. Li and X. A. Wang, *Polymer*, 2018, **148**, 101-108.

366. S. Chatterjee, F. Nafezarefi, N. H. Tai, L. Schlagenhauf, F. A. Nuesch and B. T. T. Chu, *Carbon*, 2012, **50**, 5380-5386.

367. Y. Q. Li, T. Y. Yang, T. Yu, L. X. Zheng and K. Liao, *J. Mater. Chem.*, 2011, **21**, 10844-10851.

368. S. Y. Yang, W. N. Lin, Y. L. Huang, H. W. Tien, J. Y. Wang, C. C. M. Ma, S. M. Li and Y. S. Wang, *Carbon*, 2011, **49**, 793-803.

369. A. Rostami and M. I. Moosavi, *J. Appl. Polym. Sci.*, 2020, **137**, 11.

370. K. H. Nam, J. Yu, N. H. You, H. Han and B. C. Ku, *Compos. Sci. Technol.*, 2017, **149**, 228-234.

371. J. Wang, X. Jin, H. Wu and S. Guo, *Carbon*, 2017, **123**, 502-513.

372. R. Scaffaro and A. Maio, *Compos. Pt. B-Eng.*, 2019, **168**, 550-559.

373. R. Mo, L. Zhu, X. Wu, W. Guo, Y. Min and J. Fan, *Polym. Compos.*, 2022, **43**, 2638-2650.

374. D. Lou, H. Chen, J. Liu, D. Wang, C. Wang, B. K. Jasthi, Z. Zhu, H. Younes and H.

View Article Online
DOI: 10.1039/D4NR01356E

Hong, *ACS Appl. Nano Mater.*, 2023, **6**, 12515-12525.

375. M. Dong, Y. Hu, X. Yu, M. Liu, E. Bilotti, H. Zhang and D. G. Papageorgiou, *ACS Appl. Polym. Mater.*, 2024, **6**, 207-217.

376. L. Liu, G. Ying, Y. Zhao, Y. Li, Y. Wu, D. Wen, M. Wu, M. Wang, Q. Zhou, X. Wang and C. Wang, *Polymers*, 2021, **13**, 1820.

377. L. Liu, G. Ying, C. Sun, H. Min, J. Zhang, Y. Zhao, D. Wen, Z. Ji, X. Liu, C. Zhang and C. Wang, *Polymers*, 2021, **13**, 1825.

378. B. Tang, Y. Yang, Y. Shi, H. Nie, H. Xia and X. Shen, *Polym. Compos.*, 2021, **42**, 2010-2018.

379. T. Jiang, T. Kuila, N. H. Kim, B. C. Ku and J. H. Lee, *Compos. Sci. Technol.*, 2013, **79**, 115-125.

380. L. Chen, S. G. Chai, K. Liu, N. Y. Ning, J. Gao, Q. F. Liu, F. Chen and Q. Fu, *ACS Appl. Mater. Interfaces*, 2012, **4**, 4398-4404.

381. Q. Y. Yang, Z. Xu, B. Fang, T. Q. Huang, S. Y. Cai, H. Chen, Y. J. Liu, K. Gopalsamy, W. W. Gao and C. Gao, *J. Mater. Chem. A*, 2017, **5**, 22113-22119.

382. M. Wang, L. Ma, L. Shi, P. Feng, X. Wang, Y. Zhu, G. Wu and G. Song, *Compos. Sci. Technol.*, 2019, **182**, 107751.

383. C. M. Damian, M. I. Necolau, I. Neblea, E. Vasile and H. Iovu, *Appl. Surf. Sci.*, 2020, **507**, 145046.

384. J. Zhang, C. Li, C. Yu, X. Wang, Q. Li, H. Lu, Q. Zhang, J. Zhao, E. Songfeng, M. Hu and Y. Yao, *Compos. Sci. Technol.*, 2019, **169**, 167-175.

385. Y. Xia, Y. He, C. Chen, Y. Wu and J. Chen, *Prog. Org. Coat.*, 2019, **132**, 316-327.

386. H. Peng, D. Wang, M. Li, L. Zhang, M. Liu and S. Fu, *Compos. B: Eng.*, 2019, **174**, 107037.

387. X. Zhang, J. Zheng, H. Fang, Y. Zhang, S. Bai and G. He, *Compos. Sci. Technol.*, 2018, **167**, 42-52.

388. J. Li, X. Zhao, Z. Zhang, Y. Xian, Y. Lin, X. Ji, Y. Lu and L. Zhang, *Compos. Sci. Technol.*, 2020, **186**, 107930.

389. G. Y. Duan, Y. T. Cao, J. Y. Quan, Z. M. Hu, Y. Wang, J. R. Yu and J. Zhu, *J. Mater. Sci.*, 2020, **55**, 8170-8184.

390. L. J. Fang, C. Wu, R. Qian, L. Y. Xie, K. Yang and P. K. Jiang, *RSC Adv.*, 2014, **4**, 21010-21017.

391. C. Chen, Y. Xue, Z. Li, Y. F. Wen, X. W. Li, F. Wu, X. J. Li, D. Shi, Z. G. Xue and X. L. Xie, *Chemical Engineering Journal*, 2019, **369**, 1150-1160.

392. X. Q. Fan, Y. Ding, Y. Liu, J. J. Liang and Y. S. Chen, *ACS Nano*, 2019, **13**, 8124-8134.

393. Y. Ul-Haq, I. Murtaza, S. Mazhar, R. Ullah, M. Iqbal, H. Zeeshan ul, A. A. Qarni and S. Amin, *Ceram. Int.*, 2020, **46**, 5828-5840.

394. Y. H. Zhao, Y. F. Zhang, Z. K. Wu and S. L. Bai, *Compos. Pt. B-Eng.*, 2016, **84**, 52-58.

395. Y. Jiang, J. Wang, J. Wu and Y. Zhang, *Polym. Bull.*, 2021, **78**, 1213-1230.

396. Z. H. Tang, C. F. Zhang, Q. Y. Wei, P. J. Weng and B. C. Guo, *Compos. Sci. Technol.*, 2016, **132**, 93-100.

397. Y. H. Zhang, K. Y. Rhee and S. J. Park, *Compos. Pt. B-Eng.*, 2017, **114**, 111-120.

398. Y. Zhang, J. R. Choi and S. J. Park, *Compos. Pt. A-Appl. Sci. Manuf.*, 2017, **101**, 227-236.

399. P. Feng, Y. Kong, L. Yu, Y. Li, C. D. Gao, S. P. Peng, H. Pan, Z. Y. Zhao and C. J. Shuai, *Appl. Mater. Today*, 2019, **17**, 216-226.

400. X. Wang, S. L. Ji, X. Q. Wang, H. Y. Bian, L. R. Lin, H. Q. Dai and H. N. Xiao, *J. Mater. Chem. C*, 2019, **7**, 14159-14169.

401. Q. R. Zhang, Z. W. Li, X. H. Li, L. G. Yu, Z. J. Zhang and Z. S. Wu, *Chemical Engineering Journal*, 2019, **356**, 680-692.

402. X. Zhou, S. L. Qiu, W. Y. Xing, C. S. R. Gangireddy, Z. Gui and Y. Hu, *ACS Appl. Mater. Interfaces*, 2017, **9**, 29147-29156.

403. S. L. Qiu, Y. X. Hu, Y. Q. Shi, Y. B. Hou, Y. C. Kan, F. K. Chu, H. Sheng, R. K. K. Yuen and W. Y. Xing, *Compos. Pt. A-Appl. Sci. Manuf.*, 2018, **114**, 407-417.

404. D. Guo, G. X. Xie and J. B. Luo, *J. Phys. D-Appl. Phys.*, 2014, **47**, 25.

405. D. Li, E. Peng, F. Lu, B. Wang, Y. Shen, P. Liu, L. Liu, Y. Huang and Z. Hu, *Chemical Engineering Journal*, 2023, **455**, 140887.

406. J. Lu, B. Wang, P. Jia, W. Cheng, C. Liao, Z. Xu, L. Cheng and Y. Hu, *Chem. Eng. J.*, 2022, **427**, 132046.